Universitat Autònoma de Barcelona

First-principles theory of flexoelectricity: Methods and applications

Andrea SCHIAFFINO

Universitat Autònoma de Barcelona

PH.D. THESIS

DOCTORAL PROGRAM IN PHYSICS

First-principles theory of flexoelectricity: Methods and applications

---

Candidate:
Andrea SCHIAFFINO

Supervisor:
Dr. Massimiliano STENGEL

Tutor:
Prof. Àlvar SÁNCHEZ MORENO

Department of Physics

Academic Year 2018/2019

Resumen

Esta tesis se centra en los desarrollos recientes de la teoría microscopía de la flexoelectricidad y sus aplicaciones prácticas con tal de estudiar la respuesta física en sistemas concretos. La flexoelectricidad es la propiedad electromecánica de todos los aislantes de desarrollar una respuesta polar a una perturbación uniforme del gradiente de deformación.

Una teoría formal de tal efecto se ha establecido recientemente en el marco de la teoría de perturbación del funcional densidad (DFPT). Aun así, para alcanzar una metodología valiosa para la automatización del cálculo de la respuesta flexoeléctrica para un cristal genérico, quedan algunos detalles conceptuales y prácticos. Estos están relacionados con las rotaciones locales de la muestra que pueden seguir una perturbación de gradiente de deformación. En esta tesis nos ocuparemos de tal cuestión; la solución se basa en la introducción de una nueva perturbación del cristal, la perturbación métrica, que se define como un fonón acústico descrito en el sistema de referencia que se mueve conjuntamente con los átomos. Después de presentar su implementación formal en el contexto de DFPT y en la aproximación de pseudopotencial separable, emplearemos esta nueva herramienta para calcular el tensor flexoeléctrico para materiales seleccionados.

A los logros anteriores les sigue una aplicación práctica de la teoría flexoeléctrica a la ingeniería del diseño de dispositivos "flexovoltaicos", es decir dispositivos fotovoltaicos cuyos principios fundamentales de trabajo se basan en el efecto flexoeléctrico. En la práctica, gracias a la estrecha conexión entre la teoría de la flexoelectricitad y y la teoría de los potenciales absolutos de deformación, mostramos cómo se puede calcular el perfil de bandas electrónicas en nanodispositivos doblados utilizando pocos y bien definidos parámetros. Dichos parámetros dependen de las condiciones de contorno electrostático impuesto.

Finalmente centraremos nuestra atención en la respuesta polar mostrada por las paredes del dominio (PdD) ferroeelástico en $SrTiO_3$, recientemente detectado. En general, las PdD se consideran una fuente prometedora de efectos físicos inusuales que pueden ser de interés práctico para aplicaciones de dispositivos electrónicos. Para mejorar la aplicabilidad de tales efectos físicos, es imprescindible entender su

origen. Inspirados en la teoría de la flexoelectricidad, en este trabajo desarrollamos una metodología original para estudiar el caso de las PdD ferroelásticos en $SrTiO_3$, que se basa en la construcción de un modelo energético efectivo, construido en base a calculos de primeros principios, y eso incluyendo los efectos de los acoplamientos entre diferentes distorsiones inhomogeneas del cristal. Se discuten los efectos de cada contribución a la polarización total en las PdD.

Summary

This thesis focus on the recent developments of the microscopic flexoelectric theory and its practical applications to study the physical response in concrete systems. Flexoelectricity is the electromechanical property of all insulators of developing a polar response to a uniform strain gradient perturbation.

A formal theory of such effect has been recently established in the framework of density functional perturbation theory (DFPT). Still, in order to reach a valuable methodology to facilitate the calculation of the bulk flexoelectric response for a generic crystal, some conceptual and practical subtelties remains. They are related with local rotations of the sample that can follow a strain gradient perturbation. In this thesis we will deal with such issue; The solution is based on the introduction of a novel crystal perturbation, the metric perturbation, which is defined as an acoustic phonon described in the reference frame that is co-moving with the atoms. After presenting its formal implementation in the context of the DFPT within the separable pseudopotential approximation, we will employ such new tool to perform extensive calculations of the flexoelectric tensor for selected materials.

The previous achievements are followed by a practical application of the flexoelectric theory to engineering the design of "flexovoltaic" devices, i.e. photovoltaic devices that base their fundamental working principles on the flexoelectric effect. In practice, thanks to the close connection between the flexoelectric theory and the theory of absolute deformation potentials, we show how the electron band profile of bended nanodevices can be calculated, in a mesoscopic semiclassical framework, using few and well defined parameters. Such parameters vary with respect to the type of electrostatic boundary conditions imposed.

Finally, we will focus our attention on the polar response shown by the ferroelastic domain walls (DWs) in $SrTiO_3$, recently detected. In general, DWs are considered a promising source of unusual physical effects that can be of practical interest for electronic device applications. For improving the applicability of such physical effects it is essential to understand their origin. Inspired by the theory of flexoelectricity we develop an original methodology to study the case of the ferrolastic DWs in $SrTiO_3$, which is based on the construction of an effective energy model, full

from first principles, and that includes the effects of gradient mediated couplings between different crystal distortions. The effects of each identified contribution to the total polarization at the DWs is discussed.

Contents

Resumen iii

Summary v

1 Introduction 1

2 First-principles background 7
2.1 Density functional theory . . . 8
2.1.1 Local density approximation . . . 11
2.1.2 External potential . . . 11
2.1.3 Plane waves . . . 12
2.2 Density functional pertrubation theory . . . 14
2.2.1 Phonon pertrubation . . . 16
2.2.2 Uniform strain perturbation . . . 18
2.2.3 Polarization response . . . 20
2.2.4 Microscopic current density . . . 22

3 Theory of flexoelectricity 25
3.1 General theory . . . 26
3.1.1 Definition of FxE tensor . . . 26
3.1.2 Long wave analysis . . . 28
3.1.3 Analyticity of response function around Γ . . . 32
3.1.4 Surface contributions . . . 33
3.2 Calculation of the electronic bulk FxE response . . . 36
3.2.1 Via charge density . . . 36
3.2.2 Via current density . . . 39
3.3 Revised analysis in curvilinear coordinates . . . 40

4 The metric wave approach 47
4.1 Metric perturbation in the context of DFPT . . . 49
4.2 Relation between acoustic phonon in curvilinear and Cartesian frame 52

4.3 Implementation Considerations . . . 56
4.4 Numerical tests . . . 58
4.4.1 Computational setup . . . 59
4.4.2 Charge density response: Phonon vs. metric . . . 60
4.4.3 Charge density response: Strain vs. metric . . . 62
4.4.4 Octupoles . . . 63
4.5 FxE tensors from metric perturbation . . . 64
4.5.1 Isolated spherical atoms . . . 65
4.5.2 Cubic materials . . . 67

5 Flexoelectricity for practical applications: Silicon flexovoltaic devices 71
5.1 Introduction . . . 72
5.2 The flexovoltaic idea . . . 73
5.3 The theory of absolute deformation potentials . . . 74
5.3.1 Macroscopic electrostatic term . . . 76
5.3.2 Band-structure term . . . 77
5.4 Results . . . 78
5.4.1 Bulk material constants . . . 78
5.4.2 Optimal Flexovoltaic silicon membrane . . . 81
Comparison with previous works . . . 85
5.5 Metallic electrodes . . . 86

6 Polar ferroelastic twin walls in $SrTiO_3$ 93
6.1 Introduction . . . 94
6.1.1 Geometry of the problem . . . 96
6.2 A multiscale harmonic approach . . . 97
6.2.1 The microscopic model . . . 100
6.2.2 Connections to continuum models . . . 103
6.2.3 Anhamronic couplings . . . 105
6.3 New coupling terms . . . 105
6.3.1 Rotopolar coupling . . . 106
6.3.2 Anti-ferroelectric mode of the Ti atoms . . . 107
6.4 Continuum model for STO . . . 109
6.4.1 Validating the macroscopic model . . . 111
6.5 Twin walls in STO . . . 112
6.5.1 Details on the solution of the continuum model . . . 112
6.5.2 Thickness and energy . . . 115
6.5.3 Domain wall polarity . . . 118

6.5.4 Conclusions 121

7 Conclusions **123**

A Ionic response to a strain gradient deformation **127**

B Detailed analysis of surfaces in curvilinear coordinates **131**
Cubic crystals: Full bulk flexoelectric tensor by surface response . . . 136

C Metric Hamiltonian **137**
Local potential 137
Separable potential 138

Bibliography **141**

List of Figures

1.1 Schematic effects of a uniform strain deformation (a) and of a uniform strain gradient deformation (b) on a centrosymmetric crystal. Figure from Ref [96]. 3
1.2 Schematic representation of the experimental setup for measuring the current induced by the flexo-photovoltaic effects. Figure from Ref. [92]. 6

3.1 The independent strain gradient deformations for a cubic crystal, for both the type-I and type-II strain gradient definition (from Ref. [77]). 28
3.2 (a) The pristine slab and the associated potential profile. (b) the same slab under a uniform longitudinal strain; the variation of the surface dipoles, p^U, are marked as red arrows; the variation of the surface dipole produce an dipper potential box; (c) the same slab under a longitudinal strain gradient deformation; the variation of the surface dipole is now in the same direction. The yellow potential profile shows the only contribution of the bulk flexovoltage response (the surface term is not taken into account), while the the blue is the total flexovoltage, bulk+surface. 33
3.3 The logical steps to understand the origin of an extra contribution to the bulk flexoelectric response that is generated by the local rotation of the sample. The local gradient rotations of the sample induce a solenoidal current density response (via the Larmor's theorem) whose effects is to induce a solenoidal polarization. The bulk contribution of such polarization is different from zero (red arrows), but is cancelled by an equal and opposite surface term (green arrows). 45

4.1 Illustration of the coordinate transformation to the co-moving frame. (a) Unperturbed crystal lattice; black circles represent the atomic sites, horizontal and vertical lines represent the coordinate system. (b) Transverse acoustic phonon in the laboratory frame. (c) The same phonon in the curvilinear frame; note that the atoms do not move in this coordinate system – the mechanical deformation is described via the metric. 52
4.2 Representation of the Fourier space in 2D. The small black cross are the G-vectors, the black dot circle identifies the cutoff sphere centered in Γ, the blue continue circle identifies nonzero Fourier coefficients of $|u_{\mathbf{k}}>$, while the dashed green circle identifies the Fourier coefficients of $|u_{\mathbf{k},\mathbf{q}}>$ 56
4.3 Plot of $d(n^{u^\beta}_{\mathbf{q}}(\mathbf{r}), n^{(\beta)}_{\mathbf{q}}(\mathbf{r}) + \Delta n^{\beta}_{\mathbf{q}}(\mathbf{r}))$ [cf., Eq. (4.34)] as function of the wave vector $\mathbf{q}$ (reduced coordinates), for different the cutoff. All the results refer to longitudinal perturbations. From the top to the the bottom: He, Ne and Kr. 61
4.4 Cell integrated difference, $d(-in^{1,\beta}_{\alpha}(\mathbf{r}), n^{strain}_{\alpha\beta}(\mathbf{r}))$, between the first order term of the long wave expansion applied to the metric response density and the uniform strain response, calculated as in Ref. [33], for an He atom in a box undergoing a longitudinal mechanical perturbation. The two curves refer to two different values of the finite difference increment used for getting $n^{1,\beta}_{\alpha}(\mathbf{r})$. 62
4.5 Convergence of the FxE coefficients of $SrTiO_3$ and Si with k-point mesh for the phonon and metric implementations. 68

5.1 In a centrosymmetric material, the photoexited carriers have no preferential direction where to migrate, and the recombination rate is high. On the contrary, in presence of a strain-gradient deformation, as induced by simple bending, inversion symmetry is broken, the electronic bands tilt and electron and holes are actively split towards the opposite boundaries generating a *flexo-photovoltage*. 73
5.2 Electronic bands of bulk Si in the diamond structure using our pseudopotential. The Fermi level is set to zero. The inset shows the Brillouin zone and its high symmetry points (figure from Ref. [72]). . . . 77
5.3 Fitting procedure to get the longitudinal octupoles, $Q^{(3)}_{[100]}$ and $Q^{(3)}_{[110]}$. 79

5.4 The two type of deformations considered here: (a) the plate bending; (b) the beam bending. The red line identify the main bending direction, which varies in the green plane and is identified by the angle α. 82
5.5 (a)-(c) show the ADP for a silicon membrane oriented along the [100] direction and deformed as a plate banding and a beam bending respectively. The ADP values are plotted as function of the α parameter that describes the in-plane rotation of the membrane (b)-(d) show the ADP for a silicon membrane oriented along the [11-1] direction, again for the two different types of deformations considered in the text. The $\alpha = 0$ geometry coincide with the pictures represented in Fig. 5.4. 83
5.6 (a)-(b) show the ADP for a silicon membrane oriented along the [110] direction and deformed as a plate banding and a beam bending respectively. The ADP values are plotted as function of the α parameter that describes the in-plane rotation of the membrane The $\alpha = 0$ geometry coincide with the y-direction that coincides with [1-11]. . . 84
5.7 Electronic potential energy profile across the dielectric membrane for the unsupported open circuit case (a,b,c), and for the short circuit case, in which it has been added two metallic electrodes (d,e,f). (a,d) show the unperturbed systems; (b-e) show the effects of a uniform strain ($\varepsilon = 1$); (c-f) show the effects of a uniform strain gradient ($\Delta\varepsilon = 1/t$ where t is the thickness of the membrane). Legend of colors for the electronic energy profile: red is the unperturbed case; green-dashed (only for the SC cases) is an intermediated step, where only the effects of $\Delta\tilde{\varepsilon}_F$ are considered; blue is the final results for the mechanically perturbed cases. Finally, the black lines in the SC cases are the Fermi level. 87
5.8 Bands end electron potential energy alignment at the Si-Ti interfaces. Values in eV. 89
5.9 Electron potential energy and band profiles for the silicon membrane with short-circuited Ti electrodes, oriented along the [100] direction in the plate bending regime. The applied strain gradient is: $\Delta\varepsilon_{eff} = 0.1/t$, where t is the membrane thickness. This corresponds to a curvature radius of $R = 10t$. 90
5.10 Electron potential energy and band profiles for the unsupported silicon membrane with surfaces passivated by H atoms. The applied strain gradient is: $\Delta\varepsilon_{eff} = 0.1/t$, where t is the membrane thickness. 91

6.1 (a): Un-relaxed tetragonal cell of the AFD phase; (b): Simplified sketch that compare the primitive cubic cell of the high temperature phase (yellow cube) with respect the tetragonal cell; (c) Cubic primitive cell of the High temperature phase; (d): Conventional tetragonal cell, whose volume coincide with the cell in (a) but here the phase structure is the cubic one; (e-f): Schematic illustration of the two different TBs considered in this work, respectively HH (e) and HT (f) configurations; dashed square indicates the primitive cell of the cubic reference phase and arrows indicate the local tilt vector. 98

6.2 Phonon frequencies as function of the wavevector q in reduced coordinates, where $a_{[110]} = a_0\sqrt{2}$ and a_0 is the cubic lattice parameter of STO. In panel (a) the phonon dispersions are plotted along the Γ-M direction, adn in panel (b) along the R'-X' (see inset). Solid curves are first-principles data, while dashed and dot-dashed are the results of the model (see text). 113

6.3 Evolution of the strain across the ferroelastic twin walls. (a) and (b): illustrations of the two types of ferroelastic twin walls considered in this work (respectively HH and HT). Note that these are just schematic illustrations of how the order parameter evolves from one domain to the next - as discussed in the main text, the actual length scale of the transition is much larger than suggested by the cartoons. (c): Evolution of the individual strain components across the two DWs. Note that ε_{rr} and $\varepsilon_x x$ are uniform and fixed to their bulk value, in order to reproduce the correct mechanical boundary conditions for the domain wall structure. 114

6.4 (a),(b) Schematic illustration (not to scale) of the two different types of TBs considered in this work, respectively HH (a) and HT (b). Sr (large green balls), O (small red balls), and the oxygen octahedra are shown; the dashed square indicates the primitive cell of the cubic reference phase; the arrows indicate the local tilt vector. (c) Evolution of ϕ_s and ϕ_r across the two TBs. A local decomposition of the tilt vector (black arrows) into $\hat{s}$ (green) and $\hat{r}$ (red) is also shown. The shaded area indicates the nominal wall thickness 2ξ. (d) Amplitude of the u^{Ti} mode in arbitrary units. The inset illustrates the AFE character of the Ti displacements, resembling spins in a G-type antiferromagnet. The length scale is in units of ξ. 116

6.5 (a) Domain wall thickness 2ξ as a function of temperature. (b) Formation energy per surface unit as a function of temperature. 117

6.6 (a) Polarization profile across the two DWs; the dashed line refers to the result B, i.e., without including u^{Ti} in the simulation. (b): Total polarization integrated across the DW as a function of the addition of different couplings in the Hamiltonian. The empty and filled symbols refer to the results obtained while excluding or including the biquadratic and electrostrictive terms. The polarization vector is always oriented towards the apex of the twin boundary. 120
6.7 An AFD cycloid. 121

B.1 Polarization response in a slab under: (a) uniform transverse strain deformation; (b) uniform transverse strain gradient deformation; (c) uniform shear strain; (d) uniform shear strain gradient deformation. Figure from Ref. [74]. 132

List of Tables

4.1 $Q_L/6$ for He and Ne atoms, in e Bohr^2 (Short-circuit electrostatic boundary conditions). 63
4.2 $Q_L/6$ along the [100] direction for Si and along the [110] direction for $SrTiO_3$. Values are in unit of e Bohr^2 (SC electrostatic boundary conditions). The two different columns for Si refer to two different **k**-mesh used: 12×12×12 and 16×16×16, respectively. 63
4.3 Clamped-ion flexoelectric coefficients calculated using the metric and phonon implementations, as well as the quadrupole moments of the ground-state charge density. All quantities are in units of pC/m. . . 66
4.4 Flexoelectric constants for $SrTiO_3$ and Si calculated using the phonon and metric implementations (units are nC/m); their orbital magnetic susceptibilities, χ^{mag}, are respectively -8.3×10^{-3} and 10.2×10^{-3}nC/m. 67

5.1 Here are listed the value of the two longitudinal flexovoltage, $\varphi^{tot}_{[100]}$ and $\varphi^{tot}_{[110]}$, which are the only two independent values that can be calculated using the bulk charge density response respectively along the [100] and [110] direction, together with reference values. HV and RCB stand respectively for Ref. [36] and Ref. [62], and remind the difference in the definition of $\mu_{[110]}$ between this work and HV's work. For $\mu_{[110]}$ we have disentangled the two contributions, the electronic and mixed term, tanks to our calculation of $Q^{(2)}$ and Γ. 80
5.2 Final values of the three independent bulk flexovoltages for silicon. The electronic contributions are compared with other two independent results: (a) are from Ref. [65]; (b) are from the the previous Chapter 4, Tab. 4.4; (c) are the values calculated here. 80
5.3 The parameters that describe the BS deformation potential of silicon to a generic mechanical deformation. Values in eV. 81

5.4 DP, comparison with values reported in Ref. [87]. The relations connecting the present notation to Ref. [87] are: $b = (\frac{l-m}{3})$; $d = \frac{n}{\sqrt{3}}$; $\Xi_u = \beta$; $\Xi_d = \alpha$; $a = \frac{l+2m}{3}$. 81

6.1 Calculated model parameters compared with the available literature data (US=Uwe and Sakudo [84], SV=Sai and Vanderbilt [66]). The elastic and rotostriction coefficients are repoted in the more common Voigt notation for the Cartesian axis The calculated value of κ is reported in italics, as we have replaced it with a phenomenological function of temperature, Eq. 6.36. Note that the χ_0 value calculated within the zero-temperature first-principles calculations, matches with the experimental value of the dielectric constant at $T \sim 80$ K [88]; $4\pi\chi_0 \sim 1500$. 110

List of Abbreviations

FxE	**F**lexo**e**lectric
EBC	**E**lectrostatic **B**oundary **C**onditions
OC	**O**pen **C**ircuit
SC	**S**hort **C**ircuit
OP	**O**rder **P**arameter
DFT	**D**ensity **F**unctional **T**heory
DFPT	**D**ensity **F**unctional **P**ertrubation **T**heory
FE	**F**erroel**e**lectric
AFE	**A**nti **F**erroel**e**lectric
AFD	**A**nti-**F**erro**d**istortive
DW	**D**omain **W**all
TW	**T**win **W**all
STO	**S**r**T**i$\mathbf{O}_3$
r.h.s.	**r**ight **h**and **s**ide
l.h.s.	**l**eft **h**and **s**ide

Chapter 1

Introduction

Conversion of mechanical energy into electrical one and vice versa is nowadays the fundamental building block in many of the technological devices employed in a wide variety of fields such as high performance electronics, medical diagnosis instruments and automotive industry. The electromechanical properties of crystals describe precisely the possibility for an external mechanical deformation to induce a crystal electrical response, or the reverse effect. Among them, the most famous example is piezoelectricity, which is defined as the polarization generated by the application of a uniform strain. Such effect was first discovered in 1880 by Pierre and Jacques Curie in quartz, topaz and Rochelle salt crystals. Subsequent studies and improvements of piezoelectric materials have lead them to be extensively used in sensor, actuator, high voltage generators and transducers.

Flexoelectricity is another electromechanical property, and it describes the polarization, P_α, that is linearly induced by a strain *gradient* deformation, $\partial \varepsilon_{\gamma\delta}/\partial x_\beta$,

$$P_\alpha = \mu_{\alpha\beta\gamma\delta} \frac{\partial \varepsilon_{\gamma\delta}}{\partial x_\beta}, \tag{1.1}$$

where $\mu_{\alpha\beta\gamma\delta}$ is the flexoelectric (FxE) tensor. One of the main differencses between the piezoelectric and flexoelectric effect is that the latter is a universal property of all crystals, while the former, being expressed via a third-rank tensor, is only allowed in crystals that break inversion symmetry (see Fig. 1.1).

The flexoelectric effect was theoretically predicted in the 60s [44, 53], and the first clear experimental evidence was reported by Bursian and Zaikovskii back in 1968 [10]. Two key features of the flexoelectric response were immediately clear: it is proportional to the dielectric constant [9] and it is inversely proportional to the sample size [10] (indeed at smaller scales, a strain variation can induce a huge strain gradient). Due to the latter, at the beginning the new effect did not surge to a popular topic among the condensed matter community, since the available technology only allowed to work at scales where flexoelectricity has negligible effects. On the contrary, thanks to the recent achievements on the fabrication of micro and nano devices, flexoelectricity has experienced a boost in popularity.

From the experimental side, the "revival" of the flexoelectric response was initiated by Ma and Cross at the beginning of 2000s [47–49]. Their attention was mainly addressed to ceramic compounds, since they are known to have a much higher dielectric constant respect to conventional semiconductors. More recently, a turning point was the systematic study performed by Zubko et al. [95] to measure the flexoelectric tensor components of the cubic phase of $SrTiO_3$ the single crystal. Then, it was experimentally shown that the electric response induced by strain gradient

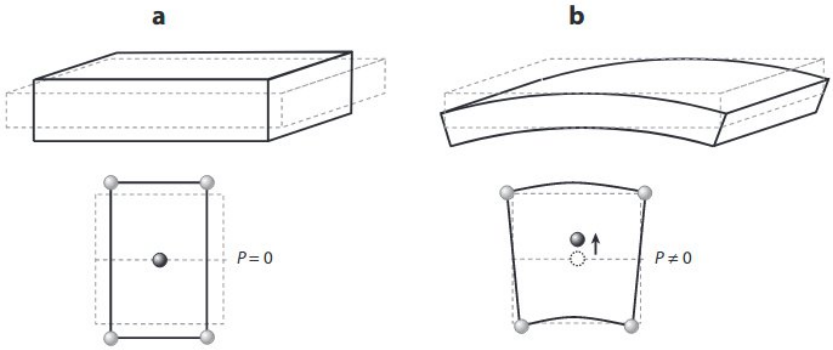

FIGURE 1.1: Schematic effects of a uniform strain deformation (a) and of a uniform strain gradient deformation (b) on a centrosymmetric crystal. Figure from Ref [96].

deformations is capable of rotating [14] or even switching [46] the spontaneous polarization of ferroelectric materials. Different flexoelectric devices have been already proposed and tested as sensors and transductors [17, 94], actuators [6, 7], and as an effective charge separator for solar cell applications [15].

These experiments identified the following points: (i) by means of the current technology, it is impossible to measure all the independent components of the bulk flexoelectric tensor; (ii) the flexoelectric tensor components greatly differ, even by more than one order of magnitude, between the results reported by independent groups; (iii) it is not clear if and, in case, how the surfaces influence the total response. These open questions were a strong motivation for a robust theoretical support, in order to develop a predictive theory of flexoelectricity, starting from its microscopic origins. Moving from the reference work by Born and Huang [8], Tagantsev developed, back in the 1986 [80], a first microscopic model based on a point-charge crystal. Despite the simplicity of such a model, which could account for the polarizability of the atoms, this work is the base of the more recent developments on the FxE effects.

Starting from the late '70s, density functional theory (DFT) simulations have surged to a popular and reliable computational tool in order to investigate the quantum-mechanical origin of effects belonging to physics, materials science, chemistry, mineralogy and biology. What makes them so appealing is the fact that they are *ab initio* calculations, i.e. their only external input is the chemical information

on the atomic specied, and they show a perfect balance between accuracy and computational efficiency. Unfortunately, a direct DFT simulations of a strain gradient deformation is difficult. Indeed in practical implementations of DFT, periodic boundary conditions are commonly enforced.

Apart from a couple of remarkable early attempts [35, 50], the development of a formal theory of flexoelectricity only started in 2010 with Resta [64]. Inspired by the seminal paper on piezoelectricity by Martin [51], Resta based its analysis on the microscopic charge density response to atomic displacements. This theory was subsequently employed by Hong and Vanderbilt [37] for calculating, within DFT, the electronic flexoelectric response for selected materials.

Soon it became clear, however, that the charge density response doses not contain enough information, at the bulk level, to extract all the independent components of the FxE tensor, even for the simplest cubic crystals [36, 77]. The issue is that the first-order charge density, being defined as a divergence, only retains the longitudinal components of the microscopic currents that adiabatically flow in the course of a mechanical deformation. This implies that, in order to capture the transverse components of the FxE tensor, one has to look at the current-density response itself; the latter, however, is not part of the standard capabilities of first-principles linear-response theory. Thus, at the time this doctoral project started, the problem of calculating the bulk flexoelectric tensor was not solved yet. The electronic contribution – which had proved to be the trickiest one to define and compute – still resisted the theoretical attempts that had been made thus far.

During this thesis, the first-principles theory of flexoelectricity has seen a number of impressive methodological advances, to which the present work has significantly contributed. To contestualize such developments, which will be detailed in Chapter 4, it is useful to recall one of the biggest obstacles in the treatment of mechanical deformations within a quantum-mechanical linear-response framework. At difference with conceptually simpler perturbations (e.g., phonons) a strain field changes the periodicity of the lattice, or even breaks it altogether if the strain is inhomogeneous. As such, it is hard to describe it in terms of a well-defined parametric dependence of the electronic Hamiltonian. The uniform strain problem has been elegantly solved by Hamann *et al.* [33] about fifteen years ago. The trick consists in expressing the total energy in reduced crystal coordinates. Then, the cell remains fixed to a unit cube, which alleviates the aforementioned difficulties – all the information about the deformation is encoded in the metric of space, which can now be treated as a formally sound perturbation parameter. As we shall see in Chapter 4, calculation of flexoelectricity is greatly facilitated as well by using similar ideas, that we have implemented by generalizing the theory of Ref. [33] to

the case of spatially modulated "metric waves". This not only provides a computationally efficient framework to calculate the full flexoelectric tensor, including the problematic transverse components, but also yields a physically appealing description of some peculiar contributions, coming from the gradients of the local rotation, that are related to orbital paramagnetism.

These developments, in principle, open the way to a systematic screening for materials with optimal flexoelectric properties, to be used as active elements in advanced pseudo-piezoelectric units. In this Thesis, however, we have taken a slightly different route, and initiated instead an exploration of other physical phenomena and systems (i.e., not necessarily electromechanical) where strain gradients are expected to play a significant role. One of the many "unconventional" (but potentially very important) applications of flexoelectricity has recently been demonstrated in the area of photovoltaics. Why flexoelectricity would enhance the photocurrent is intuitively clear: a strain gradient generally breaks inversion symmetry, which is the most important prerequisite for having a net drift of the photoexcited carriers within the sample. Ref. [92] possibly describes the most impressive realization of this idea: by applying pressure with an AFM tip (Fig. 1.2) the authors could induce a remarkable photoelectric response even in cubic single crystals. For our theoretical study we used a simpler material, bulk Si, as a testcase; strained semiconductor nanostructures are themselves been regarded as excellent candidates for photovoltaic applications [91]. As we shall see in Chapter 5, the theory of flexoelectricity can be an invaluable tool for the rational design of such systems: via a slight generalization, one can obtain a complete description of the electronic energy levels (in a mesoscopic semiclassical framework) of a sample subjected to an arbitrary deformation field, in terms of a small number of material-specific constants. Note that this is, a priori far from obvious, as one needs to cope with many subtleties regarding shape, surfaces and electrical boundary conditions, among others.

Domain walls (DWs), the regions separating different phase of the same material, are considered a promising source of peculiar physical effects that are not present in the bulk domains. Thanks to the modern advances in experimental techniques, the new field of domain wall nanoelectronics has flourished [13], whose core business is to exploit the DWs in ferroic materials as the active elements for applications. Based on the typical properties displayed by different DWs, they were proposed to be employed, for example, in electro-optic, photovoltaic and memory devices. Clearly, understanding the physical origin of the particular DWs properties is essential to boost the field of nanoelectronics. In Chapter 6 we will focus on the ferroelastic DWs in the antiferrodistortive phase of $SrTiO_3$ that show a peculiar polar behaviour, absent in the bulk domains. Since ferroelastic DWs are defined has

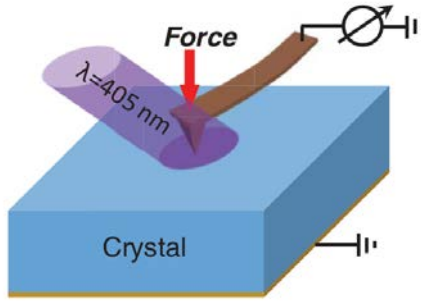

FIGURE 1.2: Schematic representation of the experimental setup for measuring the current induced by the flexo-photovoltaic effects. Figure from Ref. [92].

the walls separating two regions with opposite uniform strain, they are expected to sustain a remarkable strain gradient which ultimately can induce a notable flexoelectric effect. By employing the microscopic FxE theory, we will carry out a quantitative study of this effect in the case of $SrTiO_3$. In practice, we will build an effective energy model, based on full first-principles calculations, that include different gradient mediated couplings between the most relevant lattice distortions. We will find that the flexoelectric contribution is not the only important term to quantify the DW polarity, but other terms emerge. These new terms allows a close connection with the theory of cycloidal multiferroics, where the polarization is induced by gradients of the magnetic order parameter.

Before the three Chapters containing the original results of the present work, we have reported an extensive introduction on DFT and the recent developments on the flexoelectric theory. In Chapter 2 DFT together with its main applications to fields closely related to flexoelectricity are briefly sketched. In Chapter 3, we will give a summary of the main achievements of the flexoelectric theory that are fundamental to understand the following original results.

Chapter 2

First-principles background

In this Chapter we will briefly summarize the main outlines of density functional theory (DFT) and density functional perturbation theory (DFPT), which are the main methodologies employed all across this work. Many reviews [5, 57] and books [52] on these topics exist in the literature, therefore the choice here is to focus mainly on the aspects of the formalism that are most relevant to the results presented in this thesis. In particular, we will: (i) sketch the general ideas that lie behind DFT and DFPT, (ii) present the most significant equations for a practical implementation. Point (ii) is essential to fully understand the main difficulties and solutions faced during the formulation of a consistent theory of flexoelectricity from first principles (Chapter 3).

With these aims in mind, in the first section we will discuss the density-functional theory from a general point of view. In particular, we will review the Kohn and Sham formulation, and its explicit expressions in the case of plane wave basis set. Then, in the second section, we will present the foundations of DFPT, together with its specific application to the case of atomic displacements, uniform strain and uniform polarization response to mechanical deformations.

The final Section of this Chapter is devoted to outline the recent extension of the polar response to a monochromatic lattice displacement. Even though this is not a standard topic in common DFPT codes, it is of fundamental importance for the following derivations and to appreciate the original results of Chapter 4, where a new mechanical perturbation is presented and implemented.

2.1 Density functional theory

The non-relativistic Hamiltonian that describes the coupled motion of electrons and nuclei in a crystal can be written as

$$\hat{H} = \hat{T}_n + \hat{T}_e + \hat{V}_{ee} + \hat{V}_{nn} + \hat{V}_{ne} \tag{2.1}$$

where $\hat{T}_n$ and $\hat{T}_e$ are the kinetic contribution of the nuclei and the electrons respectively, while $\hat{V}_{ee}$, $\hat{V}_{nn}$ and $\hat{V}_{ne}$ describe the electron-electron, nucleus-nucleus and electron-nucleus interactions respectively. In order to solve the corresponding many body Schrödinger problem it is necessary to perform various number of approximations. The first one is the Born-Oppenheimer approximation: due to the mass difference between electrons and nuclei (10^{-15}), their dynamics can be regarded as decoupled. This approximation simplifies the previous Hamiltonian, by removing the nuclear kinetic energy. Therefore one is left with the problem of finding the electronic ground state in a fixed ionic configuration, and the Hamiltonian

reduces to

$$\hat{H}_e = \hat{T}_e + \hat{V}_{ee} + \hat{V}_{ext} + E_{nn} \tag{2.2}$$

where $V_{ext} = V_{ne}$. Note that in the electronic problem, Eq. 2.2, the effects of the nucleus-nucleus interactions are just an additive constant, and for simplicity it can be removed in the following derivation; nevertheless its presence in the final formulation is of fundamental importance in order to correctly treat the overall Coulomb interactions in extended systems [52].

Still, the Schrödinger equation associated to the Hamiltonian 2.2 involves a many-body wave function, Ψ, which is a function of $3N$ spatial coordinates (N is the number of particles); for $N > 10$ a direct solution becomes quickly out of reach even for modern supercomputers. In order to make this problem tractable, Hohenberg and Kohn established two theorems [34]: first, given the ground state density, the external potential, V_{ext}, acting on a system of interacting electrons is unique, apart from a trivial additive constant; second, given an external potential, the ground-state energy of any many-body system can be obtained as the variational minimum of a functional, $E[n]$, that only depends on the electronic density,

$$E_{GS} = \min_n E[n], \tag{2.3}$$

with the requirement that the density integrates to the total number of particles, $\int n(\mathbf{r}) d^3r = N$. The energy functional can be written as the sum of the external potential energy plus a universal term, $F[n]$, as

$$E[n] = F[n] + \int V_{ext}(\mathbf{r}) n(\mathbf{r})\, d^3r \tag{2.4}$$

Despite the generality of the two theorems, they do not provide any explicit recipe to construct the universal functional $F[n]$.

The next step forward in order to make the previous results computationally useful, is based on the ansatz by Kohn and Sham [45]. They assumed that the many body ground state density, n^0, is equal to the electronic density of some auxiliary independent-particle system, n^{KS}. In the new independent-particle framework the charge density is

$$n(\mathbf{r}) = \sum_i f_i |\psi_i(\mathbf{r})|^2, \tag{2.5}$$

where f_i is the occupation factor of the i-th state, and the functional $F[n]$ can be rewritten as

$$F^{KS}[n] = \tilde{T}[n] + E_H[n] + E_{xc}[n]. \tag{2.6}$$

The tilde on the first term indicates that only the independent-particle kinetic energy is included, which is commonly expressed as functional of the wavefunctions, $\tilde{T} = \sum_i f_i \langle \psi_i | \nabla_i^2 | \psi_i \rangle$; the electron-electron Hartree energy has been isolated in the term $E_H[n]$, and all the remainder of the many-body effects have been grouped into the exchange-correlation energy, $E_{xc}[n]$. In Eq. 2.6 the only unknown functional is the universal term $E_{xc}[n]$, whose knowledge would in principle allow one to access the exact solution of the many-body problem by solving the auxiliary independent-particle system. Despite the fact that an explicit formula for the exchange-correlation term is not available, many different approximation were proposed; clearly the higher the quality of the approximation, the closer the solution of the auxiliary system is to the real many-body solution. We will discuss in the following section 2.1.1 the approximation used for $E_{xc}[n]$ in this thesis. Here instead we sketch how the independent-particle problem can be solved.

The solution of the Kohn and Sham ground-state problem can be obtained by minimizing the functional 2.6 with respect the independent particle wavefunctions, ψ_i, together with the requirement that these wavefunction must be an orthonormal set. This operation is equivalent to solving the following one-particle Schrödinger equation

$$\left(-\frac{1}{2}\nabla^2 + \hat{V}_H + \hat{V}_{ext} + \hat{V}_{xc} \right) |\psi_i\rangle = \epsilon_i |\psi_i\rangle \tag{2.7}$$

where $\hat{V}_{ext}$ is the electron-nucleus interaction (in practical implementations this is replaced by a pseudopotential, see Sec.2.1.2), and

$$\begin{aligned} \hat{V}_H(\mathbf{r}) &= \int d^3r' \frac{n(\mathbf{r}')}{|\mathbf{r} - \mathbf{r}'|} \\ \hat{V}_{xc}(\mathbf{r}) &= \frac{\delta E_{xc}[n]}{\delta n(\mathbf{r})}. \end{aligned} \tag{2.8}$$

Note that the Hartree and the exchange-correlation potential appearing in Eqs. 2.7 depend on the charge density, which is ultimately function of the electronic wavefunctions, ψ_i, via Eq. 2.5. Indeed the KS equations must be solved self-consistently. With the aim of highlighting the self-consistent nature of the previous problem, it is convenient to rewrite the Hamiltonian, $\mathcal{H}$, appearing on the left hand side of the Schrödinger equation 2.7 as

$$\mathcal{H} = H + V_{scf}, \tag{2.9}$$

where $H = -\nabla^2/2 + V_{ext}$ includes the non self-consistent contributions, while $V_{scf} = V_H + V_{xc}$ includes the self-consistent terms.

Finally, the energy of the original problem can be rewritten, using the auxiliary systems and its ground-sate wavefunctions, as [52]

$$E_e = \sum_i f_i \langle \psi_i | H | \psi_i \rangle + E_H[n] + E_{xc}[n] + E_{nn} \tag{2.10}$$

where we have reinserted the nucleus-nucleus energy.

2.1.1 Local density approximation

The exact analytical expression for the exchange-correlation energy is not known. In this thesis we will employ the local density approximation (LDA), in which the effects of the exchange and correlation are explicitly treated as local. Despite such choice could appear to be too crude, it has proved to give remarkably good results even for strongly inhomogeneous cases. In such approximation, the exchange-correlation energy is written as

$$E_{xc}[n] = \int d^3r \, \varepsilon_{xc}(n) n(\mathbf{r}), \tag{2.11}$$

where $\varepsilon_{xc}(n)$ is the exchange-correlation energy per electron of a uniform electron gas that has the same density as the electron gas at point $\mathbf{r}$. Different parametrization for $\varepsilon_{xc}(n)$ are available, whose coefficients can be extracted via Monte Carlo methods. In this work we employ the Perdew-Wang 92 parametrization [58].

Finally, in the LDA approximation the exchange-correlation potential is

$$V_{xc} = \frac{\delta E_{xc}[n]}{\delta n} = \frac{d\varepsilon_{xc}(n)}{dn} n + \varepsilon_{xc}(n). \tag{2.12}$$

2.1.2 External potential

In order to reduce the computational cost it is useful to observe that the core electrons are almost inert to the environment surrounding each atom. This means that only the valence electrons participate in the chemical bonding and need to be treated explicitly, while the combined effect of nucleus and core electrons is replaced with effective ionic potentials called *pseudopotentials*. They are constructed with the constraint of reproducing (to some approximation) the scattering properties of the all-electron atom as seen by the valence wavefunctions. The scattering properties are different for each angular momentum component (defined by the azimuthal and magnetic quantum number, $\{l, m\}$) of the valence wavefunction. Then

the pseudopotential, v_κ^{psp}, of a given atomic species, κ, becomes a non-local function of $\mathbf{r}$ and $\mathbf{r}'$. For convenience, a pseudopotential is constructed by identifying two contributions, a long-range local term, $v_\kappa^{loc}(\mathbf{r})$, and a separable non-local term, $V_\kappa^{sep}(\mathbf{r},\mathbf{r}')$, [52, 57]:

$$v_\kappa^{psp}(\mathbf{r},\mathbf{r}') = v_\kappa^{loc}(\mathbf{r})\delta(\mathbf{r}-\mathbf{r}') + v_\kappa^{sep}(\mathbf{r},\mathbf{r}'). \tag{2.13}$$

The local term is spherically symmetric while the separable term written in the Kleinman-Bylander (KB) form is [42]

$$v_\kappa^{sep}(\mathbf{r},\mathbf{r}') = \sum_\mu e_{\mu\kappa}\zeta_{\mu\kappa}(\mathbf{r}-\mathbf{R}_{l\kappa})\zeta^*_{\mu\kappa}(\mathbf{r}'-\mathbf{R}_{l\kappa}), \tag{2.14}$$

where μ runs on the angular momentum components, $\{l,m\}$, $\zeta_{\mu\kappa}(\mathbf{r})$ are the KB projectors, and $e_{\mu\kappa}$ are the corresponding coefficients.

In the case of a crystal lattice, the external potential is written in terms of the single atomic pseudopotentials as

$$V^{ext}(\mathbf{r},\mathbf{r}') = \sum_{i\kappa} v_\kappa^{psp}(\mathbf{r}-\mathbf{R}_{a\kappa},\mathbf{r}'-\mathbf{R}_{a\kappa}) \tag{2.15}$$

where a labels the unit cell, κ runs on the sublattices and $\mathbf{R}_{a\kappa}$ identifies the position of the ion κ in the unit cell a.

2.1.3 Plane waves

In order to solve the KS equations in bulk crystals, it is common to take advantage of the periodicity of the system; this allows to perform the calculations in a primitive cell within periodic boundary conditions (PBC). In particular, thanks to the discrete translational symmetries enforced by the PBC, it is possible to use Bloch wavefunctions,

$$\psi_{n,\mathbf{k}}(\mathbf{r}) = \frac{1}{\sqrt{\Omega}} e^{i\mathbf{r}\cdot\mathbf{k}} u_{n,\mathbf{k}}(\mathbf{r}) \tag{2.16}$$

where Ω is the unit cell volume, n identifies the bands, $\mathbf{k}$ is a vector in reciprocal space and it is restricted to the first Brillouin zone, and $u_{n,\mathbf{k}}(\mathbf{r})$ is a periodic function in real space. The electronic density is then defined as

$$n(\mathbf{r}) = \frac{\Omega}{(2\pi)^3}\int_{BZ} d^3k \sum_n f_{n,\mathbf{k}}|u_{n,\mathbf{k}}(\mathbf{r})|^2, \tag{2.17}$$

where $f_{n,\mathbf{k}}$ is the occupation factor. Inserting the Bloch functions into the KS problem results in a new Schrödinger-like problem for the cell-periodic part, $u_{n,\mathbf{k}}(\mathbf{r})$, where the original Hamiltonian, Eq. 2.9, is replaced by its cell-periodic counterpart,

$$\hat{\mathcal{H}}_{\mathbf{k}} = e^{-i\mathbf{k}\cdot\mathbf{r}}\hat{\mathcal{H}}e^{i\mathbf{k}\cdot\mathbf{r}'}. \tag{2.18}$$

With the aim of fixing the notation that will be used in the rest of this work, we report the explicit expression for the cell-periodic part of the different terms in the Hamiltonian 2.18. Using the plane-wave basis set, the Bloch functions read as

$$u_{n,\mathbf{k}}(\mathbf{r}) = \sum_{\mathbf{G}} C_{n,\mathbf{k}+\mathbf{G}} e^{i\mathbf{r}\cdot\mathbf{G}} \tag{2.19}$$

and $C_{n,\mathbf{k}+\mathbf{G}}$ are the Fourier expansion coefficients.

The kinetic term is diagonal in the reciprocal space,

$$T_{\mathbf{k}}(\mathbf{G},\mathbf{G}') = \frac{1}{2}(\mathbf{k}+\mathbf{G})^2\delta_{\mathbf{G},\mathbf{G}'}. \tag{2.20}$$

The pseudopotential terms are respectively

$$\begin{aligned} V^{loc}_{\mathbf{k}}(\mathbf{G}) &= \begin{cases} \frac{1}{\Omega_{cell}}\sum_{\kappa} e^{-i\mathbf{G}\cdot\boldsymbol{\tau}_\kappa} v^{loc}_{\kappa}(\mathbf{G}) \text{ when } \mathbf{G}\neq 0 \\ 0 \text{ when } \mathbf{G}=0 \end{cases} \\ V^{sep}_{\mathbf{k}}(\mathbf{G},\mathbf{G}') &= \frac{1}{\Omega_{cell}}\sum_{\mu\kappa} e_{\mu\kappa}\left(e^{-i(\mathbf{k}+\mathbf{G})\cdot\boldsymbol{\tau}_\kappa}\zeta_{\mu\kappa}(\mathbf{k}+\mathbf{G})\right)\left(e^{i(\mathbf{k}+\mathbf{G}')\cdot\boldsymbol{\tau}_\kappa}\zeta^*_{\mu\kappa}(\mathbf{k}+\mathbf{G}')\right) \end{aligned} \tag{2.21}$$

where $v^{loc}_{\kappa}(\mathbf{G})$ and $\zeta_{\mu\kappa}(\mathbf{k}+\mathbf{G})$ are the Fourier components of $v^{loc}_{\kappa}(\mathbf{r})$ and $\zeta_{\mu\kappa}(\mathbf{r})$ respectively. Note that we have excluded from the local potential the $\mathbf{G}=0$ component, since it diverges. This is common practice, and it is justified by the fact that it cancels out with a similar Coulomb divergences in the electron-electron and ion-ion interactions [52]. The Hartree potential in reciprocal space is given by

$$V^{H}_{\mathbf{k}}(\mathbf{G}) = \begin{cases} 4\pi\frac{n(\mathbf{G})}{|\mathbf{G}|^2}, \text{ when } \mathbf{G}\neq 0 \\ 0 \text{ when } \mathbf{G}=0 \end{cases} \tag{2.22}$$

where $n(\mathbf{G})$ is the Fourier transform of the electronic density, and again the diverging component has been removed. Finally the XC term, already diagonal in real space, is calculated using Eq. 2.12 with the charge density 2.17.

The previous expressions cover all the terms appearing in $\hat{\mathcal{H}}$, Eq. 2.9, and are

sufficient to solve the Schrödinger problem 2.7. However, remind that the total energy of the system, defined in Eq. 2.2, contains also the constant ion-ion energy, E_{nn} . In order to calculate such term the Ewald method is commonly employed, which is an efficient way of performing the Coulomb summation over the periodic lattice.

As last remark, note that the plane wave basis set is in principle infinite, and then the sum in Eq. 2.19 is infinite as well. However the coefficients $C_{n,\mathbf{k}+\mathbf{G}}$ associated to plane waves with lower kinetic energy, $(1/2)|\mathbf{k}+\mathbf{G}|^2$, are more relevant than those with a higher energy. Therefore, one usually define an energy cutoff, E^{cutoff}, which identifies a sphere in reciprocal space, and only the plane waves that fall inside such sphere are used while all the others are discarded. In other words only plane waves with wavevectors that satisfy the following relation are considered: $(1/2)|\mathbf{k}+\mathbf{G}|^2 < E^{cutoff}$. This approximation is especially suitable for practical calculations, and the most convenient value for E^{cutoff} must be identified with convergence tests.

2.2 Density functional pertrubation theory

Linear response in the context of DFT can be efficiently calculated in the framework of density functional perturbation theory (DFPT). In this section we will start by briefly summarizing the main concepts and formulas of DFPT; in the following subsections we will give practical examples of their applications in cases that are particularly relevant to the present thesis.

The starting point to develop a perturbation theory is that the external potential, the wavefunctions, the electronic density and the total energy of the electronic problem can be expanded as function of some perturbation parameter, λ [67]:

$$\begin{aligned} V_{ext} &= \sum_n \lambda^n V_{ext}^{(n)} \\ \psi(\mathbf{r}) &= \sum_n \lambda^n \psi^{(n)}(\mathbf{r}) \\ n(\mathbf{r}) &= \sum_n \lambda^n n^{(n)}(\mathbf{r}), \\ E &= \sum_n \lambda^n E^{(n)}, \end{aligned} \tag{2.23}$$

where the superscript is the perturbation order, and the zero order elements are the ground state quantities presented in the previous section. By plugging the electronic charge density expansion into Eq. 2.5 we obtain that the first order electron

density,

$$n^{(1)}(\mathbf{r}) = 4\mathrm{Re}\sum_{i}^{occ}\psi_i^*(\mathbf{r})\psi_i^{(1)}(\mathbf{r}), \tag{2.24}$$

specialized to a nonmagnetic insulator with the occupation factors, $f_i = 2$ for the occupied states and zero otherwise. Similarly, to calculate the response functions, $\psi^{(n)}$, one has to substitute the expressions 2.23 into the Schrödinger problem, Eq. 2.7, and group together the terms of the same order. At first order one recovers the following Sternheimer equation [5]

$$(\mathcal{H}^{(0)} + aP_v - \epsilon_i^{(0)})|\psi_i^{(1)}\rangle = -Q_c V^{(1)}|\psi_i^{(0)}\rangle, \tag{2.25}$$

where P_v and Q_c are the projectors on the valence and conduction bands respectively, a is a generic non zero value that avoids the singularity of the l.h.s., $\epsilon_i^{(0)}$ is the unperturbed eigenvalue of Eq. 2.7, $\mathcal{H}^{(0)}$ is the ground state Hamiltonian defined in Eq. 2.9, and finally $V^{(1)}$ is the first order potential, which is [5]

$$V^{(1)} = V_{ext}^{(1)} + \int \frac{n^{(1)}(\mathbf{r})}{|\mathbf{r}-\mathbf{r}'|}\, d^3r' + \int \frac{dV_{xc}^{(0)}(\mathbf{r})}{dn(\mathbf{r}')} n^{(1)}(\mathbf{r}')\, d^3r'. \tag{2.26}$$

(Here the second and third terms on the r.h.s. come from the Hartree and exchange-correlation potential respectively.) The explicit presence of P_v and Q_c in Eq. 2.25 automatically enforces the parallel transport gauge [27], which prescribes to take the first-order wavefunctions orthogonal to the manifold of the valence states:

$$\langle\psi_i^{(0)}|\psi_j^{(1)}\rangle = 0 \,\forall\{i,j\} \in occ. \tag{2.27}$$

Eq. 2.25, 2.26 and 2.24 establish a closed set of equations that must be solved selfconsistently for the first-order wavefunctions, $|\psi_n^{(1)}\rangle$, and charge density response, $n^{(1)}(\mathbf{r})$.

Thanks to the knowledge of $|\psi_n^{(1)}\rangle$ and $n^{(1)}(\mathbf{r})$, it is then possible to calculate the correction to the total energy of the system, $E^{(2)}$; in the case of time-reversal symmetry it is:

$$E^{(2)} = \sum_{i}^{occ}\langle\psi_i^{(1)}|\hat{V}_{ext}^{(1)}|\psi_i^{(0)}\rangle + \sum_{i}^{occ}\langle\psi_i^{(0)}|V_{ext}^{(2)}|\psi_i^{(0)}\rangle. \tag{2.28}$$

The above expression is a special case of the "$(2n+1)$ theorem" [25] that states that the derivatives of the total energy of a system, $E^{(n)}$, can be obtained with the only knowledge of the wavefunction corrections up to the n-th order. In particular, for

the first order correction to the energy, the $(2n+1)$ theorem reduces to the famous Hellmann-Feynman theorem:

$$E^{(1)} = \sum_{i}^{occ} \langle \psi_i^{(0)} | V_{ext}^{(1)} | \psi_i^{(0)} \rangle. \tag{2.29}$$

2.2.1 Phonon pertrubation

In the following microscopic theory of flexoelectricity, one of the key quantities will be the first order electronic density response to monochromatic lattice displacements. The crystal response to such perturbations is well known the context of DFPT, and here we shell briefly recap the main concepts by specializing the general equations presented in the previous section.

The common procedure, as for example reported by Gonze and Lee [28], consists in considering a monochromatic atomic displacement of the κ atom in the unit cell l along the direction α, defined as

$$\lambda \rightarrow \lambda_{\kappa\alpha} e^{i\mathbf{q}\cdot\mathbf{R}_l}, \tag{2.30}$$

where $\mathbf{R}_l$ identifies the position of the unit cell l. The advantage of using a monochromatic perturbation is that, although in general its periodicity is not commensurate with the crystal lattice periodicity, the first order wavefunctions and charge density can be written in a Bloch type form [28],

$$\begin{aligned} \psi_{m\mathbf{k},\mathbf{q}}^{(\kappa\alpha)}(\mathbf{r}) &= \frac{1}{\sqrt{\Omega}} e^{i(\mathbf{k}+\mathbf{q})\cdot\mathbf{r}} u_{m\mathbf{k},\mathbf{q}}^{(\kappa\alpha)}(\mathbf{r}) \\ n_{\mathbf{q}}^{(\kappa\alpha)}(\mathbf{r}) &= e^{i\mathbf{q}\cdot\mathbf{r}} \overline{n}_{\mathbf{q}}^{(\kappa\alpha)}(\mathbf{r}) = e^{i\mathbf{q}\cdot\mathbf{r}} \sum_{m}^{occ} \frac{4\Omega}{(2\pi)^3} \int d^3k \, u_{m\mathbf{k}}^{(0)*}(\mathbf{r}) u_{m\mathbf{k},\mathbf{q}}^{(\kappa\alpha)}(\mathbf{r}) \end{aligned} \tag{2.31}$$

where $\psi_{m\mathbf{k},\mathbf{q}}^{(\kappa\alpha)}(\mathbf{r})$ and $n_{\mathbf{q}}^{(\kappa\alpha)}(\mathbf{r})$ are the total response functions, while $u_{m\mathbf{k},\mathbf{q}}^{(\kappa\alpha)}(\mathbf{r})$ and $\overline{n}_{\mathbf{q}}^{(\kappa\alpha)}(\mathbf{r})$ are cell-periodic.

In order to calculate the first order functions, it is possible to specialize the Sternheimer equation 2.25, to the case of monochromatic atomic displacements; then Eq. 2.25 becomes [28]

$$(\hat{\mathcal{H}}_{\mathbf{k}+\mathbf{q}}^{(0)} + \alpha \hat{P}_{\mathbf{k}+\mathbf{q}} - \epsilon_{i,\mathbf{k}}^{(0)}) | u_{m,\mathbf{k},\mathbf{q}}^{(\kappa\alpha)} \rangle = -\hat{Q}_{\mathbf{k}+\mathbf{q}} \hat{V}_{\mathbf{k},\mathbf{q}}^{(\kappa\alpha)} | u_{m,\mathbf{k}}^{0} \rangle, \tag{2.32}$$

where $P_{\mathbf{k}} = \sum_n^{occ} |u_{n,\mathbf{k}}^0\rangle\langle u_{n,\mathbf{k}}^0|$ is the projector operator on the valence bands, $\hat{Q}_{\mathbf{k}} = 1 - \hat{P}_{\mathbf{k}}$ is the projector on the conduction bands, and $\hat{V}_{\mathbf{k},\mathbf{q}}^{(\kappa\alpha)}$ is the periodic part of the

first order perturbation potential, $\hat{V}^{(\kappa\alpha)}_{\mathbf{k},\mathbf{q}} = e^{-i(\mathbf{k}+\mathbf{q})\cdot\mathbf{r}}\hat{V}^{(\kappa\alpha)}e^{i\mathbf{k}\cdot\mathbf{r}}$, which can be written as [28]

$$\hat{V}^{(\kappa\alpha)}_{\mathbf{k},\mathbf{q}} = \hat{V}^{sep,(\kappa\alpha)}_{\mathbf{k},\mathbf{q}} + \hat{V}^{loc,(\kappa\alpha)}_{\mathbf{q}} + \hat{V}^{H,(\kappa\alpha)}_{\mathbf{q}} + \hat{V}^{XC,(\kappa\alpha)}_{\mathbf{q}}. \tag{2.33}$$

The explicit expression for the terms of Eq. 2.33 in the case of the plane wave basis set are [28]:

$$\begin{aligned}
\hat{V}^{loc,(\kappa\alpha)}_{\mathbf{q}}(\mathbf{G}) &= -\frac{i}{\Omega}(\mathbf{G}+\mathbf{q})_\alpha\, e^{-i(\mathbf{G}+\mathbf{q})\cdot\boldsymbol{\tau}_\kappa} v^{loc}_\kappa(\mathbf{G}+\mathbf{q}) \\
\hat{V}^{sep,(\kappa\alpha)}_{\mathbf{k},\mathbf{q}}(\mathbf{G},\mathbf{G}') &= \frac{i}{\Omega}\sum_\mu e_{\mu\kappa}\, e^{-i(\mathbf{G}-\mathbf{G}'+\mathbf{q})\cdot\boldsymbol{\tau}_\kappa}\left[i(\mathbf{G}'-\mathbf{G}-\mathbf{q})_\alpha\right]\zeta_{\mu\kappa}(\mathbf{k}+\mathbf{q}+\mathbf{G})\zeta^*_{\mu\kappa}(\mathbf{k}+\mathbf{G}') \\
\hat{V}^{H,(\kappa\alpha)}_{\mathbf{q}}(\mathbf{G}) &= 4\pi\frac{\overline{n}^{\tau_{\kappa\alpha}}_{\mathbf{q}}(\mathbf{G})}{|\mathbf{G}+\mathbf{q}|^2} \\
\hat{V}^{XC,(\kappa\alpha)}_{\mathbf{q}}(\mathbf{r}) &= K_{XC}\overline{n}^{(\tau_{\kappa\alpha})}_{\mathbf{q}}(\mathbf{r})
\end{aligned} \tag{2.34}$$

where the Kernel of the XC term is defined as

$$K_{XC} = \frac{\delta V_{xc}}{\delta n} \tag{2.35}$$

As stressed by Eq. 2.28, using the only knowledge of the first order wavefunctions, it is possible to calculate the second derivative of the total energy; in the present case this would give the atomic force constant matrix

$$C^l_{\kappa\alpha,\kappa'\beta} = \frac{\partial^2 E}{\partial u^0_{\kappa\alpha}\partial u^l_{\kappa'\beta}}, \tag{2.36}$$

where $u^l_{\kappa\alpha}$ is the displacement of the κ atom in the cell l along the direction α. In practice, for the monochrmatic perturbation 2.30 employing the response wavefunctions to the monocromatic perturbation 2.30, one get the Fourier component of the dynamical matrix, defined as

$$C^{\mathbf{q}}_{\kappa\alpha,\kappa'\beta} = \sum_l C^l_{\kappa\alpha,\kappa'\beta}\, e^{i\mathbf{q}\cdot\mathbf{R}_l} \tag{2.37}$$

The explicit expression for $C^{\mathbf{q}}_{\kappa\alpha,\kappa'\beta}$ as function of $|u^{(\kappa\alpha)}_{m\mathbf{k},\mathbf{q}}\rangle$ can be found for example in Ref. [29].

We conclude this section by noting that the choice of the phase in Eq. 2.30 is the standard one because it ensures periodicity in $\mathbf{q}$-space; however, it is not the most convenient when working in a long wave limit, as we will do in the next Chapters.

Indeed, throughout this work, if it is not explicitly mentioned otherwise, we will consider a *different choice for the phase of the monochromatic perturbation*:

$$\lambda \rightarrow \lambda_{\kappa\alpha} e^{i\mathbf{q}\cdot(\mathbf{R}_a+\boldsymbol{\tau}_\kappa)}, \tag{2.38}$$

where $\boldsymbol{\tau}_\kappa$ is the position of the atom κ inside the cell $\mathbf{R}_a$. The extra phase in Eq. 2.38 is essential when performing a long wave analysis since it assigne the correct phase to each sublattice inside a given unit cell [77]. From a practical point of view, the redefinition of the monochromatic perturbation can be easily incorporated as a post-processing step. For example, the electronic response density to the new perturbation, $n_{\mathbf{q}}^{(\tau_{\kappa\alpha})}(\mathbf{r})$, can be obtained starting by the standard response function, $n_{\mathbf{q}}^{(\kappa\alpha)}(\mathbf{r})$, as follows [77]:

$$n_{\mathbf{q}}^{(\tau_{\kappa\alpha})}(\mathbf{r}) = n_{\mathbf{q}}^{(\kappa\alpha)}(\mathbf{r}) e^{i\mathbf{q}\cdot\boldsymbol{\tau}_\kappa}, \tag{2.39}$$

where note the change in the superscript. In a similar way, using Eq. 2.37, the force constant matrix in the case of the new perturbation is obtained as

$$\Phi^{\mathbf{q}}_{\kappa\alpha,\kappa'\beta} = C^{\mathbf{q}}_{\kappa\alpha,\kappa'\beta} e^{i\mathbf{q}\cdot(\boldsymbol{\tau}_{\kappa'}-\boldsymbol{\tau}_\kappa)}. \tag{2.40}$$

2.2.2 Uniform strain perturbation

Another perturbation that is routinely available is the crystal response to a uniform strain. Some of the difficulties encountered for its implementation in the DFPT framework have a common root with the case of uniform strain gradient deformations that we will address in the next Chapter 3. Then, the theory developed by Hamann *et al.* [33] for a uniform strain plays an important conceptual role for this work. Moreover, in our study on inhomogeneous mechanical deformations the results of Ref. [33] will be an important benchmark for the results obtained in Chapter 4. For these reasons here we will briefly revise the theory by Hamann *et al.*.

The main difficulty that hides behind the DFPT formulation of the uniform strain perturbation is that it induces boundary changes of the primitive cell. Indeed the pristine and strained structure have different cell parameters, and therefore the Hilbert space associated to the two crystal structures is different. This clashes with the requirement that the first order wavefunctions can be expanded on the same basis of the unperturbed wavefunctions. The key idea to solve this issue relies on avoiding the use of the Cartesian coordinates, and instead employing the reduced coordinates; in this way the cell size and shape do not change as consequence of a uniform strain, but only the metric tensor does.

Moving to the practical relations, it is possible to specialize the generic procedure outlined previously, to the case of a uniform strain perturbation, $\varepsilon_{\alpha\beta}$. In particular, the response density function, Eq. 2.24 becomes

$$n^{(\alpha\beta)}(\mathbf{r}) = \frac{4}{(2\pi)^3}\sum_{n}^{occ}\int d^3k\, u^{(0)*}_{n,\mathbf{k}}(\mathbf{r})u^{(\alpha\beta)}_{n,\mathbf{k}}(\mathbf{r}) \tag{2.41}$$

where $|u^{(0)}_{n,\mathbf{k}}\rangle$ are the ground state wavefunctions, and $|u^{(\alpha\beta)}_{n,\mathbf{k}}\rangle$ are the first order response functions. The latter can be calculated using the Sternheimer Eq. 2.25, where the perturbation potential, $V^{(1)}$, is obtained by, first, changing the coordinates in the ground state Hamiltonian to the reduced ones, and then deriving such expression respect to the strain component, $\varepsilon_{\alpha\beta}$, reminding that only the metric tensor is explicitly dependent by the strain. When moving to the reduced coordinates, it is easy to see that also the kinetic term shows an explicit dependence by the metric tensor; then in the present case, $V^{(1)}$ can be written as

$$V^{(1)} \rightarrow \mathcal{H}^{(\alpha\beta)}_{\mathbf{k}} = T^{(\alpha\beta)}_{\mathbf{k}} + V^{loc,(\alpha\beta)}_{\mathbf{k}} + V^{sep,(\alpha\beta)}_{\mathbf{k}} + V^{H,(\alpha\beta)}_{\mathbf{k}} + V^{xc,(\alpha\beta)}_{\mathbf{k}}. \tag{2.42}$$

Since in the following Chapter 4 we will recover the explicit formulas for $\mathcal{H}^{(\alpha\beta)}_{\mathbf{k}}$ as a special case of a more general theory, here we report the results of Ref. [33], by using the Cartesian coordinates and the plane wave basis set. Each single term of Eq. 2.42 becomes (for convenience we set $\mathbf{K} = \mathbf{k} + \mathbf{G}$):

$$\begin{aligned}
\hat{T}^{(\alpha\beta)}_{\mathbf{k}} =& K_\alpha K_\beta \\
V^{loc,(\alpha\beta)}_{\mathbf{k}} =& \frac{1}{\Omega}\sum_{\kappa} e^{-i\mathbf{G}\cdot\boldsymbol{\tau}_\kappa}\left[-\delta_{\alpha\beta}v^{loc}_\kappa(\mathbf{G}) + \frac{v'^{loc}_\kappa(\mathbf{G})}{|\mathbf{G}|}G_\alpha G_\beta\right] \\
V^{sep,(\beta)}_{\mathbf{k}}(\mathbf{G},\mathbf{G}') = \frac{i}{\Omega}\sum_{\mu\kappa} e_{\mu\kappa}e^{-i(\mathbf{G}-\mathbf{G}')\cdot\boldsymbol{\tau}_\kappa}&\left[-\delta_{\alpha\beta}\zeta_{\mu\kappa}(\mathbf{K})\zeta^*_{\mu\kappa}(\mathbf{K}')\right. \\
&\left. + K'_\beta\frac{\zeta_{\mu\kappa}(\mathbf{K})}{\partial K_\alpha}\zeta^*_{\mu\kappa}(\mathbf{K}') + K_\beta\zeta_{\mu\kappa}(\mathbf{K})\frac{\partial\zeta^*_{\mu\kappa}(\mathbf{K}')}{\partial K_\alpha}\right]
\end{aligned} \tag{2.43}$$

$$V^{H,(\alpha\beta)}_{\mathbf{k}} = \frac{4\pi}{|\mathbf{G}|^2}\left[n^{(\alpha\beta)}_{\mathbf{G}} - n^{(0)}_{\mathbf{G}}\left(\delta_{\alpha\beta} + \frac{G_\alpha G_\beta}{|\mathbf{G}|^2}\right)\right],$$

where the separable esternal potential defined in Eq. 2.14 has been used. Finally, the exchange-correlation term is most conveniently treated in real space:

$$V^{xc,(\alpha\beta)}(\mathbf{r}) = K_{xc}\left(-\delta_{\alpha\beta}n^{(0)}(\mathbf{r}) + n^{(\alpha\beta)}(\mathbf{r})\right). \tag{2.44}$$

2.2.3 Polarization response

In this thesis we are mainly interested in calculating the polarization response to generic mechanical deformations of crystals, with particular focus on uniform strain gradient. Currently, only the polar response to a cell-periodic deformation λ is a well established topic in the framework of DFPT. For convenience one can divide the total polarization response into two contributions, a pure electronic term, $\overline{P}$, and a lattice-mediated term, P^{ion}, and writing

$$\frac{\partial P}{\partial \lambda} = \frac{\partial \overline{P}}{\partial \lambda} + \frac{\partial P^{ion}}{\partial \lambda}. \tag{2.45}$$

This splitting usually has the advantage that the lattice mediate term is easily calculated as in a point charge model. On the contrary, $\overline{P}$ must be treated in a full quantum-mechanical fashion, and now we will summarize how it can be calculated using the DFPT results.

The frozen-ion polarization response can be written as [5]

$$\frac{\partial \overline{P}_\alpha}{\partial \lambda} = 2\sum_n^{occ} \langle \psi_n^{(0)} | \hat{r}_\alpha | \psi_n^{(\lambda)} \rangle + c.c., \tag{2.46}$$

where $\hat{\mathbf{r}}$ is the position operator. It is well known that such operator is ill-defined in periodic systems. Recalling that, at first order, a perturbation only mixes valence and conduction states, one can rewrite the previous equation as [4]

$$\frac{\partial \overline{P}_\alpha}{\partial \lambda} = 2\sum_v^{occ}\sum_c^{empty} \frac{\langle \psi_v^{(0)} | \left[\hat{\mathcal{H}}^{(0)}, \hat{r}_\alpha\right] | \psi_c^{(0)} \rangle}{\varepsilon_v^{(0)} - \varepsilon_c^{(0)}} \langle \psi_c^{(0)} | \psi_v^{(\lambda)} \rangle + c.c., \tag{2.47}$$

where $\hat{\mathcal{H}}^{(0)}$ and $\varepsilon_m^{(0)}$ is the ground-state Hamiltonian and the associated eigenvectors, the sums over c and v are intended on the conduction (empty) and valence (occupied) states, respectively. The commutator appearing in the last equation is $\left[\hat{\mathcal{H}}^{(0)}, \hat{r}_\alpha\right] = -i\hat{p}_\alpha + [V_{NL}, \hat{r}_\alpha]$, where the last term is due to nonlocal peseudopotentials. This is well defined in periodic boundary conditions [4], and using plane waves basis, in the separable case, one obtains [23]:

$$\langle \mathbf{k}+\mathbf{G} | [V, \hat{r}_\alpha] | \mathbf{k}+\mathbf{G}' \rangle = -i \frac{\partial}{\partial k_\alpha} V_{\mathbf{k}}^{sep}(\mathbf{G}, \mathbf{G}') \tag{2.48}$$

Then, after some manipulation, Eq. 2.47 becomes [5, 28]

$$\frac{\partial \overline{P}_\alpha}{\partial \lambda} = -\frac{4}{(2\pi)^3}\int d^3k \, \langle i u_{n\mathbf{k}}^{(k_\alpha)} | u_{n\mathbf{k}}^{(\lambda)} \rangle, \tag{2.49}$$

where $u_{m,\mathbf{k}}^{(k_\beta)}(\mathbf{r})$ is a new auxiliary quantity that is defined as the ground state derivative with respect its wave vector in the parallel transport gauge, Eq. 2.27,

$$u_{m,\mathbf{k}}^{(k_\beta)}(\mathbf{r}) = \frac{\partial u_{m,\mathbf{k}}^{(0)}(\mathbf{r})}{\partial k_\beta}, \tag{2.50}$$

and it can be calculated in the framework of DFPT by using the following Sternheimer equation [28]

$$(\hat{\mathcal{H}}_{\mathbf{k}}^{(0)} + \alpha \hat{P}_{\mathbf{k}} - \epsilon_{m,\mathbf{k}}^{(0)}) | u_{m,\mathbf{k}}^{(k_\alpha)} \rangle = -\hat{Q}_{\mathbf{k}} \frac{\partial \hat{\mathcal{H}}_{\mathbf{k}}^{(0)}}{\partial k_\alpha} | u_{m,\mathbf{k}}^{(0)} \rangle. \tag{2.51}$$

Note that the $\mathbf{k}$-derivative of $\hat{\mathcal{H}}_{\mathbf{k}}^{(0)}$, in the case of separable pseudopotentials precisely coincides with the commutator in Eq. 2.47: $\partial \hat{\mathcal{H}}_{\mathbf{k}}^{(0)} / \partial k_\alpha = \langle \mathbf{k}+\mathbf{G} | [\hat{\mathcal{H}}^{(0)}, \hat{r}_\alpha] | \mathbf{k}+\mathbf{G}' \rangle$.

We now proceed to specialize this result, Eq. 2.49, to the case of the two perturbations previously discussed: the atomic displacements, and the uniform strain. The polarization response induced by a uniform displacement of a given sublattice, $\boldsymbol{\lambda}_\kappa$, is related to the Born effective charges, $Z^*_{\alpha,\kappa\beta}$, which are defined as [29]

$$Z^*_{\alpha,\kappa\beta} = \Omega \frac{\partial P_\alpha}{\partial \lambda_{\kappa\beta}}, \tag{2.52}$$

where $\mathbf{P}$ is the total macroscopic polarization. They can be split, following Eq. 2.45, as

$$Z^*_{\alpha,\kappa\beta} = Z_\kappa \delta_{\alpha\beta} + \Delta Z^*_{\alpha,\kappa\beta}, \tag{2.53}$$

where Z_κ is the bare pseudopotential charge, while $\Delta Z^*_{\alpha,\kappa\beta}$ is the electronic contribution; the latter can be obtained via Eq. 2.49, where the generic perturbation λ is replaced with the perturbation defined in Eq. 2.30, at $\mathbf{q} = 0$. Then, one obtains [29]

$$\Delta Z^*_{\alpha,\kappa\beta} = -4\frac{\Omega}{(2\pi)^3}\int d^3k \sum_n^{occ} \langle i u_{n,\mathbf{k}}^{(k_\beta)} | u_{n,\mathbf{k},\mathbf{q}=0}^{(\kappa\alpha)} \rangle, \tag{2.54}$$

where $u_{m,\mathbf{k},\mathbf{q}=0}^{(\kappa\alpha)}(\mathbf{r})$ is the $\mathbf{q} = 0$ component of Eq. 2.31.

In a similar way one can look at the macroscopic polarization response to a uniform strain deformation, $\varepsilon_{\alpha\beta}$, which defines the piezoelectric tensor,

$$e_{\alpha\beta\gamma} = \Omega \frac{\partial P_\alpha}{\partial \varepsilon_{\beta\gamma}}. \tag{2.55}$$

Again, one can separate the clamped-ion contribution, $\bar{e}_{\alpha\beta\gamma}$, from the rest [89]

$$e_{\alpha\beta\gamma} = \bar{e}_{\alpha\beta\gamma} + \Delta Z^*_{\alpha,\kappa\delta} \Gamma^\kappa_{\delta\beta\gamma}, \tag{2.56}$$

where $\Gamma^\kappa_{\delta\beta\gamma}$ describes the atomic relaxations induced by the strain $\varepsilon_{\beta\gamma}$ and is defined in term of the routinely available force-response internal-strain, $\Lambda^\kappa_{\alpha\beta\gamma}$ as [89]

$$\Gamma^\kappa_{\alpha\gamma\delta} = \tilde{\Phi}^{(0)}_{\kappa\alpha,\kappa'\beta} \Lambda^{\kappa'}_{\beta\gamma\delta} \tag{2.57}$$

with $\tilde{\Phi}^{(0)}_{\kappa\alpha,\kappa'\beta}$ the pseudo-inverse of $\Phi^{\mathbf{q}=0}_{\kappa\alpha,\kappa'\beta}$.

The frozen-ion term can be calculated by using the first order electronic response function to a uniform strain, $u^{(\alpha\beta)}_{n,\mathbf{k}}(\mathbf{r})$. Indeed, specializing Eq. 2.49, one can demonstrate that [33]

$$\bar{e}_{\alpha\beta\gamma} = 2\frac{\Omega}{(2\pi)^3} \int d^3k \sum_n^{occ} \langle i u^{(k_\alpha)}_{n,\mathbf{k}} | u^{(\beta\gamma)}_{n,\mathbf{k}} \rangle. \tag{2.58}$$

2.2.4 Microscopic current density

In the previous subsection we have discussed the macroscopic polar response to a uniform mechanical deformation. However, in this work we are mainly interested in nonuniform effects, and specifically on strain gradients. Recently an extension of the previous theory was developed [19] in the context of DFPT; here we will briefly revise the main concepts, since they are of fundamental importance for the results presented later.

In order to be able to study the polarization response to a inhomogeneous mechanical deformation, λ, one should explore its intimate connection with the microscopic current density, $J_\alpha(\mathbf{r})$. In the linear regime, the induced polarization, $P^\lambda_\alpha(\mathbf{r}) = \partial P_\alpha(\mathbf{r})/\partial\lambda$, is given by: $P^\lambda_\alpha(\mathbf{r}) = \partial J_\alpha(\mathbf{r})/\partial\dot{\lambda}$, where $\dot{\lambda}$ is the velocity of the perturbation.

In quantum-mechanical terms, the microscopic current density due to a static perturbation λ is

$$\frac{\partial J_\alpha(\mathbf{r})}{\partial\lambda} = 2\sum_v^{occ} \langle \psi_v | \hat{J}_\alpha(\mathbf{r}) | \psi^\lambda_v \rangle + c.c. \tag{2.59}$$

where $\hat{J}_\alpha(\mathbf{r})$ is the current density operator. Since in the following it will be convenient to work in the reciprocal space, one can define the Fourier transform of the current density operator, $\hat{\mathbf{J}}(\mathbf{q}) = 1/\Omega \int_{cell} d^3r\, \hat{\mathbf{J}}(\mathbf{r}) e^{-i\mathbf{q}\cdot\mathbf{r}}$.

In the case of local external potential, the explicit expression for such operator is the well known textbook formula [67]

$$\hat{J}^0_\alpha(\mathbf{r}) = -\frac{\hat{p}_\alpha|\mathbf{r}\rangle\langle\mathbf{r}| + |\mathbf{r}\rangle\langle\mathbf{r}|\hat{p}_\alpha}{2} \tag{2.60}$$

(the superscript "0" reminds that this definition holds only for local potentials), and its Fourier transform is [79]

$$\hat{J}^0_\alpha(\mathbf{q}) = -\frac{1}{\Omega}\int_{cell} d^3r\, \left(\hat{p}_\alpha + \frac{q_\alpha}{2}\right) e^{-i\mathbf{q}\cdot\mathbf{r}}. \tag{2.61}$$

However when nonlocal potential are employed, the definition in Eq. 2.60 breaks down, and an extra nonlocal contribution appears, $\hat{J}^{NC}$, [19]

$$\hat{\mathbf{J}}(\mathbf{q}) = \hat{\mathbf{J}}^0(\mathbf{q}) + \hat{\mathbf{J}}^{NL}(\mathbf{q}). \tag{2.62}$$

$\hat{\mathbf{J}}^{NL}(\mathbf{q})$ shall fulfill some sensible requirements such as satisfying a generalized continuity equation and vanishing in the case of local external potentials. The topic of defining an explicit expression for the nonlocal current density operator is quite complex and was recently treated by Dreyer *et al.* [19]. Since in Chapter 4 we will be interested in a long wave expansion (i.e. $\mathbf{q} \to 0$) of this operator, here we limit ourself to report only the final expression, in such limit, for the cell periodic nonlocal current density operator, $\hat{\mathbf{J}}^{NL}_{\mathbf{k},\mathbf{q}} = e^{-\mathbf{k}\cdot\mathbf{r}}\hat{\mathbf{J}}^{NL}(\mathbf{q})e^{(\mathbf{k}+\mathbf{q})\cdot\mathbf{r}}$ [19] :

$$\hat{J}^{NL}_{\alpha\mathbf{k},\mathbf{q}} \approx -\left(\frac{\partial\hat{V}^{NL}_{\mathbf{k}}}{\partial k_\alpha} + \frac{q_\beta}{2}\frac{\partial^2\hat{V}^{NL}_{\mathbf{k}}}{\partial k_\alpha k_\beta} + \frac{q_\beta q_\gamma}{6}\frac{\partial^3\hat{V}^{NL}_{\mathbf{k}}}{\partial k_\alpha k_\beta \partial k_\gamma}\right) \tag{2.63}$$

where $\hat{V}^{NL}_{\mathbf{k}}$ is defined in Eq. 2.21.

As we said, the induced polarization is related to the perturbation velocity. Using the linear time-dependent perturbation theory, in the case of a monochromatic mechanical deformation defined by the vector $\mathbf{q}$, one obtains [19, 79]

$$\frac{d\overline{P}^{\mathbf{q}}_\alpha}{d\lambda} = 2\sum_v \langle\psi^{(0)}_v|\hat{J}_\alpha(\mathbf{q})|\delta\psi^{(\lambda)}_v(\mathbf{q})\rangle + c.c., \tag{2.64}$$

where $|\delta\psi_v^{(\lambda)}(\mathbf{q})\rangle$ are the *adiabatic* response generated by the external potential, $\hat{\mathcal{H}}^{\lambda}(\mathbf{q})$, and it is defined as

$$|\delta\psi_v^{(\lambda)}(\mathbf{q})\rangle = -i \sum_c^{empty} |\psi_c^{(0)}\rangle \frac{\langle\psi_c^{(0)}|\mathcal{H}^{\lambda}(\mathbf{q})|\psi_v^{(0)}\rangle}{(\varepsilon_v^{(0)} - \varepsilon_c^{(0)})^2}. \tag{2.65}$$

In practice the adiabatic function can be calculated by solving the following Sternheimer equation

$$(\hat{\mathcal{H}}^{(0)}_{\mathbf{k}+\mathbf{q}} + \alpha\hat{P}_{\mathbf{k}+\mathbf{q}} - \epsilon^{(0)}_{n,\mathbf{k}})|\delta u^{(\tau_{\kappa\alpha})}_{n,\mathbf{k},\mathbf{q}}\rangle = -i\hat{Q}_{\mathbf{k}+\mathbf{q}}|u^{(\tau_{\kappa\alpha})}_{n,\mathbf{k},\mathbf{q}}\rangle. \tag{2.66}$$

Eq. 2.64 is a generalization to inhomogeneous cases of the theory presented in Sec. 2.2.3, and it will be fundamental for deriving some of the main results of Chapter 3 and 4.

As sanity check, one can show that in the homogeneous limit Eq. 2.64 reduces to Eq. 2.49. This result follows immediately after observing that for $\mathbf{q} = 0$ the current density operator reduces to the commutator appearing in Eq. 2.47: $\hat{J}_\alpha(\mathbf{q} = 0) = [\hat{\mathcal{H}}_{\mathbf{k}}, \hat{r}_\alpha]$.

Finally, it is useful for the next Chapter 3, to explicitly rewrite the induced polarization, Eq. 2.64, in the case of a monochromatic atomic displacement as defined in Eq. 2.38:

$$\overline{P}^{\mathbf{q}}_{\alpha,\kappa\beta} = 2\sum_n^{occ}\langle\psi_n^{(0)}|\hat{J}_\alpha(\mathbf{q})|\delta\psi_n^{(\tau_{\kappa\beta})}(\mathbf{q})\rangle, \tag{2.67}$$

and the adiabatic wavefunctions are

$$|\delta\psi_v^{(\tau_{\kappa\beta})}(\mathbf{q})\rangle = -i \sum_c^{empty} |\psi_c^{(0)}\rangle \frac{\langle\psi_c^{(0)}|\mathcal{H}^{(\tau_{\kappa\beta})}(\mathbf{q})|\psi_v^{(0)}\rangle}{(\varepsilon_v^{(0)} - \varepsilon_c^{(0)})^2}. \tag{2.68}$$

Chapter 3

Theory of flexoelectricity

In this Chapter we will summarize the state of the art about the recent microscopic theory of the flexoelectric (FxE) effect, together with its implementation in the context of DFPT.

After a formal definition of the flexoelectric tensor, in Sec.3.1.2, we will start by giving the basis of the long wave approach applied to mechanical deformations of crystals. This will allows to establish a general bulk theory of flexoelectricity. As results we will identify three contributions to the FxE tensor: a pure ionic contribution, a pure electronic contribution and a mixed term. The long-wave method will also allows us to recover the microscopic piezoelectric response.

In Sec. 3.1.4 we will discuss the surface contributions, in order to understand their impact on the total FxE response of a macroscopic object. In general, a detailed analysis of this topic is quite complicated; here we will limit ourself to a simplified geometry, which in any case will allow to grasp the main physical effects induced by the surfaces.

Following the results of the long wave analysis, in Sec. 3.2 we will discuss different ways to make the FxE theory computational tractable in the context of DFPT; advantages and disadvantages of the different methods will be reported.

Finally, in Sec. 3.43, in order to obtain a more profound physical meaning of the various contributions to the bulk flexoelectric response, we will summarize the main results of the recent work by Stengel and Vanderbilt [79]. In particular, we will introduce the concept of curvilinear coordinates, which constitute the theoretical background of the original work presented in Chapter 4.

3.1 General theory

3.1.1 Definition of FxE tensor

The flexoelectric effect is defined as the polarization response, $\mathbf{P}$, induced by a strain gradient deformation. It is *linear* respect to the displacement vector field, $\mathbf{u}(\mathbf{r}, t)$. This allows to settle the theory of flexoelectricity in the framework of linear-response theory, where a generic transformation of the unperturbed coordinates, $\mathbf{r}$, is written as follows

$$\mathbf{r}'(\mathbf{r}, t) = \mathbf{r} + \mathbf{u}(\mathbf{r}, t), \tag{3.1}$$

where $\mathbf{r}'$ are the perturbed coordinates. Starting from the displacement field, $\mathbf{u}(\mathbf{r})$, one can define the unsymmetrized "deformation gradient":

$$\tilde{\varepsilon}_{\alpha\beta} = \frac{\partial u_\alpha(\mathbf{r})}{\partial r_\beta}, \tag{3.2}$$

where the Greek letters identify the Cartesian coordinates. The tensor $\tilde{\varepsilon}_{\alpha\beta}$ has a symmetric and an antisymmetric part; the latter is related to rotations of the sample, while the former is the symmetric strain tensor,

$$\varepsilon_{\alpha\beta} = \frac{1}{2}(\tilde{\varepsilon}_{\alpha\beta} + \tilde{\varepsilon}_{\beta\alpha}). \tag{3.3}$$

Two different strain gradient tensors exist, depending on whether one uses $\tilde{\varepsilon}_{\alpha\beta}$ or $\varepsilon_{\alpha\beta}$ in its definition. One can define it as a second gradient of the displacement field (type-I),

$$\eta_{\alpha,\beta\gamma} = \frac{\partial\tilde{\varepsilon}_{\alpha\beta}}{\partial r_\gamma} = \frac{\partial^2 u_\alpha}{\partial r_\beta \partial r_\gamma}, \tag{3.4}$$

symmetric in $\beta \leftrightarrow \gamma$, or as a gradient of the symmetric strain (type-II),

$$\varepsilon_{\alpha\beta,\gamma} = \frac{\partial\varepsilon_{\alpha\beta}}{\partial r_\gamma}, \tag{3.5}$$

which is symmetric in $\alpha \leftrightarrow \beta$. Both strain gradient tensors have the same number of independent components and they are related as follows [38]:

$$\eta_{\alpha\beta,\gamma} = \varepsilon_{\alpha\beta,\gamma} + \varepsilon_{\gamma\alpha,\beta} - \varepsilon_{\beta\gamma,\alpha}. \tag{3.6}$$

Since two different strain gradient tensors exist, then also the FxE tensor has two possible definitions

$$\begin{aligned} \mu^I_{\alpha\beta,\gamma\delta} &= \frac{\partial P_\alpha}{\partial \eta_{\beta,\gamma\delta}} \\ \mu^{II}_{\alpha\delta,\beta\gamma} &= \frac{\partial P_\alpha}{\partial \varepsilon_{\beta\gamma,\delta}}. \end{aligned} \tag{3.7}$$

Both are symmetric in the two last indices, but the meaning of the indices is not the same for the two tensors. Then, in general their individual components differ. Yet, both FxE tensors have 54 independent components for the lowest crystal symmetry. Indeed, a one-to-one relation exists between the two definitions,

$$\mu^{II}_{\alpha\beta,\gamma\delta} = \mu^I_{\alpha\beta,\gamma\delta} + \mu^I_{\alpha\gamma,\delta\beta} - \mu^I_{\alpha\delta,\beta\gamma}. \tag{3.8}$$

The simplest type of crystals for studying the flexoelectric effect are the cubic ones, since they only have three independent components of the flexoelectric tensor. They are usually identified as the longitudinal, μ_{11}, the transverse, μ_{12}, and the

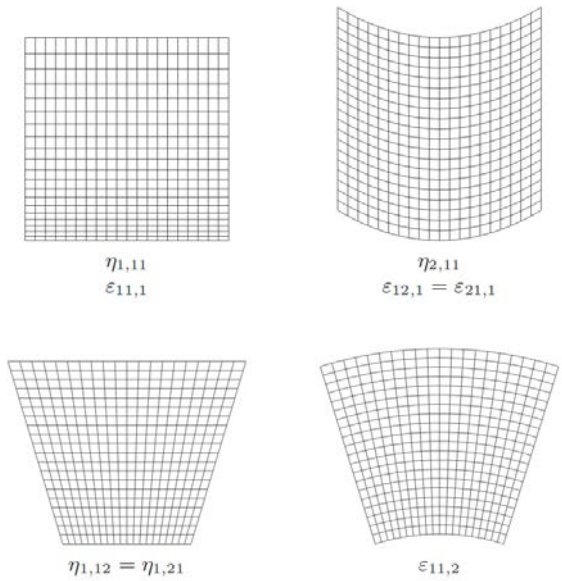

FIGURE 3.1: The independent strain gradient deformations for a cubic crystal, for both the type-I and type-II strain gradient definition (from Ref. [77]).

shear, μ_{44}, which are connected to the type-II definition of Eq. 3.7 as follows:

$$\mu_{11} = \mu^{II}_{xx,xx} \qquad \mu_{12} = \mu^{II}_{xx,yy} \qquad \mu_{44} = \mu^{II}_{xy,xy} = \mu^{II}_{yx,xy}. \tag{3.9}$$

A schematic representation of the associated strain gradient deformation is given in Fig. 3.1.

From Eq. 3.7 it easy to see that in the case of cubic crystals the tensors are symmetric also in the interchange of the first two indices; therefore for cubic crystals the FxE tensor has the same symmetry as the elastic tensor.

3.1.2 Long wave analysis

Long wave analysis has proved to be a really valuable theoretical tool in order to study the macroscopic response of crystals to a variety of perturbations. A notable systematic employment of this method dates back to the Born and Huang's milestone book, "Dynamical Theory of Crystal Lattices" [8]. The great advantage of the long-wave approach is especially clear when dealing with non-periodic perturbations; indeed its key feature is the reformulation of a perturbation as sinusoidal

functions. Thanks to the Fourier transform, periodic functions are easier to treat for establishing a formal theory. Moreover, from a practical point of view, a periodic reformulation is essential to take advantage of DFPT. Chronologically, Tagantsev [80] was the first to employ systematically the long wave approach to study flexoelectricity. His work was based on rigid-ion model. In this section we will present a more general theory of flexoelectricity, based on the work of Stengel [77]. The latter has the double advantage of being based on the long wave analysis, and not restricting itself to the case of point-charge atoms. A previous detailed review can be found in [76].

In continuum theory one can work with the Fourier components of the displacement field of Eq. 3.1 and define a monochromatic mechanical deformation as

$$u_\alpha(\bar{\mathbf{r}}, t) = U_\alpha e^{i\mathbf{q}\cdot\bar{\mathbf{r}} - i\omega t}, \tag{3.10}$$

where $\mathbf{q}$ is the propagation wave vector, U_α is the displacement of a material point in direction α, and ω is the frequency of the perturbation. Such perturbation locally induces a strain and strain gradient deformation that are, respectively,

$$\begin{aligned} \tilde{\varepsilon}_{\alpha\beta}(\bar{\mathbf{r}}, t) &= iq_\beta U_\alpha e^{i\mathbf{q}\cdot\bar{\mathbf{r}}} \\ \eta_{\alpha,\beta\gamma}(\bar{\mathbf{r}}, t) &= -q_\beta q_\gamma U_\alpha e^{i\mathbf{q}\cdot\bar{\mathbf{r}}}. \end{aligned} \tag{3.11}$$

[Note that the deformations in Eq. 3.11 are written in type-I form; similar relations can be written for type-II tensors.]

In a microscopic theory, as it is the case of DFT where the crystal is treated as a discrete lattice, a generic monochromatic phonon is defined as

$$u^l_{\kappa\alpha} = U^{\mathbf{q}}_{\kappa\alpha} e^{i\mathbf{q}\cdot\mathbf{R}^l_\kappa - i\omega t}, \tag{3.12}$$

where l is the index running on different unit cells, κ identifies the sublattice, the Greek letters stands for Cartesian directions, and ω is the frequency. Focusing now on the acoustic phonons, which are defined as the lattice displacements associated to the phonon branches that have zero frequency at $\mathbf{q} = 0$, and by applying the long wave analysis to their equations of motion [8], one arrives at the following result (see Appendix A):

$$U^{\mathbf{q}}_{\kappa\alpha} = U_\beta(\delta_{\alpha\beta} + iq_\gamma \Gamma^\kappa_{\alpha\beta\gamma} - q_\gamma q_\delta N^\kappa_{\alpha\beta\gamma\delta}) + ... \tag{3.13}$$

Each quantity in the above expansion has a precise physical meaning: at order zero in $\mathbf{q}$, $U^{\mathbf{q}}_{\kappa\alpha}$ is the same for each sublattice, U_α; this coincide with a uniform translation

of the whole crystal. The first-order term in Eq. 3.13 contains the tensor $\Gamma^{\kappa}_{\alpha\beta\gamma}$, which describes the sublattice atomic displacement induced by a uniform strain, $\varepsilon_{\beta\gamma}$, we defined in Eq. 2.57. In a similar way, the second order term in Eq. 3.13 describes the sublattice displacements induced by the strain gradient deformation, $\eta_{\beta,\gamma\delta}$ ($N^{\kappa}_{\alpha\beta\gamma\delta}$ is the type-I flexoelectric internal-strain tensor). Both internal relaxation tensors, $\Gamma^{\kappa}_{\alpha\beta\gamma}$ and $N^{\kappa}_{\alpha\beta\gamma\delta}$, can be calculated using the force-constant matrix (as shown in Appendix A), which is a standard quantity available in most code implementations of DFPT.

In addition to the crystal distortion that is associated with the acoustic phonon, the other key quantity that defines the flexoelectric tensor is the polarization response. As we have already pointed out, flexoelectricity is linear with respect to the atomic displacements; thus the macroscopic polarization induced by the collective atomic displacement, $\sum_l u^l_{\kappa\alpha}$, is

$$P_{\alpha}(t) = P^{\mathbf{q}}_{\alpha,\kappa\beta} U^{\mathbf{q}}_{\kappa\beta} e^{i\mathbf{q}\cdot\mathbf{r} - i\omega t} \tag{3.14}$$

where $\overline{\mathbf{P}}^{\mathbf{q}}_{\kappa\beta}$ is the polarization response to the perturbation Eq. 3.12.

Assuming for the moment that we can expand the polarization response function in $\mathbf{q}$, as we did for the displacements, Eq. 3.13, we write:

$$P^{\mathbf{q}}_{\alpha,\kappa\beta} = P^{(0)}_{\alpha,\kappa\beta} - i q_{\gamma_1} P^{(1,\gamma_1)}_{\alpha,\kappa\beta} - \frac{q_{\gamma_1} q_{\gamma_2}}{2} P^{(2,\gamma_1\gamma_2)}_{\alpha,\kappa\beta} + ..., \tag{3.15}$$

where we have adopted the following convention

$$P^{(n,\gamma_1 ... \gamma_n)}_{\alpha,\kappa\beta} = (-i)^n \left. \frac{\partial^n P^{(\mathbf{q})}_{\alpha,\kappa\beta}}{\partial q_{\gamma_1} ... \partial q_{\gamma_n}} \right|_{\mathbf{q}=0} \tag{3.16}$$

In Eq. 3.15 it is easy to recognize that the zero-th order term coincides with the Born effective charges, $P^{(0)}_{\alpha,\kappa\beta} = Z^{\star}_{\kappa,\alpha\beta}$, defined in Eq. 2.53. It is convenient to rewrite the total polar response by splitting the electronic, $\overline{\mathbf{P}}_{\kappa\beta}$ and ionic contributions,

$$\mathbf{P}^{\mathbf{q}}_{\kappa\beta} = \mathbf{P}^{ion\,\mathbf{q}}_{\kappa\beta} + \overline{\mathbf{P}}^{\mathbf{q}}_{\kappa\beta}. \tag{3.17}$$

By inserting Eq.s 3.13 and 3.15 into Eq. 3.14 and collecting the terms up to the second order in $\mathbf{q}$, one can finally write

$$P_{\alpha}(t) = \varepsilon_{\beta\gamma}(t) e_{\alpha\beta\gamma} + \eta_{\beta,\gamma\delta}(t) \mu^{I}_{\alpha\beta,\gamma\delta}, \tag{3.18}$$

where we have used the definitions 3.11. The first term on the r.h.s of Eq. 3.18 is the

piezoelectric contribution, where $e_{\alpha\beta\gamma}$ was defined in Eq. 2.56. Interestingly here we have derived an alternative expression for the clamped-ion contribution that is

$$\bar{e}_{\alpha\beta\gamma} = -\sum_{\kappa} \overline{P}^{(1,\gamma)}_{\alpha,\kappa\beta}. \tag{3.19}$$

Moving to the flexoelectric part of Eq. 3.18, one get that the flexoelctric coefficient is [77]

$$\mu^{I}_{\alpha\beta,\gamma\delta} = \overline{\mu}^{I}_{\alpha\beta,\gamma\delta} - \frac{1}{2}(\Gamma^{\kappa}_{\rho\beta\gamma}\overline{P}^{(1,\lambda)}_{\alpha,\kappa\rho} + \Gamma^{\kappa}_{\rho\beta\lambda}\overline{P}^{(1,\gamma)}_{\alpha,\kappa\rho}) + \frac{1}{\Omega} Z^{\star}_{\kappa,\alpha\rho} N^{\kappa}_{\rho\beta\gamma\lambda}, \tag{3.20}$$

where the clamped-ion term is

$$\overline{\mu}^{I}_{\alpha\beta,\gamma\delta} = \frac{1}{2}\sum_{\kappa} \overline{P}^{(2,\gamma\delta)}_{\alpha,\kappa\beta}. \tag{3.21}$$

Via Eq. 3.8, it is possible to rewrite the FxE coefficient in the type-II form,

$$\mu^{II}_{\alpha\beta,\gamma\delta} = \overline{\mu}^{II}_{\alpha\beta,\gamma\delta} - \Gamma^{\kappa}_{\rho\beta\gamma}\overline{P}^{(1,\lambda)}_{\alpha,\kappa\rho} + \frac{1}{\Omega} Z^{\star}_{\kappa,\alpha\rho} L^{\kappa}_{\rho\beta\gamma\lambda}, \tag{3.22}$$

where $L^{\kappa}_{\rho\beta\gamma\lambda}$ is the correspondent type-II form of $N^{\kappa}_{\rho\beta\gamma\lambda}$ (see Appendix A). Note that in both Eq. 3.22 and Eq. 3.20, three different contributions to the flexolectric tensor are identified: the first term is a pure electronic term, the last term is a pure lattice-mediated term and the second term is a mixed contribution.

In conclusion, we have established a formalism to define the flexoelectric response in a generic crystal. The lattice contribution can be connected with the theory developed in Ref. [80], where a rigid ion-model was considered. In addition, the present derivation also contains the electronic response to a mechanical deformation, which is encoded into the $\mathbf{q}$-expansion of the polarization response function, $\overline{P}^{\mathbf{q}}_{\alpha,\kappa\beta}$. These quantities are the trickiest to calculate. Therefore the bulk of this chapter, starting from the next section, is dedicated to the a detailed analysis of how to deal with the $\mathbf{q}$-expansion terms of the electronic polarization response function. For such presentation we will adopt a DFT point of view, since $\overline{\mathbf{P}}^{\mathbf{q}}_{\kappa\beta}$ is a genuine quantum-mechanical property. Before closing this section however, we will discuss two important points: (i) the validity of the long wave expansion applied to any response functions, such as Eq. 3.15; (ii) the physical impact of surfaces on the global flexoelectric response of a finite sample.

3.1.3 Analyticity of response function around Γ

The previous analysis is based on the long-wave expansion of the response to atomic displacements. In practice, this means that one can expand the response functions around $\mathbf{q} = 0$ as a Taylor series, such as in eq. 3.14. However, from a mathematical point of view, one could ask if this is allowed, i.e. if the response functions are analytic in a neighbourhood of $\mathbf{q} = 0$. Unfortunately this is not the case for insulating crystals, because for $\mathbf{q} \to 0$ their values depend on the direction along which the Γ-point is approached.

The non-analyticity of insulators has its physical origin in the macroscopic electric fields generated by the displacement of charged atoms [59]. The monochromatic atomic displacements described by eq. 3.12 are periodic in the planes perpendicular to the phonon propagation direction, $\hat{\mathbf{q}}$, but in the longitudinal direction they generate a macroscopic electrostatic field that interacts with the other atoms and electronic clouds. This electric field is well known, for example in the context of lattice dynamics, where it is responsible for the splitting between the longitudinal and transverse optical branches at the Γ point. At the lowest order in $\mathbf{q}$, the macroscopic electric field, in the case of polar monochromatic phonon modes, can be approximated as [76]

$$\overline{E}^{(\mathbf{q}\to 0)} \sim -\frac{4\pi}{\Omega}\frac{\hat{\mathbf{q}}\cdot Z^{\star}_{\kappa\beta}}{\hat{\mathbf{q}}\cdot\boldsymbol{\epsilon}\cdot\hat{\mathbf{q}}}, \tag{3.23}$$

where $\boldsymbol{\epsilon}$ is the electronic dielectric constant. From Eq. 3.23 is clear that the induced electric field is function of the phonon propagation direction, $\hat{\mathbf{q}}$, and this dependency propagates into all the response functions, causing their non-analyticity around Γ.

Clearly, in order to be able to perform a long wave expansion one need to deal with the macroscopic electric field. Every time that a long wave approximation is performed in this work, it must be intended that the macroscopic electrostatic interactions have been excluded. Such a choice not only solves the present problem of removing the non-analyticity, but it also recovers the standard definition of all the material constants, e.g. the effective charges, the piezoelctric tensor and the flexoelectric tensor, that are defined in short-circuit electrostatic boundary conditions [63].

From a conceptual point of view, the short-circuit electrostatic boundary conditions could in principle be achieved, by adding to the insulator a low density free electron gas [77], to screen the long range electrostatic interactions generated by the atomic displacements. From a practical point of view, such a regime can be achieved in DFT calculations by setting to zero the $\mathbf{G} = 0$ components of the

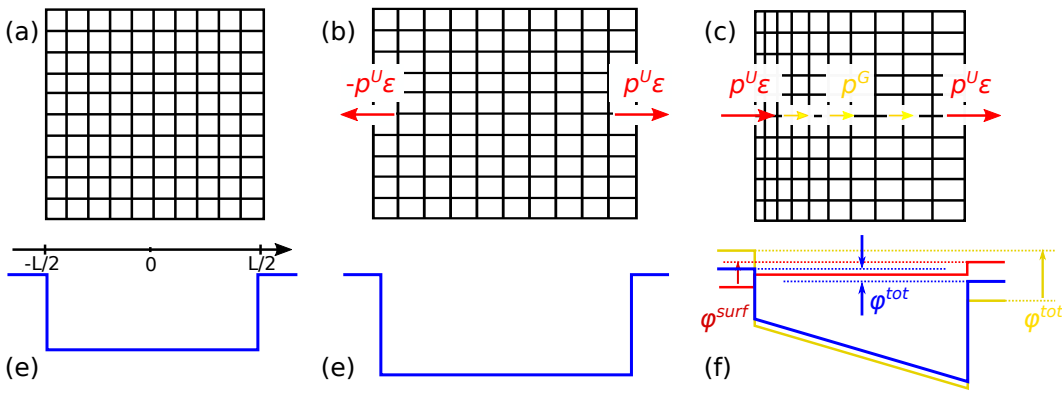

FIGURE 3.2: (a) The pristine slab and the associated potential profile. (b) the same slab under a uniform longitudinal strain; the variation of the surface dipoles, p^U, are marked as red arrows; the variation of the surface dipole produce an dipper potential box; (c) the same slab under a longitudinal strain gradient deformation; the variation of the surface dipole is now in the same direction. The yellow potential profile shows the only contribution of the bulk flexovoltage response (the surface term is not taken into account), while the the blue is the total flexovoltage, bulk+surface.

first-order electrostatic energy and potential, as done in Ref [78].

3.1.4 Surface contributions

The physical properties of crystals are usually divided into two categories based on their behaviour in the limit of a macroscopic sample: a given physical property is a truly bulk property if the details of the surface become irrelevant to determine the total response; on the contrary, one speaks of a "surface property" if the surfaces do matter. Understanding if a certain property has a truly bulk nature or not is of fundamental interest both for theoretical and experimental purposes. Indeed, in the former case, a sample can be prepared by focusing just on the quality of the bulk crystal and without paying much attention to the surfaces, which are usually more demanding to engineer. Theoretically, a bulk physical property can be calculated using periodic boundary conditions, which allows to explicitly simulate only the primitive cell of the crystal, with a considerable saving of time. An example of bulk property is piezoelectricity, as it was demonstrated by Martin [51].

In order to understand where flexoelectricity stands regarding the above calssification, one can think of a free standing slab of a cubic crystal, with two symmetrically terminated surfaces. For clarity, we consider here a slab centered in the origin,

with the normal to the surfaces oriented along $\hat{x}$ and thickness L, which is sufficiently thick in order to recover locally in its center the bulk physical properties of the constituent material (see Fig 3.2-a). Moreover, for simplicity, we will only contemplate longitudinal deformations in such a way that the problem reduces to one dimension.

We start by analyzing the overall polar response of the slab to a uniform mechanical strain, ε (see Fig. 3.2-b). Since the crystal is not piezoelectric, the interior of the slab will not produce any polar response. Moving to the surfaces, one can note that they are by construction piezoelectric, since inversion symmetry is locally broken. Then the uniform strain will result in a change of the surface dipoles. In particular, by focusing on the right surface, one can quantify such change, defining the absolute linear variation induced by a uniform strain as

$$p^U = \frac{2}{L}\int_0^{+\infty} dx\, \frac{\partial P(x)}{\partial \varepsilon}, \tag{3.24}$$

where $P(x)$ is the local polarization along $\hat{x}$, and in the present case is located at the surface regions. However, the changes affecting the two surface dipoles have opposite direction, $p^U_{\pm L/2} = \pm p^U$, because we assumed that the slab is symmetric. It follows that the total polarization response to a uniform strain deformation of a cubic slab is zero: $P^{tot} = (p^U_{L/2} + p^U_{-L/2})\varepsilon = (p^U - p^U)\varepsilon = 0$.

In the case of a strain gradient deformation, $\Delta\varepsilon$ (Fig. 3.2-c), flexoelectricity generates a bulk polar response,

$$p^G = \frac{1}{L}\int_{-\infty}^{+\infty} dx\, \frac{\partial P(x)}{\partial(\Delta\varepsilon)}. \tag{3.25}$$

Regarding the surface response, here one can immediately see that the two surfaces experience an opposite strain. [With reference to Fig. 3.2-c, the local strain in a generic point along the $\hat{x}$ direction is: $(\Delta\varepsilon)x$; then the strain at the two surfaces is opposite: $\varepsilon_{\pm L/2} = \pm(\Delta\varepsilon)\, L/2$.] Therefore, in the case of a strain gradient deformation, the two surface dipole variations do not cancel each other, but they sum up to a non zero surface contribution:

$$P^{surf} = p^U_{L/2}\varepsilon_{L/2} + p^U_{-L/2}\varepsilon_{-L/2} = p^U(\Delta\varepsilon)L. \tag{3.26}$$

Adding together the bulk and surface contributions, one gets the total polar response of the slab to a strain gradient deformation

$$P = p^U(\Delta\varepsilon)L + p^G(\Delta\varepsilon). \tag{3.27}$$

Then, by means of the previous schematic arguments, it is possible to conclude that surface piezoelectricity has macroscopic effects, which must be added to the bulk flexoelectric term in order to capture the total response of a finite crystal.

Another way to analyze the same problem consists in looking at the total flexovoltage of the slab, φ; this is defined as the variation in the electrostatic potential between the two opposite surfaces, ΔV, induced by a strain gradient, $\Delta\varepsilon$,

$$\varphi_x = \lim_{L\to\infty} \frac{1}{L} \frac{d\Delta V}{d(\Delta\varepsilon)}. \tag{3.28}$$

In order to make Eq. 3.28 a sensible definition, ΔV is defined in open circuit (OC) electrostatic boundary conditions (field must vanish away far from the slab surfaces). Note that the flexovoltage quantity has a close relation to the experimental results, since experiments directly measure the current induced by ΔV. Figs. 3.2-[d-f] show the potential profile across the slab for the three different cases: pristine slab, uniform strain, uniform strain gradient. The potential offsets between the vacuum and interior regions of the pristine slab are due to the surface dipoles, and they both change by an equal amount as consequence of the uniform strain, Fig. 3.2-e. Then no variation in the electrostatic potential between the two opposite surfaces is induced. On the contrary, the case of a uniform strain gradient has a double effect on the electrostatic potential 3.2-f: on one side the bulk flexoelectric response induces an internal electric field (yellow line); on the other side the surface dipoles change of an opposite amount, producing an extra potential offset between the two surfaces (red line). The sum of the two effects yields the total change in ΔV, and the total flexovoltage can be written as the sum of a surface and bulk contribution,

$$\varphi^{tot} = \varphi^{surf} + \varphi^{bulk}. \tag{3.29}$$

The bulk term is related to the longitudinal FxE tensor via the relative and vacuum permittivit, ϵ and ϵ_0 respectively, as: $\varphi^{bulk} = \mu/(\epsilon_0\epsilon)$. Again, the surfaces do contribute to the total response in a way that is usually comparable to the bulk effect [78].

While the previous conclusions have been derived for the specific case of a longitudinal deformation, one can show that this result is general. To do this, however, it is necessary to introduce more sophisticated tools: in particular the key point is to settle the analysis of the electronic response of a slab to a strain gradient deformation in a curvilinear frame [74]. This is defined as the frame that is co-moving with the atoms, in such a way that they do not move in a course of a mechanical deformation. A formal introduction to the curvilinear coordinates is presented in

Sec. 3.2.2, while its application to the surface problem is reported in Appendix B.

3.2 Calculation of the electronic bulk FxE response

In this section we will describe a viable strategy to calculate the electronic contribution to the bulk flexoelectric response, $\overline{\mu}_{\alpha\beta,\gamma\delta}$, defined in Eq. 3.21, with particular attention to its practical application in the context of DFPT.

Historically, the first attempt was based on a generalization of the Martin's theory of piezoelectricity [51], where the key quantities to obtain the polar response to a mechanical deformation are the space moments of the electronic density response to atomic displacements. We will revise such theory in Sec. 3.2.1.

This method does not allows to calculate all the independent components of the FxE tensor. In particular the transverse response are inaccessible via the electronic density. A more general theory to calculate the induced polarization, $\overline{P}^{\mathbf{q}}_{\alpha,\kappa\beta}$, was established; this is relies on its direct link with the current density induced by the adiabatic atomic displacements. Combining the long wave expansion of the polarization, Eq. 3.15, with the recent results on the microscopic current density operator discussed in Sec. 2.2.4, we will show in the following Sec. 3.2.2 a feasible way to calculate the full electronic FxE tensor.

3.2.1 Via charge density

Inspired by the seminal paper on piezoelectricity [51], the first remarkable attempt to calculate the microscopic electronic response to a strain gradient deformation was developed by Resta [64]. It is based on a multipolar expansion of the local microscopic variations in the charge density induced by atomic displacements. The key relation to recover the polar response from the electronic response density, $\delta\rho(\mathbf{r})$, is the Poisson equation

$$\nabla \cdot \mathbf{P}(\mathbf{r}) = -\delta\rho(\mathbf{r}). \tag{3.30}$$

This approach is particularly convenient for a practical application to DFT, since in general the electronic density function is a fundamental and routinely available quantity in the framework of DFT calculations.

Unfortunately, subsequent works [36, 77] have demonstrated that not all the independent components of the FxE tensor can be extracted via the charge density response. Still, revising this method is important because: (i) it is functional to understand the following theoretical developments; (ii) it allows to easily establish

general relations that will be used in this work, such as the famous relation between the octupoles moments and the longitudinal FxE tensor; (iii) in the specific case of cubic crystals, if combined with slab calculations, it can be used to extract all the three independent bulk components of the FxE tensor. Here, our presentation will follow closely Ref. [76]

The starting point for the present analysis are the microscopic electronic density responses to a monochromatic lattice displacement, $n_{\mathbf{q}}^{(\tau_{\kappa\beta})}(\mathbf{r})$ (already available in DFPT codes, see Sec. 2.2.1). Since here we are mainly interested in the macroscopic response, it is convenient to introduce the cell integral of the microscopic periodic function,

$$\overline{\rho}_{\kappa\beta}^{\mathbf{q}} = \frac{e}{\Omega}\int_{cell} d^3r\, n_{\mathbf{q}}^{(\tau_{\kappa\beta})}(\mathbf{r}) \tag{3.31}$$

where e is the electronic charge. Inspired by Eq. 3.14, in the linear approximation the macroscopic charge density change induced by a monochromatic lattice displacement is [77]

$$\delta\overline{\rho}(t) = \overline{\rho}_{\kappa\beta}^{\mathbf{q}} U_{\kappa\beta}^{\mathbf{q}} e^{i(\mathbf{q}\cdot\bar{\mathbf{r}}-\omega t)} \tag{3.32}$$

where $U_{\kappa\beta}^{\mathbf{q}}$ is defined in Eq. 3.13. With the same precaution discussed in section 3.1.3, we can now proceed in performing the long wave expansion of the charge density function:

$$\overline{\rho}_{\kappa\beta}^{\mathbf{q}} = \rho^0 - i\overline{\rho}_{\kappa\beta}^{(1,\gamma)} q_\gamma - \frac{\overline{\rho}_{\kappa\beta}^{(2,\gamma\delta)}}{2} q_\gamma q_\delta + i\frac{\overline{\rho}_{\kappa\beta}^{(3,\gamma\delta\lambda)}}{6} q_\gamma q_\delta q_\lambda. \tag{3.33}$$

Note that from a computational point of view, the terms of the previous expansion can be obtained via DFPT; the $\mathbf{q}$-derivative are calculated as finite difference of the electronic response density to for different small value of $\mathbf{q}$ (of the order of 10^{-2} in reduced units).

By substituting Eq. 3.14 and Eq. 3.32 into the Poisson equation 3.30 and grouping together the terms of the same order in $\mathbf{q}$, one gets [76]

$$\overline{\rho}_{\kappa\beta}^{(n,\gamma_1\ldots\gamma_n)} = \sum_l \overline{P}_{\gamma_l,\kappa\beta}^{(n-1,\gamma_1\ldots[\gamma_l]\ldots\gamma_n)}, \tag{3.34}$$

where the symbol $[\gamma_l]$ identifies the absence of the element l from the list.

The previous equation 3.34 can be rewrite employing the more familiar Cartesian multipoles of the charge response to a *single* atomic displacement, also called dynamical multipoles,

$$Q_{\kappa\beta}^{(n,\gamma_1\ldots\gamma_n)} = \int_{\text{all sapce}} d^3r f_{\kappa\beta}(\mathbf{r}) r_{\gamma_1}\ldots r_{\gamma_n} \tag{3.35}$$

where the integrand is the localized density response function in real space, $f_{\kappa\beta}(\mathbf{r}-\mathbf{R}_{l\kappa}) = \partial\rho(\mathbf{r})/\partial u^{l}_{\kappa\beta}$. Using $f_{\kappa\beta}(\mathbf{r})$, the cell-periodic function is equal to [36]

$$e\, n_{\mathbf{q}}^{(\tau_{\kappa\beta})}(\mathbf{r}) = \sum_{l} f_{\kappa\beta}(\mathbf{r}-\mathbf{R}_{l\kappa}) e^{i\mathbf{q}\cdot(\mathbf{R}_{l\kappa}-\mathbf{r})}, \tag{3.36}$$

and therefore the derivatives of the cell average, Eq. 3.31, are

$$\overline{\rho}_{\kappa\beta}^{(n,\gamma_1\cdots\gamma_n)} = \frac{1}{\Omega}\int_{cell} d^3r \frac{\partial^n \rho^{\mathbf{q}}_{\kappa\beta}(\mathbf{r})}{\partial q_{\gamma_1}\ldots\partial q_{\gamma_n}} = \frac{1}{\Omega} Q_{\kappa\beta}^{(n,\gamma_1\cdots\gamma_n)}. \tag{3.37}$$

In conclusion, $\overline{\rho}_{\kappa\beta}^{(n,\gamma_1\cdots\gamma_n)}$ are the dynamical multipoles per cell volume, and Eq. 3.34 connects the long wave expansion of the polarization response with the dynamical multipoles of the induced charge density. The explicit form of the first four $\mathbf{q}$-orders of that relation are:

$$\begin{aligned}
\frac{Q^{(0)}_{\kappa\beta}}{\Omega} &= 0 \\
\overline{Z}^{*}_{\gamma,\kappa\beta} &= \overline{P}^{(0)}_{\gamma,\kappa\beta} \\
\frac{Q^{(2,\gamma\delta)}_{\kappa\beta}}{\Omega} &= \overline{P}^{(1,\gamma)}_{\delta,\kappa\beta} + \overline{P}^{(1,\delta)}_{\gamma,\kappa\beta} \\
\frac{Q^{(3,\gamma\delta\lambda)}_{\kappa\beta}}{\Omega} &= \overline{P}^{(2,\gamma\delta)}_{\lambda,\kappa\beta} + \overline{P}^{(2,\gamma\lambda)}_{\delta,\kappa\beta} + \overline{P}^{(2,\delta\lambda)}_{\gamma,\kappa\beta}
\end{aligned} \tag{3.38}$$

The first line of Eq. 3.38 is a consequence of the fact that the cell integral of electronic charge-density response to an atomic displacement is zero, while in the second line we have used the relation $Q^{(1,\gamma)}_{\kappa\beta} = \Omega\,\Delta Z^{\star}_{\gamma,\kappa\beta}$, where $\Delta Z^{\star}_{\gamma,\kappa\beta}$ is the electronic contribution to the Born effective charge, Eq. 2.53. The third equation in 3.38 is related to the piezoelectric tensor (recall Eq. 3.21) and it can be inverted [77]. The result is the famous equation, first derived by Martin [51], for the electronic contribution to the piezoelectric coefficients:

$$\overline{P}^{(1,\gamma)}_{\alpha\beta} = \frac{1}{2}\left[Q^{(2,\alpha\gamma)}_{\beta} + Q^{(2,\alpha\beta)}_{\gamma} - Q^{(2,\beta\gamma)}_{\alpha}\right], \tag{3.39}$$

where each term has been summed on the sublattice index, κ. Note that Eq. 3.39 is quite similar to the formula that connects the type-I and type-II FxE tensor, Eq. 3.8. Indeed, the quadrupoles $Q^{(2,\alpha\gamma)}_{\beta}$ can be seen as the type-I electronic response to a uniform strain gradient, and $\overline{P}^{(1,\gamma)}_{\alpha,\beta}$ as the type-II.

Finally, reminding that the electronic contribution to the FxE tensor is given by

the second **q**-derivate of the polarization response, Eq. 3.21, then one would be tempted to invert the last relation in Eq. 3.38, to get $\overline{P}^{(2,\gamma\delta)}_{\alpha,\kappa\beta}$. However, just by counting the independent components of both $Q^{(3,\beta\gamma\delta)}_{\kappa\alpha}$ and $\overline{P}^{(2,\gamma\delta)}_{\alpha,\kappa\beta}$ tensor, one get that the former has only 30 while the latter has 54 independent entries [77], and this makes impossible to invert the last relation in Eq. 3.38. Therefore, despite this approach is very appealing from the point of view of DFPT calculations, this strategy does not allow to determine all the clamped-ion independent components of the FxE tensor.

Another way to understand the impossibility of using the Poisson equation in order to extract the full polarization response is based on the observation that Eq. 3.30 only connects the longitudinal part of **P** (i.e. the curly free) to the charge density. The information on the solenoidal component of **P**, which in general differs from zero, can not be accessed via charge density. Summarizing, the knowledge of the electronic charge density response function only gives access to the longitudinal components of the FxE tensor. This can be expressed using the well known relation between the longitudinal octupoles and the associated longitudinal flexoelectric tensor component [64],

$$\overline{\mu}_{\hat{\mathbf{q}}} = \frac{Q^{(3)}_{\hat{\mathbf{q}}}}{6\Omega}, \tag{3.40}$$

where $\overline{\mu}_{\hat{\mathbf{q}}} = \overline{\mu}_{\alpha\beta\gamma\delta}\hat{\mathbf{q}}_\alpha\hat{\mathbf{q}}_\beta\hat{\mathbf{q}}_\gamma\hat{\mathbf{q}}_\delta$ and $Q^{(3)}_{\hat{\mathbf{q}}} = \sum_\kappa Q^{(3,\beta\gamma\delta)}_{\alpha\kappa}\hat{\mathbf{q}}_\alpha\hat{\mathbf{q}}_\beta\hat{\mathbf{q}}_\gamma\hat{\mathbf{q}}_\delta$.

In the specific case of cubic crystals there are only two independent longitudinal directions, which are usually identified with the [100] and [110] Cartesian directions. Therefore the corresponding longitudinal flexoelctric coefficients that can be obtained using the charge density response are defined, in terms of the Cartesian tensor 3.9, as follows:

$$\begin{aligned} \mu_{[100]} &= \mu_{11}, \\ \mu_{[110]} &= \mu_{11} + \mu_{12} + 2\mu_{44}. \end{aligned} \tag{3.41}$$

It is interesting to note that, only for cubic crystals, the transverse component, μ_{12}, can be calculated using a slab geometry [74]. The proof of this statement needs the concept of curvilinear coordinates (Sec. 3.43) and is reported in Appendix B.

3.2.2 Via current density

In order to be able to get all the bulk independent components of the clamped-ion flexoelectric tensor, one should explore the intimate connection between the microscopic current density and the macroscopic inhomogeneous polarization.

In quantum-mechanics terms we have already discuss the relation between the microscopic current density operator and the macroscopic polarization response in Sec. 2.2.4, together with its generalization to the case of nonlocal external potentials. In practice, the electronic polarization induced by a monochromatic atomic displacement, Eq. 3.21, can be calculated via Eq. 2.67,

$$\overline{\mu}^{I}_{\alpha\beta,\gamma\delta} = -\frac{1}{2}\sum_{\kappa}\frac{\partial^2 \overline{P}^{\mathbf{q}}_{\alpha,\kappa\beta}}{\partial q_\gamma \partial q_\delta}. \tag{3.42}$$

Note that the approximation of the current density operator in the case of non-local pseudopotential, Eq. 2.63, is just enough for our purpose; indeed the electronic FxE response is proportional to the second order term of the long wave expansion of $\overline{\mathbf{P}}^{\mathbf{q}}_{\kappa\beta}$, and in Eq. 2.63 is precisely reported the expression for the current density operator up to the second order in $\mathbf{q}$.

3.3 Revised analysis in curvilinear coordinates

When dealing with time-dependent problems, as in the case of the microscopic current density induced by an adiabatic displacement, the boundary conditions of the Hamiltonian change during the perturbation and therefore issues related to the physical representation of the quantum-mechanical observables can rise. The origin of these issues can be understood using the case of uniform strain deformations; Lets suppose to have an infinite one dimensional atomic chain and to be interested in the response to a *small* uniform strain, ε. Then, the ion located at R_a will be displaced of an amount $u_a = R_a\varepsilon$. Unfortunately the perturbation u_a has two problems: (i) it is not small for atoms that are far from the origin; (ii) it is implicitly dependent by the arbitrary choice of the origin of the coordinate system. The former point clearly contradicts the hypothesis of small perturbations, while the latter contrasts with the concept of proper mechanical response of crystals, which prescribes that the response must only be function of the relative distances between points in the crystals and not of their absolute position with respect to some arbitrary coordinate origin [85]. In order to solve such problems in the context of DFPT, Hamann *et al.* [33] have derived the crystal response to a uniform strain perturbation in reduced coordinates; then no explicit displacement of the atoms takes place and the boundary conditions remain unchanged during the perturbation. We have discussed some practical details of this procedure in Sec. 2.2.2. Clearly, these same problems are expected to be even more severe in the case of strain gradient deformations, where the displacement field of the atomic positions grows quadratically

respect to the arbitrary coordinate origin.

Recently, Stengel and Vanderbilt [79], inspired by Hamann *et al.* [33], have tackled these issues from their very root, by considering a generic mechanical deformation and incorporating a convenient coordinate transformation into the time-dependent Schrödinger equation. It follows that the Schrödinger problem is formulated in a curvilinear frame where the ions do not move, and all the effects of the mechanical perturbation are incorporated in a change of the real space metric.

One of the main results of employing the curvilinear coordinates is that the polarization response to an inhomogeneous deformation is naturally divided into two contributions: a "static" term, which is linear in the amplitude of the distortion; a "dynamic" term, which is proportional to the velocity of the distortion. This same partition applies also to the flexoelectric response, where the dynamic term is responsible for a peculiar contribution, proportional to the magnetic susceptibility of the crystal. Since these results will be the starting point to develop an efficient strategy in order to remove the dynamical term from the Cartesian Eq. 3.42, which will be the central goal of the next Chapter, here we revise in some detail the main conclusion of Ref [79].

In all generality one can consider the following time-dependent coordinate transformation, corresponding to the mechanical deformation of Eq. 3.1,

$$\mathbf{r} = \boldsymbol{\xi} + \mathbf{u}(\boldsymbol{\xi}, t), \tag{3.43}$$

where $\mathbf{r}$ and ξ are the Cartesian and curvilinear coordinates, respectively. Plugging this transformation into the time dependent Schrödinger equation, one obtain the following curvilinear Hamiltonian [79]:

$$\hat{\tilde{\mathcal{H}}} = \frac{1}{2}(\hat{\tilde{p}}_\beta - A_\beta)(\mathbf{g}^{-1})_{\beta\gamma}(\hat{\tilde{p}}_\gamma - A_\gamma) + \hat{\tilde{V}} + \hat{\tilde{V}}_{geom} - \frac{1}{2}\phi \tag{3.44}$$

where the tilde symbol identifies the curvilinear quantities, $\hat{\tilde{p}}_\beta = \partial/\partial\xi_\beta$ is the momentum operator, $g_{\beta\gamma}$ is the metric tensor defined as

$$g_{\beta\gamma} = \left(\frac{\partial r_i}{\partial \xi_\beta} \frac{\partial r_i}{\partial \xi_\gamma} \right), \tag{3.45}$$

A_β and ϕ are a vector and scalar potential defined as

$$\begin{aligned} \phi &= \frac{\partial r_i}{\partial t}\frac{\partial r_i}{\partial t} \\ A_\beta &= \frac{\partial r_i}{\partial \xi_\beta}\frac{\partial r_i}{\partial t}|_{\boldsymbol{\xi}}, \end{aligned} \tag{3.46}$$

$\hat{\tilde{V}}_{geom}$ comes from the kinetic term and is equal to

$$\begin{aligned} \hat{\tilde{V}}_{geom} &= \frac{1}{2}\mathcal{A}_\alpha g^{\alpha\beta}\mathcal{A}_\beta + \frac{1}{2}\partial_\alpha(g^{\alpha\beta}\mathcal{A}_\beta) \\ \mathcal{A}_\alpha &= \frac{1}{2h}\frac{\partial h}{\partial \xi_\alpha} \\ h &= \det\left(\frac{\partial r_i}{\partial \xi_\alpha}\right), \end{aligned} \tag{3.47}$$

and $\hat{\tilde{V}}$ contains all the remaining potential terms written explicitly in curvilinear coordinates.

In practice, for the purpose of the present discussion, we consider a monochromatic acoustic phonon perturbation: $\mathbf{u}_{a\kappa} = \boldsymbol{\lambda} e^{i(\boldsymbol{R}_{a\kappa}\cdot\mathbf{q}-\omega t)}$, where $\boldsymbol{R}_{a\kappa}$ identify the position of the atom κ in the cell a. [Note that this perturbation of frame is associated with the collective displacement of an acoustic phonon, since all the atoms undergo to the same displacement $\boldsymbol{\lambda}$.] Then, the associated coordinate transformation is given by Eq. 3.43, with

$$\mathbf{u}(\boldsymbol{\xi}, t) = \boldsymbol{\lambda}(t) e^{i\boldsymbol{\xi}\cdot q}. \tag{3.48}$$

By only retaining the term up to the first order in $\boldsymbol{\lambda}$, we obtain that the scalar potential does not contribute, the geometric potential is simply an additive $\mathbf{q}$-dependent constant (see next Chapter), and the effective vector potential $\mathbf{A}$, reduces to the velocity of the perturbation, $\mathbf{A} = \dot{\boldsymbol{\lambda}}$.

The explicit presence of the velocity of the perturbation in the curvilinear Hamiltonian allows to group its effect in a "dynamical" term. Then, the bulk polarization can be written as the sum of two contributions [79]

$$\overline{P}^{\mathbf{q}}_{\alpha\beta} = \overline{P}^{\mathbf{q},stat}_{\alpha\beta} + \overline{P}^{\mathbf{q},dyn}_{\alpha\beta}; \tag{3.49}$$

the static term, $\overline{P}^{\mathbf{q},stat}_{\alpha\beta}$, is the curvilinear equivalent of the Cartesian Eq. 2.67,

$$\overline{P}^{\mathbf{q},stat}_{\alpha\beta} = 2\sum_v \langle \psi_v | \hat{\mathcal{J}}_\alpha(\mathbf{q}) | \delta\psi^{(\beta)}_v(\mathbf{q}) \rangle, \tag{3.50}$$

where $\hat{\mathcal{J}}(\mathbf{q})$ is the Fourier transform of the current density operator defined in Sec. 2.2.4, but now the Cartesian coordinates are replaced by the curvilinear, and $|\delta\psi_n^{(\beta)}(\mathbf{q})\rangle$ is the adiabatic response function generated by the static curvilinear Hamiltonian,

$$\hat{\mathcal{H}}^{(\beta)}(\mathbf{q}) = \frac{\partial\hat{\tilde{\mathcal{H}}}(\mathbf{q})}{\partial\lambda_\beta} \tag{3.51}$$

[where we have made explicit the $\mathbf{q}$-dependence], and in analogy with Eq. 2.65 is defined as

$$|\delta\psi_v^{(\beta)}(\mathbf{q})\rangle = -i\sum_c |\psi_c\rangle \frac{\langle\psi_c|\mathcal{H}^{(\beta)}(\mathbf{q})|\psi_v\rangle}{(\epsilon_v-\epsilon_c)^2}. \tag{3.52}$$

The explicit calculation of these response wavefunctions will be one of the main achievements of the next Chapter 3. The dynamic term, $\overline{P}_{\alpha\beta}^{\mathbf{q},dyn}$, is defined as

$$\overline{P}_{\alpha\beta}^{\mathbf{q},dyn} = 2\sum_v \langle\psi_v|\hat{\mathcal{J}}_\alpha(\mathbf{q})|\psi_v^{(\dot{\lambda}_\beta)}(\mathbf{q})\rangle + \frac{N}{\Omega}\delta_{\alpha\beta}, \tag{3.53}$$

where the second term on the r.h.s. originates from an additional piece that appears in the curvilinear definition of current density operator [79], with N equal to the total number of electrons in the valence band and Ω the cell volume, and $|\psi_v^{(\dot{\lambda}_\beta)}(\mathbf{q})\rangle$ is [79]

$$|\psi_v^{(\dot{\lambda}_\beta)}(\mathbf{q})\rangle = \sum_c |\psi_c\rangle \frac{\langle\psi_c|\mathcal{H}^{\dot{\lambda}_\beta}(\mathbf{q})|\psi_v\rangle}{(\epsilon_v-\epsilon_c)}. \tag{3.54}$$

where $\mathcal{H}^{\dot{\lambda}}$ is dynamical first order contribution to the curvilinear Hamiltonian, $\hat{\mathcal{H}}^{\dot{\lambda}_\beta}(\mathbf{q}) = \frac{\partial\hat{\tilde{\mathcal{H}}}(\mathbf{q})}{\partial\dot{\lambda}_\beta}$.

Clearly the same division as in Eq. 3.49 applies to the flexoelectric tensor,

$$\overline{\mu}_{\alpha\beta,\gamma\delta} = \overline{\mu}'_{\alpha\beta,\gamma\delta} + \overline{\mu}^{dyn}_{\alpha\beta,\gamma\delta} \tag{3.55}$$

where $\overline{\mu}'_{\alpha\beta,\gamma\delta}$ and $\overline{\mu}^{dyn}_{\alpha\beta,\gamma\delta}$ are the static and dynamic contribution, respectively. Interestingly, it is possible to show that the dynamical term is proportional to the magnetic susceptibility tensor, $\chi^{mag}_{\alpha\beta}$, which is defined as the proportionality tensor between the magnetization vector, $\mathbf{M}$, and the magnetic field, $\mathbf{B}$:

$$M_\alpha = \chi^{mag}_{\alpha\beta} B_\beta \tag{3.56}$$

This can be seen as follows: consider a monochromatic $\mathbf{A}$-field that changes linearly in space, then it induces the following current density (remind the two basic

relations $\boldsymbol{B} = \nabla \wedge \mathbf{A}$ and $\boldsymbol{J} = -\nabla \wedge \mathbf{M}$):

$$J_\alpha = \epsilon_{\alpha\rho\gamma}\, q_\rho\, \chi_{\gamma\delta}\, \epsilon_{\delta\omega\beta}\, q_\omega\, A_\beta, \tag{3.57}$$

where $\epsilon_{\alpha\rho\gamma}$ is the Levi-Civita symbol. Since in our case the effective vector potential is equal to the velocity of the perturbation, then the derivative of J_α respect to $\mathbf{A}$ gives the dynamical contribution to the polarization

$$\overline{P}^{\mathbf{q},dyn}_{\alpha\beta} \sim \epsilon_{\alpha\rho\gamma}\, q_\rho\, \chi_{\gamma\delta}\, \epsilon_{\delta\omega\beta}\, q_\omega \tag{3.58}$$

Finally, the corresponding flexoelectric tensor is obtained by performing the second $\mathbf{q}$-derivative of the previous expression [79], and the type-I expression is

$$\overline{\mu}^{I\,dyn}_{\alpha\beta,\gamma\delta} = \frac{1}{2}\sum_{\omega\rho}\left(\epsilon_{\omega\alpha\gamma}\epsilon_{\rho\beta\delta} + \epsilon_{\omega\alpha\delta}\epsilon_{\rho\beta\gamma}\right)\chi^{mag}_{\omega\rho}, \tag{3.59}$$

which is indeed proportional to the magnetic susceptibility tensor.

An easy understanding on the physical origin of the dynamical contribution can be obtained by means of the schematic cartoons reported in Fig. 3.3, where we consider a cubic crystal slab perturbed by a uniform shear strain gradient. The decomposition of the crystal into small pieces, Fig. 3.3-(a), shows that each of these pieces experience a rotation. By Larmor's theorem, the effects of a uniform rotation are equivalent to the effects of a uniform magnetic field. An external magnetic field generates surface currents that ultimately produce a divergenceless surface polarization. Since the pieces of the crystal are rotating of a different angle, which linearly grows along the transverse direction, then the induced surface polarization differs between each peace. Summing up to reconstruct the full crystal, one can observe that an additional uniform bulk polarization contribution rises, the red arrows in Fig. 3.3, which is is precisely $\overline{\mathbf{P}}^{\mathbf{q},dyn}_{\beta}$, Eq. 3.53.

Crucially, Fig. 3.3 also shows that surface currents are induced, green arrows in Fig. 3.3. Clearly, they exactly cancel the previous bulk term, since both their origin is the same *divergenless* polarization.

In a more formal way one can regard at the presence of an inhomogeneous effective vector potential, $\mathbf{A}$, in the curvilinear Hamiltonian, Eq. 3.44, as describing an external magnetic field acting on the system, which ultimately generates a *solenoidal* current density. We have already shown that here the effective vector potential is proportional to the velocity of the perturbation, $\dot{\boldsymbol{\lambda}}$, and therefore it describes the effects of the local rotation of the sample, which are proportional to the curl of $\dot{\boldsymbol{\lambda}}$.

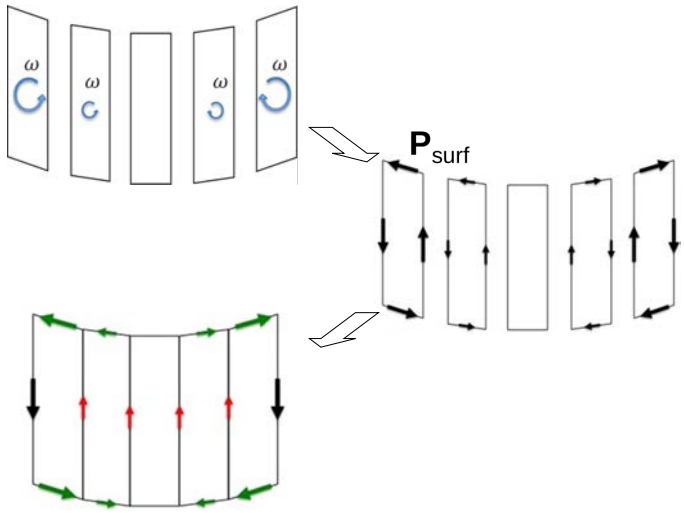

FIGURE 3.3: The logical steps to understand the origin of an extra contribution to the bulk flexoelectric response that is generated by the local rotation of the sample. The local gradient rotations of the sample induce a solenoidal current density response (via the Larmor's theorem) whose effects is to induce a solenoidal polarization. The bulk contribution of such polarization is different from zero (red arrows), but is cancelled by an equal and opposite surface term (green arrows).

Then, the effects of the gradient rotations that can follow a strain gradient perturbation cause a solenoidal current that ultimately generates a divergenceless polarization.

Since in the case of flexoelectricity surfaces do condition to the global response of a bounded sample and what really matters in experimental measurements is the sum of the bulk and surface response, it is a sensible choice is to discard $\overline{\mu}^{dyn}_{\alpha\beta,\gamma\delta}$ and define the bulk FxE tensor as simply $\overline{\mu}'_{\alpha\beta,\gamma\delta}$. Obviously, the previous curvilinear analysis is showing us the strategy to achieve such goal; one has to directly calculate the adiabatic response to a mechanical perturbation in curvilinear coordinates, using the Hamiltonian, $\hat{\mathcal{H}}^{(\beta)}(\mathbf{q})$. How it can be done in practice, in the framework of DFPT, is the subject of the next Chapter 4.

We conclude this section, noticing that the dynamical contribution to the FxE response can also be isolated by using the proportionality relation with the susceptibility tensor, Eq. 3.59. This was the strategy employed in Ref. [19], where the authors have performed an independent calculation for the susceptibility tensor, and removed the dynamical contribution in a post processing step. In particular

for cubic crystals only the transverse and shear term have a nonzero dynamical contribution, which are

$$\mu_{11,22}^{II,dyn} = -2\chi^{mag} \quad \mu_{12,12}^{II,dyn} = \chi^{mag}, \tag{3.60}$$

Chapter 4

The metric wave approach

In Chapter 3 we have reviewed the recent developments of the microscopic theory of flexoelectricity, based on a long wave expansion of the response to an acoustic phonon. As a result, we have identified two contributions to the total bulk FxE tensor: a clamped-ion and a lattice-mediated term. While the lattice-mediated contributions are relatively easy to calculate, since they can be treated similarly to the case of a point-charge model [80], the clamped-ion term is the most difficult to obtain, since it needs the knowledge of the microscopic current-density operator. Despite its fundamental nature from a computational point of view, a practical implementation of the microscopic current-density operator in the context of non-local pseudopotentials is far from being trivial and only recently was developed and implemented [19]. This has allowed for a methodological breakthrough in the calculation of all the independent components of the bulk flexoelectric tensor, by using a primitive cell, via Eq. 2.67.

However, following the curvilinear analysis of Ref. [79], we have also shown in Chapter 3 that further subtleties affect the bulk FxE tensor as defined in Eq. 3.42. It turns out that, even at the clamped-ion level, there are two contributions: a dynamic and a static term, Eq. 3.49. In particular, the dynamical term is a consequence of the local rotations of the sample, and it is proportional to the diamagnetic susceptibility tensor. To understand its physical relevance, it is essential to remind that the flexoelectricity is not a pure bulk property and surfaces contribute to the total response of a finite sample, making the separation between the two contributions not unique. Then, in a bounded sample only the static term is relevant to the electromechanical response, since the dynamical electronic response, which consist in a purely solenoidal current, is exactly canceled by an opposite surface response. For this reason, in Ref. [19] an independent calculation of the diamagnetic susceptibility was performed in order to isolate the physically relevant static part.

Clearly a simpler and more efficient approach for calculating the static response is directly using the curvilinear frame, eliminating the need of any post-processing step connected with the diamagnetic correction. To this aim, one has to describe an acoustic phonon in the frame that is co-moving with the atoms. Since in this frame the atoms do not move and all the information on the perturbation is encoded in the macroscopic displacement fields and in its gradients (e.g. the metric tensor), we identify such perturbation as the "metric perturbation".

In this Chapter we will provide the formalism to implement the metric perturbation in the context of separable atomic pseudopotentials in the Kleinman-Bylander [43] form. Remarkably, we will establish a rigorous link between the response in the Cartesian and co-moving frames, which shows that the respective first-order wave functions are related by a simple geometric contribution -i.e. one that can

be expressed in terms of ground-state quantities-, together with the implications of this result on the observables of interest (charge density and current).

Based on these results, we then proceed to the implementation and testing of the monochromatic metric perturbation, identified by a (generally) incommensurate wavevector $\mathbf{q}$, in the context of DFPT. The wave-function response to such a metric perturbation is then used as input for calculating the current-density response, as recently developed in Ref. [19], and outlined in Sec. 2.2.4. This results in a methodology that allows to calculate the flexoelectric coefficients with unprecedented accuracy and computational efficiency. In particular, our numerical tests clearly demonstrate that the present method yields faster convergence with respect to $\mathbf{k}$-point mesh density and other computational parameters when compared with previous approaches. All these results are rationalized in terms of the aforementioned relationship between the first-order wave functions in the curvilinear and laboratory frames.

From the formal point of view, this work also establishes a direct link between the perturbative treatment of phonon and uniform strain perturbations, which previously were regarded as two conceptually distinct sub-areas of DFPT.

The Chapter is organized as follows: We will first derive the explicit expression of the linear metric perturbation Hamiltonian, which is suitable for an implementation into a DFPT code. Second, we will clarify the connection existing between the first order response wave functions to a metric and to a standard acoustic phonon perturbation. Third, we will report extensive tests of the metric perturbation implementation, followed by the calculation of the static bulk FxE tensor for selected materials.

4.1 Metric perturbation in the context of DFPT

The starting ingredient for the metric perturbation is a "clamped-ion" acoustic phonon. This is a collective lattice mode where all atoms are displaced according to $\mathbf{u}_{a\kappa} = \boldsymbol{\lambda} e^{i\mathbf{R}_{a\kappa}\cdot\mathbf{q}}$. (Note that in comparison with standard phonon perturbation, Eq. 2.38, here the same displacement amplitude for all sublattices, $\lambda_{\kappa\beta} = \lambda_\beta$, is used.) Next, we describe such a monochromatic acoustic wave *in the curvilinear frame that is co-moving with the atoms* (Fig. 4.1). This means that we combine the aforementioned displacement pattern with a simultaneous coordinate transformation that brings every atom back to its original position,

$$\mathbf{r} = \boldsymbol{\xi} + \boldsymbol{\lambda} e^{i\boldsymbol{\xi}\cdot\boldsymbol{q}}, \tag{4.1}$$

where $\boldsymbol{\xi}$ are the curvilinear coordinates.

By performing this double operation in the context of DFPT, we shall obtain the "static" first-order Hamiltonian describing a monochromatic metric wave perturbation, Eq. 3.51. After isolation the phase factors, $\hat{\mathcal{H}}^{(\beta)}_{\mathbf{k},\mathbf{q}} = e^{-i(\mathbf{q}+\mathbf{k})\cdot\mathbf{r}}\hat{\mathcal{H}}^{(\beta)}(\mathbf{q})e^{i\mathbf{k}\cdot\mathbf{r}}$, this Hamiltonian can be conveniently written as

$$\hat{\mathcal{H}}^{(\beta)}_{\mathbf{k},\mathbf{q}} = \hat{H}^{(\beta)}_{\mathbf{k},\mathbf{q}} + \hat{V}^{(\beta)}_{\mathbf{q}}, \tag{4.2}$$

where we have split the "external potential", $\hat{H}^{(\beta)}_{\mathbf{k},\mathbf{q}}$, from the self-consistent contribution,

$$V^{(\beta)}_{\mathbf{q}}(\mathbf{r}) = \int d^3r'\, K_{\mathrm{Hxc}}(\mathbf{r},\mathbf{r}')e^{i\mathbf{q}\cdot(\mathbf{r}'-\mathbf{r})}n^{(\beta)}_{\mathbf{q}}(\mathbf{r}'), \tag{4.3}$$

that depends on the first-order charge density,

$$n^{(\beta)}_{\mathbf{q}}(\mathbf{r}) = \frac{4}{N_{\mathbf{k}}}\sum_{m\mathbf{k}}\langle u^{(0)}_{m\mathbf{k}}|\mathbf{r}\rangle\langle\mathbf{r}|u^{(\beta)}_{m\mathbf{k},\mathbf{q}}\rangle, \tag{4.4}$$

via the Hartree, and exchange-correlation kernel,

$$K_{\mathrm{Hxc}}(\mathbf{r},\mathbf{r}') = \frac{\delta V_{\mathrm{Hxc}}(\mathbf{r})}{\delta n(\mathbf{r}')}\Big|_{n^{(0)}} = \frac{\delta^2 E_{\mathrm{Hxc}}}{\delta n(\mathbf{r})\delta n(\mathbf{r}')}\Big|_{n^{(0)}}. \tag{4.5}$$

In contrast to most perturbations, however, the external potential here takes contributions from all individual pieces of the Hamiltonian, including the kinetic, pseudopotential, Hartree and exchange-correlation terms. (The situation is analogous to the strain perturbation introduced by Hamann *et al.* [33].) In particular, taking advantage of the expression for the curvilinear Hamiltonian, reported in the previous Eq. 3.44, one obtain for the self-consistent contribution of Eq. 4.2

$$\hat{H}^{(\beta)}_{\mathbf{k},\mathbf{q}} = \hat{T}^{(\beta)}_{\mathbf{k},\mathbf{q}} + \hat{V}^{\mathrm{psp},(\beta)}_{\mathbf{k},\mathbf{q}} + \hat{V}^{\mathrm{H0},(\beta)}_{\mathbf{q}} + \hat{V}^{\mathrm{XC0},(\beta)}_{\mathbf{q}} + \hat{V}^{\mathrm{geom},(\beta)}_{\mathbf{q}}. \tag{4.6}$$

In Eq. 4.6, the kinetic term is originating from the linear part of the metric tensor (which coincides with the strain tensor) and it is

$$\hat{T}^{(\beta)}_{\mathbf{k},\mathbf{q}} = -\frac{i}{2}\left[(\hat{p}_{\mathbf{k}\beta} + q_\beta)\,\mathbf{q}\cdot\hat{\mathbf{p}}_{\mathbf{k}} + (\hat{\mathbf{p}}_{\mathbf{k}} + \mathbf{q})\cdot\mathbf{q}\,\hat{p}_{\mathbf{k}\beta}\right], \tag{4.7}$$

where $\hat{p}_{\mathbf{k}\beta} = -i\partial/\partial\xi_\beta + k_\beta$ is the canonical momentum operator in curvilinear space. For notational purposes we shall write the remainder of the contributions as

matrix elements on two plane waves, e.g.,

$$W^{(\beta)}_{\mathbf{k},\mathbf{q}}(\mathbf{G},\mathbf{G}') = \langle \mathbf{G}+\mathbf{k}+\mathbf{q}|\hat{W}^{(\beta)}_{\mathbf{k},\mathbf{q}}|\mathbf{G}'+\mathbf{k}\rangle \tag{4.8}$$

for an arbitrary operator $\hat{W}$.

Regarding the pseudopotential term, it is the sum of a local and a separable contribution, as shown in the ground state case by Eq. 2.13; the corrispondent first order metric terms are (see Appendix C)

$$\begin{aligned} V^{\mathrm{loc},(\beta)}_{\mathbf{q}}(\mathbf{G}) =& iG_\beta \frac{1}{\Omega}\sum_\kappa e^{-i\mathbf{G}\cdot\boldsymbol{\tau}_\kappa} v^{\mathrm{loc}}_\kappa(\mathbf{G}) \\ & - i(G_\beta+q_\beta)\frac{1}{\Omega}\sum_\kappa e^{-i\mathbf{G}\cdot\boldsymbol{\tau}_\kappa} v^{\mathrm{loc}}_\kappa(\mathbf{G}+\mathbf{q}) \end{aligned} \tag{4.9}$$

$$\begin{aligned} V^{\mathrm{sep},(\beta)}_{\mathbf{k},\mathbf{q}}(\mathbf{G},\mathbf{G}') = \frac{1}{\Omega}\sum_{\mu\kappa} e_{\mu\kappa} e^{-i(\mathbf{G}-\mathbf{G}')\cdot\boldsymbol{\tau}_\kappa} \Big\{ & i(G_\beta+k_\beta+\frac{q_\beta}{2})\zeta_{\mu\kappa}(\mathbf{G}+\mathbf{k})\zeta^*_{\mu\kappa}(\mathbf{G}'+\mathbf{k}) \\ & - i(G_\beta-G'_\beta+q_\beta)\zeta_{\mu\kappa}(\mathbf{G}+\mathbf{k}+\mathbf{q})\zeta^*_{\mu\kappa}(\mathbf{G}'+\mathbf{k}) \\ & - i(G'_\beta+k_\beta+\frac{q_\beta}{2})\zeta_{\mu\kappa}(\mathbf{G}+\mathbf{k}+\mathbf{q})\zeta^*_{\mu\kappa}(\mathbf{G}'+\mathbf{k}+\mathbf{q})\Big\}, \end{aligned} \tag{4.10}$$

where $\zeta_{\mu\kappa}(\mathbf{G}+\mathbf{k})$ indicates the Fourier components of the KB projectors.

The two terms

$$V^{\mathrm{H0},(\beta)}_{\mathbf{q}}(\mathbf{G}) = 4\pi i\left(-\frac{G_\beta+q_\beta}{|\mathbf{G}+\mathbf{q}|^2}+\frac{G_\beta}{G^2}\right)n^{(0)}(\mathbf{G}), \tag{4.11}$$

$$V^{\mathrm{XC0},(\beta)}_{\mathbf{q}}(\mathbf{G}) = -iq_\beta V^{\mathrm{xc},(0)}(\mathbf{G}) \tag{4.12}$$

are the "geometric" (i.e., only depending on the unperturbed quantity, $n^{(0)}$) contributions to the Hartree (H) and exchange-correlation (XC) potentials, respectively. Finally,

$$V^{\mathrm{geom},(\beta)}_{\mathbf{q}} = -\frac{i}{4}q_\beta\, q^2 \tag{4.13}$$

is an additional geometric potential originating from the change of coordinates, which we introduce here for completeness (this structureless potential is irrelevant for either the uniform strain or the strain-gradient response, as it is of third order in $\mathbf{q}$).

Based on the above results, it is now easy to demonstrate the two following points. First, the external perturbation $\hat{H}^{(\beta)}_{\mathbf{k},\mathbf{q}}$ identically vanishes in the limit $\mathbf{q}=0$. This is a consequence of the fact that, in the co-moving frame, the Hamiltonian is

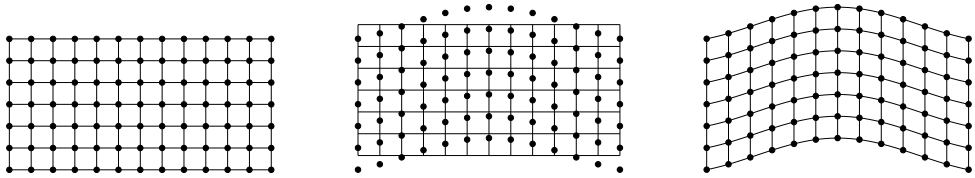

FIGURE 4.1: Illustration of the coordinate transformation to the co-moving frame. (a) Unperturbed crystal lattice; black circles represent the atomic sites, horizontal and vertical lines represent the coordinate system. (b) Transverse acoustic phonon in the laboratory frame. (c) The same phonon in the curvilinear frame; note that the atoms do not move in this coordinate system – the mechanical deformation is described via the metric.

invariant under rigid translations. Second, the first $\mathbf{q}$-gradient of the above expressions recovers the treatment by Hamann *et al.* [33] for the uniform strain:

$$i\mathcal{H}^{(\alpha\beta)}_{\mathbf{k}} = \left.\frac{\partial \mathcal{H}^{(\beta)}_{\mathbf{k},\mathbf{q}}}{\partial q_\alpha}\right|_{\mathbf{q}=0}, \tag{4.14}$$

which is symmetric under $\beta\gamma$ exchange. We have, therefore, achieved the desired generalization of the metric tensor formalism of Ref. [33] to a monochromatic displacement wave of arbitrary $\mathbf{q}$.

In conclusion, the explicit knowledge of the Hamiltonian $\hat{\mathcal{H}}^{(\beta)}_{\mathbf{k},\mathbf{q}}$ allows to calculate the associated first order-response functions, $|u^{(\beta)}_{n\mathbf{k},\mathbf{q}}\rangle$. By definition of metric perturbation, the first-order response are zero for $\mathbf{q} = 0$. Then when we will calculate the static flexoelectric coefficient, $\overline{\mu}'_{\alpha\beta,\gamma\delta}$, as the second q-derivative of the static polarization, Eq. 3.50, the current density operator for non-local pseuopotential, Eq. 2.63, is only needed up to the first order in q.

4.2 Relation between acoustic phonon in curvilinear and Cartesian frame

In this section we establish the explicit link between the metric perturbation previously derived, defined in the co-moving frame, and the familiar phonon perturbation, defined in the laboratory frame (and derived in Sec. 2.2.1). In particular, we show that the corresponding response functions ("metric" versus "phonon") differ

by a geometric piece that depends only on ground-state quantities. The analytical results of the present paragraph will prove to be important, on one side for finding the connection between the current density response in the Cartesian frame, Eq. 2.67, and its analogous in curvilinear coordinates, Eq. 3.50, and on the other side for testing the numerical implementation of the metric perturbation, as shown below.

The first-order external potential for a phonon perturbation consists of a local potential plus a separable contribution (see Sec. 2.1.2),

$$V^{ext\,\tau_{\kappa\beta}}_{\mathbf{k},\mathbf{q}}(\mathbf{G},\mathbf{G}') = V^{\mathrm{loc},\tau_{\kappa\beta}}_{\mathbf{q}}(\mathbf{G}-\mathbf{G}') + V^{\mathrm{sep},\tau_{\kappa\beta}}_{\mathbf{k},\mathbf{q}}(\mathbf{G},\mathbf{G}'), \tag{4.15}$$

where the two terms can be written as

$$V^{\mathrm{loc},\tau_{\kappa\beta}}_{\mathbf{q}}(\mathbf{G}) = -i(G_\beta+q_\beta)\frac{1}{\Omega}e^{-i\mathbf{G}\cdot\boldsymbol{\tau}_\kappa}\,v^{\mathrm{loc}}_\kappa(\mathbf{G}+\mathbf{q}), \tag{4.16}$$

$$V^{\mathrm{sep},\tau_{\kappa\beta}}_{\mathbf{k},\mathbf{q}}(\mathbf{G},\mathbf{G}') = -i(G_\beta+q_\beta-G'_\beta)\frac{1}{\Omega}\sum_\mu e^{-i(\mathbf{G}-\mathbf{G}')\cdot\boldsymbol{\tau}_\kappa}\,e_{\mu\kappa}\zeta_{\mu\kappa}(\mathbf{k}+\mathbf{q}+\mathbf{G})\zeta^*_{\mu\kappa}(\mathbf{k}+\mathbf{G}'), \tag{4.17}$$

Note that the first order potential in Eq. 4.15 are related to the perturbation defined in Eq. 2.38, which carry an extra phase factor, $e^{i\mathbf{q}\cdot\boldsymbol{\tau}_\kappa}$, respect to the standard choice, Eq. 2.30. Therefore Eq.s 4.16 and 4.17 have a slightly different structure factor compared to Eq.s. 2.34.

In the laboratory frame, an acoustic phonon perturbation can be readily constructed as a sublattice sum of the above,

$$V^{ext\,u_\beta}_{\mathbf{k},\mathbf{q}}(\mathbf{G},\mathbf{G}') = \sum_\kappa V^{ext\,\tau_{\kappa\beta}}_{\mathbf{k},\mathbf{q}}(\mathbf{G},\mathbf{G}'). \tag{4.18}$$

Here and in the following we use the symbol u_β to indicate a laboratory-frame acoustic phonon perturbation, not to be confused with the corresponding metric perturbation labeled by (β). The corresponding first-order wavefunctions satisfy the Sternheimer equation (similar to Eq. 2.32):

$$\left(\hat{\mathcal{H}}^{(0)}_{\mathbf{k}+\mathbf{q}} + a\hat{P}_{\mathbf{k}+\mathbf{q}} - \epsilon^{(0)}_{m\mathbf{k}}\right)|u^{u_\beta}_{m\mathbf{k},\mathbf{q}}\rangle = -\hat{Q}_{\mathbf{k}+\mathbf{q}}\hat{V}^{u_\beta}_{\mathbf{k},\mathbf{q}}|u^{(0)}_{m\mathbf{k}}\rangle, \tag{4.19}$$

where $\hat{V}^{u_\beta}_{\mathbf{k},\mathbf{q}}$ is the first order potential respect to an acoustic wave.

Now, to see the relationship between the laboratory and curvilinear frame pictures, it is convenient to take one step back, and consider the first-order Hamiltonians in the original Hilbert space, i.e. without factoring out the incommensurate phases that belong either to the Bloch orbitals or to the first-order Hamiltonian. We

shall postulate (and prove *a posteriori* that it is consistent with the results derived so far) the relationship

$$\hat{V}^{u_\beta}(\mathbf{q}) = \hat{\mathcal{H}}^{(\beta)}(\mathbf{q}) + i\left[\hat{\mathcal{H}}^{(0)}, \frac{1}{2}\left(e^{i\mathbf{q}\cdot\mathbf{r}}\hat{p}_\beta + \hat{p}_\beta e^{i\mathbf{q}\cdot\mathbf{r}}\right)\right]. \tag{4.20}$$

After reverting to the cell-periodic notation, the relation between laboratory-frame and metricresponses in Eq. 4.20 becomes

$$\hat{V}^{u_\beta}_{\mathbf{k},\mathbf{q}} = \hat{\mathcal{H}}^{(\beta)}_{\mathbf{k},\mathbf{q}} + i\hat{\mathcal{H}}^{(0)}_{\mathbf{k}+\mathbf{q}}\left(\hat{p}_{\mathbf{k}\beta} + \frac{q_\beta}{2}\right) - i\left(\hat{p}_{\mathbf{k}\beta} + \frac{q_\beta}{2}\right)\hat{\mathcal{H}}^{(0)}_{\mathbf{k}}. \tag{4.21}$$

The correctness of this result can be verified by comparing the explicit formulas for the perturbed Hamiltonians, derived in the previous paragraph, piece by piece. In particular, the second and the third terms on the rhs of Eq. 4.21 precisely cancel the kinetic and geometric contributions in $\hat{\mathcal{H}}^{(\beta)}_{\mathbf{k},\mathbf{q}}$, and they also account for the difference between the pseudopotential, Hartree, and XC terms in $\hat{\mathcal{H}}^{(\beta)}_{\mathbf{k},\mathbf{q}}$ and $\hat{V}^{u_\beta}_{\mathbf{k},\mathbf{q}}$.

If Eq. 4.21 is plugged into Eq. 4.19, one obtain an analogous Sternheimer equation with $\hat{\mathcal{H}}^{(\beta)}_{\mathbf{k},\mathbf{q}}$ replacing $\hat{V}^{u_\beta}_{\mathbf{k},\mathbf{q}}$, and with the laboratory-frame first-order wavefunctions related to the metric ones by

$$|u^{u_\beta}_{m\mathbf{k},\mathbf{q}}\rangle = |u^{(\beta)}_{m\mathbf{k},\mathbf{q}}\rangle + |\Delta u^{\beta}_{m\mathbf{k},\mathbf{q}}\rangle, \tag{4.22}$$

where $|\Delta u^{\beta}_{m\mathbf{k}}\rangle$ is a purely geometric contribution, i.e. it is defined in terms of the ground-state orbitals only,

$$|\Delta u^{\beta}_{m\mathbf{k},\mathbf{q}}\rangle \quad = \quad -i\hat{Q}_{\mathbf{k}+\mathbf{q}}\left(\hat{p}_{\mathbf{k}\beta} + \frac{q_\beta}{2}\right)|u^{(0)}_{m\mathbf{k}}\rangle. \tag{4.23}$$

This constitutes the main result of this Section.

To illustrate its physical meaning it is useful, first of all, to calculate the contribution of $|\Delta u^{\beta}_{m\mathbf{k},\mathbf{q}}\rangle$ to the first-order electron density, and check whether it satisfies the expected relations between its laboratory-frame and curvilinear-frame representations. By combining the definition of the density response to a generic perturbation, Eq. 2.24, with the specific Eq. 4.22, we get

$$n^{u_\beta}_{\mathbf{q}}(\mathbf{r}) = n^{(\beta)}_{\mathbf{q}}(\mathbf{r}) + \Delta n^{\beta}_{\mathbf{q}}(\mathbf{r}), \tag{4.24}$$

where $\Delta n^{\beta}_{\mathbf{q}}(\mathbf{r})$ is, again, a purely geometric object. One can arrive at an explicit formula for $\Delta n^{\beta}_{\mathbf{q}}(\mathbf{r})$ after observing that $\hat{Q}_{\mathbf{k}+\mathbf{q}} = 1 - \hat{P}_{\mathbf{k}+\mathbf{q}}$, where $\hat{P}_{\mathbf{k}+\mathbf{q}}$ is the projector on the valence band states; this leads to two separate contributions to $\Delta n^{\beta}_{\mathbf{q}}(\mathbf{r})$. The

part that contains the band projector $\hat{P}_{\mathbf{k}+\mathbf{q}}$ vanishes identically, which can be seen in the following way. Any physical scalar field must be real, which implies

$$n^{(1)}_{-\mathbf{q}}(\mathbf{r}) = n^{(1)*}_{\mathbf{q}}(\mathbf{r}). \tag{4.25}$$

Thus, the contribution of $\hat{P}_{\mathbf{k}+\mathbf{q}}$ to $\Delta n^{\beta}_{\mathbf{q}}(\mathbf{r})$ can be written as

$$\begin{aligned}&\sum_{mj} i\langle u^{(0)}_{m\mathbf{k}}|\mathbf{r}\rangle\langle\mathbf{r}|u^{(0)}_{j\mathbf{k}+\mathbf{q}}\rangle\langle u^{(0)}_{j\mathbf{k}+\mathbf{q}}|\left(\hat{p}_{\mathbf{k}\beta}+\frac{q_\beta}{2}\right)|u^{(0)}_{m\mathbf{k}}\rangle \\ &-\sum_{mj} i\langle u^{(0)}_{j\mathbf{k}-\mathbf{q}}|\mathbf{r}\rangle\langle\mathbf{r}|u^{(0)}_{m\mathbf{k}}\rangle\langle u^{(0)}_{m\mathbf{k}}|\left(\hat{p}_{\mathbf{k}\beta}-\frac{q_\beta}{2}\right)|u^{(0)}_{j\mathbf{k}-\mathbf{q}}\rangle.\end{aligned} \tag{4.26}$$

After operating a translation in $\mathbf{k}$-space on the second line (this is irrelevant, as the expression needs to be integrated over the whole Brillouin zone), the result manifestly vanishes.

Eq. 4.23 is left with just the contribution of the identity operator, which can be written as

$$\Delta n^{\beta}_{\mathbf{q}}(\mathbf{r}) = -\frac{\partial n^{(0)}(\mathbf{r})}{\partial r_\beta} - iq_\beta n^{(0)}(\mathbf{r}), \tag{4.27}$$

In order to illustrate the meaning of Eq. 4.20 and 4.27, one can consider a uniform translation of a crystal. Then for the laboratory-frame perturbation we have

$$\hat{V}^{u_\beta}_{\mathbf{k},\mathbf{q}=0} = i\left[\hat{H}^{(0)}_{\mathbf{k}}, \hat{p}_{\mathbf{k}\beta}\right], \tag{4.28}$$

and therefore Eq. 4.20 yields immediately

$$\hat{\mathcal{H}}^{(\beta)}_{\mathbf{k},\mathbf{q}=0} = 0, \tag{4.29}$$

as one should expect since, as we said early, a uniform translation of the crystal has no effect in its own co-moving reference frame. The same is true for the charge density relation where a uniform translation in the Cartesian frame gives $n^{u^\beta}_{\mathbf{q}=0}(\mathbf{r}) = -\frac{\partial n^{(0)}(\mathbf{r})}{\partial r_\beta}$, and therefore $n^{(\beta)}_{\mathbf{q}=0}(\mathbf{r}) = 0$.

In other words, Eq. 4.20 and 4.27 corroborates the interpretation that the "metric" wave effects do not induce atomic displacements but are expressed as a local modification of the metric of space. From this perspective the geometric contribution, $|\Delta u^{\beta}_{m\mathbf{k},\mathbf{q}}\rangle$ is essential for ensuring that the first-order density response complies with the established transformation laws.

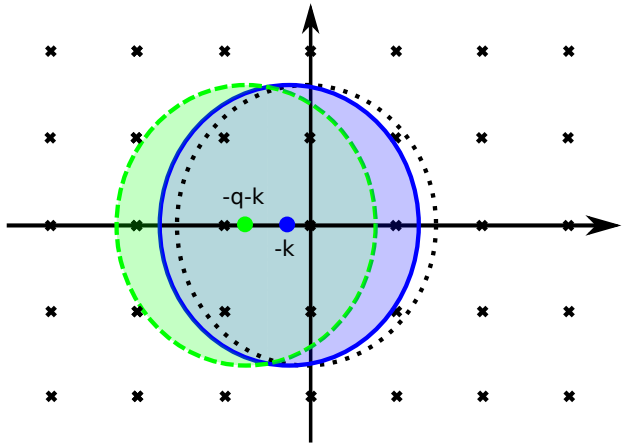

FIGURE 4.2: Representation of the Fourier space in 2D. The small black cross are the G-vectors, the black dot circle identifies the cut-off sphere centered in Γ, the blue continue circle identifies nonzero Fourier coefficients of $|u_{\mathbf{k}}>$, while the dashed green circle identifies the Fourier coefficients of $|u_{\mathbf{k},\mathbf{q}}>$.

4.3 Implementation Considerations

The formulas derived in the previous section are formal, but when implementing them we need to introduce approximations in order to make the calculations tractable. In particular, we make a set of choices concerning the discrete sampling of the Brillouin zone (BZ) with a finite mesh, and the plane-wave energy cutoff used in the wave-function expansion. It is therefore important to clarify which of the above relations remain exact in principle, once such a set of choices has been made, and which should be expected to show discrepancies (of course, these will diminish as more highly converged choices are made).

Our main focus will be on Eq. 4.27, describing the difference between the electron-density response to a phonon perturbation in the laboratory frame, already available within the existing DFPT implementations, and the new metric response introduced in this work.

First of all note that, in order to obtain Eq. 4.27, we have used the fact that the expression in Eq. 4.26 vanishes; this, in turn, relies on the fact that it must be integrated over the whole Brillouin zone. If the BZ is sampled by a discrete number of **k** points, then Eq. 4.26 is only approximately satisfied; in fact, one can see that it holds exactly only if the set of **k**-points is invariant under a translation by **q**, i.e., **q** is commensurate with the **k**-points.

Still, the commensuration between **q** and the **k**-mesh does not automatically

guarantee that Eq. 4.24 is exact. To see this, one can rewrite the geometric contribution, Eq. 4.27, as

$$\begin{aligned}\Delta n^{\beta}_{\mathbf{q}}(\mathbf{r}) &= -\frac{4i}{N_{\mathbf{k}}}\sum_{m\mathbf{k}}\langle u^0_{m\mathbf{k}}|\mathbf{r}\rangle\langle\mathbf{r}|\hat{Q}_{\mathbf{k}+\mathbf{q}}(\hat{p}_{\mathbf{k}\beta}+\frac{q_\beta}{2})|u^0_{m\mathbf{k}}\rangle \\ &= -\frac{4i}{N_{\mathbf{k}}}\sum_{m\mathbf{k}}\langle u^0_{m\mathbf{k}}|\mathbf{r}\rangle\langle\mathbf{r}|(\hat{p}_{\mathbf{k}\beta}+\frac{q_\beta}{2})|u^0_{m\mathbf{k}}\rangle\end{aligned} \tag{4.30}$$

where $N_{\mathbf{k}}$ is the number of $\mathbf{k}$-points (a uniform mesh is assumed), and the second equality relies on the assumed commensuration between $\mathbf{q}$ and the mesh (see above discussion). The previous equation only reduces to Eq. 4.27 in the case of an infinite basis set. However, in practice, a finite basis set is always used, which means that plane waves with a kinetic energy that is larger than E_{cut} are discarded from the calculation. Crucially, the kinetic energy of a plane wave is calculated as $|\mathbf{G}+\mathbf{k}|^2/2$, which implies that different $\mathbf{k}$ points are characterized by different cutoff spheres in reciprocal space, and hence by different basis sets. For example, the wavefunction $u^0_{\mathbf{k}}(\mathbf{r})$ has non-zero coefficients only inside a cutoff sphere centred in $-\mathbf{k}$ (blue sphere in Fig 4.2), while the sphere of both the phonon and metric response functions $u^{(1)}_{\mathbf{k}+\mathbf{q}}(\mathbf{r})$ is centered in $-(\mathbf{k}+\mathbf{q})$ (green sphere in Fig 4.2). Therefore, in a DFPT calculation the first order density response to both the phonon and metric perturbation, $n^{(1)}_{\mathbf{q}}(\mathbf{r}) = 4/N_{\mathbf{k}}\sum_{m\mathbf{k}}\langle u_{m\mathbf{k}}|\mathbf{r}\rangle\langle\mathbf{r}|u^{(1)}_{m\mathbf{k},\mathbf{q}}\rangle$, has non-zero Fourier coefficients only inside the intersection between the two sphere.

It follows that the computed difference between n^{β} and n^{u_β} shall be equal to

$$\Delta\tilde{n}^{(\beta)}_{\mathbf{q}}(\mathbf{r}) = -\frac{4i}{N_{\mathbf{k}}}\sum_{m\mathbf{k}}\langle u^0_{m\mathbf{k}}|\mathbf{r}\rangle\langle\mathbf{r}|(\hat{p}_{\mathbf{k},\beta}+\frac{q}{2})|\tilde{u}^0_{m\mathbf{k}}\rangle \tag{4.31}$$

where $\tilde{u}^{(0)}_{m\mathbf{k}}(\mathbf{r})$ is the same as $u^{(0)}_{m\mathbf{k}}(\mathbf{r})$ in Eq. 4.30 except that it has nonzero Fourier components only in the intersection between the green and blue circles of Fig. 4.2, while $u^{(0)}_{m\mathbf{k}}(\mathbf{r})$ is defined inside the whole blue solid circle. Since the first-order wave functions are obtained through a self-consistent process, this error will propagate to the potentials and back to the density; thus, at the end of the calculation even the "revised" relationship 4.31 will not be exactly fulfilled. In any case, we can expect that the error will be roughly linear in $|\mathbf{q}|$, and should rapidly vanish upon increasing the plane-wave cutoff; we shall see that both expectations are nicely fulfilled in ourtests. As we shall show shortly, this discrepancy between the phonon and metric approach results in a faster numerical convergence of the latter with respect to plane-wave cutoff and k-point sampling.

4.4 Numerical tests

To test our implementation of the metric perturbation, we compare it to the response functions that are already present in public available DFPT codes: the phonon perturbation [28] and the uniform strain perturbation [33]. In particular, we perform three different tests:

1- We benchmark the electron density response by numerically verifying Eq. 4.24, where the geometric contribution, $\Delta n^{\beta}_{\mathbf{q}}(\mathbf{r})$, is defined in terms of the ground state wavefunctions as in Eq. 4.27.

In order to construct the response to an acoustic phonon (in the Cartesian frame) we use $n^{(u_\beta)} = \sum_\kappa n^{(\tau_{\kappa\beta})}$, where $n^{(\tau_{\kappa\beta})}$ is the response to an individual atomic displacements defined in Eq. 2.39.

2- We compare the electron density response of a uniform strain perturbation to the electron density response of a metric perturbation at first order in $\mathbf{q}$. We have already explained how the metric wave can be consider a generalization of the uniform strain perturbation. In the same way, their corresponding density response are related by

$$in^{(\alpha\beta)}(\mathbf{r}) = \left.\frac{n^{(\beta)}_{\mathbf{q}}(\mathbf{r})}{\partial q_\alpha}\right|_{\mathbf{q}=0}, \tag{4.32}$$

where the r.h.s. is the first derivative of the microscopic metric perturbation response, $n^{(\beta)}_{\mathbf{q}}(\mathbf{r})$, respect to q_α. Note that the first $\mathbf{q}$-derivative of the metric density is a pure imaginary function. In conclusion, testing Eq. 4.32 is particularly interesting in order to prove that indeed the metric perturbation can be regarded as the generalization of a uniform strain deformation.

3- We compare the octupolar response calculated via the phonon to that obtained via the metric perturbation. The octupolar tensor components can be extracted via the long-wave expansion of the macroscopic (i.e., cell-integrated) charge-density response

$$Q^{(3,\alpha\beta\gamma)}_{\delta} = \mathrm{Im}\int_{\mathrm{cell}} d^3r \left.\frac{\partial^3 n^{(\delta)}_{\mathbf{q}}(\mathbf{r})}{\partial q_\alpha \partial q_\beta \partial q_\gamma}\right|_{\mathbf{q}=0} \tag{4.33}$$

where δ indicates the atomic displacement direction, and remind that also the third q-derivative of the density response function is only imaginary. Clearly,

since the geometrical term Δn^β averages to zero, both the phonon and metric calculations should, in principle, yield the same values of $Q_\delta^{(3,\alpha\beta\gamma)}$. The q-derivative can be performed by fitting the cell-integrated density as a function of $\mathbf{q}$ in a vicinity of $\mathbf{q} = 0$, as described in Ref. [74]. Directly testing the octupoles is important, since they are directly related to the longitudinal clamped-ion flexoelectric tensor by Eq. 3.40.

Note that, whenever a 3D scalar field is involved (first and second tests), we shall use the "distance"

$$d(f,g) = \frac{1}{\Omega}\int_{\text{cell}} d^3r\,|f(\mathbf{r}) - g(\mathbf{r})|, \tag{4.34}$$

to gauge their overall difference, where functions f and g identify the left- and right-hand sides of the given relation that is to be verified.

4.4.1 Computational setup

We have used two types of systems for our benchmark tests in the following sections: isolated noble gas atoms in large boxes, and cubic bulk solids. Regarding the isolated atoms, we have tested three different noble gases, He, Ne and Kr. As for the cubic solids, we have used crystalline Si in the diamond structure, and the cubic perovskite phase of $SrTiO_3$.

The calculations are performed in the framework of density-functional theory, using the local-density approximation (we have employed the Perdew-Wang 92 parametrization [58] of the exchange and correlation). The core-valence interactions are described by Troullier-Martins [83] norm-conserving pseudopotentials, which was generated via the fhi98PP [22] code with the following electronic configurations: He=$1s^2$; Ne=$2s^22p^6$; Kr=$4s^24p^6$; Si=$3s^23p^2$; Sr=$4s^24p^5s^2$; Ti=$3s^23p^63d^24s^2$; O=$2s^22p^4$. Note that the He pseudopotetial only contains a local part.

The noble gas atoms have been simulated in cubic boxes large enough to avoid interaction between the replicas. The size of such box in the test are 5 Bohr for He, 7 Bohr for Ne, and 14 Bohr for Kr, with (unless specified), Monkhorst-Pack (MP) k-meshes [54] of 8×8×8 for He and Ne, and 4×4×4 for Kr. For the calculation of flexoelectric constants in Sec. 4.5, 14 Bohr boxes were used for all atoms, with a 4×4×4 k-mesh and a plane wave cutoff of 120 Ha.

The relaxed cubic lattice parameters obtained for Si and $SrTiO_3$ are 10.102 and 7.267 Bohr respectively. Calculations are performed under short-circuit electrostatic boundary conditions (see Refs. [77] and [19] for details). For Si and $SrTiO_3$, MP k-meshes from 4×4×4 to 16×16×16 and plane wave cutoffs from 20 to 100 Ha were

tested to explore the convergence properties of the metric and phonon implementations. For the calculations of flexoelectric coefficients, a $12\times12\times12$ k-mesh and 80 Ha plane wave cutoff were used.

Note that short circuit electrostatic boundary conditions (EBC) have been used throughout this work. Indeed, here we are mainly interested in long-wave expansions of the polarization (or charge-density) response; to do this, it is essential to deal with an analytic function, and the short circuit EBC precisely remove the non-analyticity generated by the presence of the macroscopic electric field [77]. This, however, differs from the physical electrostatic conditions ("mixed" EBC) that characterize the phonon response at nonzero $\mathbf{q}$ [36]. (The difference between the two cases only concern the longitudinal components of the polarization, since mixed EBC impose zero longitudinal displacement field.) Thus, if the metric perturbation is to be employed for the realistic simulation of a finite-$\mathbf{q}$ acoustic phonon, such longitudinal fields must be incorporated in the calculation [78]. For a metric wave the short circuit EBC are obtained by simply removing the $\mathbf{G} = 0$ component from the self-consistent part of the first-order Hartree potential response, $\hat{V}^{(\beta)}_{\mathbf{q}}$; by plugging this contribution back into the first-order Hamiltonian, we readily recover the correct electrostatics. Thus, switching from short-circuit to standard electrical boundary conditions is even simpler in the metric case than in the standard phonon case.

4.4.2 Charge density response: Phonon vs. metric

First, we check the validity of Eq. 4.24, which connects the metric and phonon charge density response functions via a geometric term. To make this test quantitative, we have taken advantage of the distance function defined in Eq. 4.34, with $f(\mathbf{r}) = n^{u^\beta}_{\mathbf{q}}(\mathbf{r})$ and $g(\mathbf{r}) = n^{(\beta)}_{\mathbf{q}}(\mathbf{r}) + \Delta n^{\beta}_{\mathbf{q}}(\mathbf{r})$. [We construct $\Delta n^{\beta}_{\mathbf{q}}(\mathbf{r})$ in terms of the ground-state density, following Eq. 4.27.] Tests are conducted on He, Ne and Kr atoms. Due to periodic boundary condition these systems can be regarded as crystals of isolated atoms, intended as a computational analog to the toy model of Ref. [74], and discussed further in Sec. 4.5.1. The perturbations considered here are longitudinal, and they propagate along one of the three equivalent Cartesian axis. In Fig. 4.3 we report the values of $d(f,g)$ as a function of the wavevector amplitude, $|\mathbf{q}|$, for different energy cutoffs.

The first interesting observation is the almost perfect linear trend shown by the function $d(f,g)$. As we anticipated in Section 4.3, this is a direct consequence of using a finite plane-wave basis set: the larger the wavevector, the larger the shift of

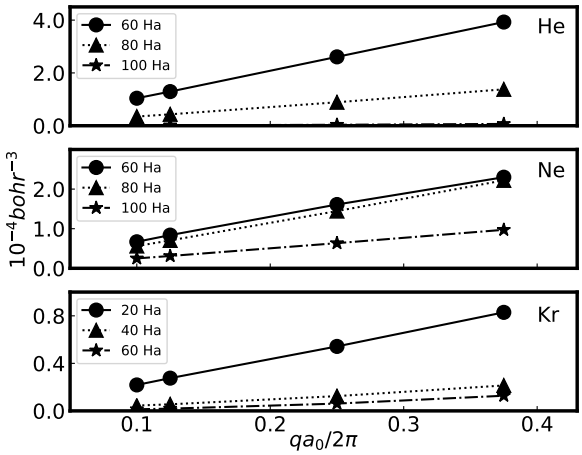

FIGURE 4.3: Plot of $d(n^{u^\beta}_{\mathbf{q}}(\mathbf{r}), n^{(\beta)}_{\mathbf{q}}(\mathbf{r}) + \Delta n^{\beta}_{\mathbf{q}}(\mathbf{r}))$ [cf., Eq. (4.34)] as function of the wave vector $\mathbf{q}$ (reduced coordinates), for different the cutoff. All the results refer to longitudinal perturbations. From the top to the the bottom: He, Ne and Kr.

the cutoff sphere, and hence one expects a discrepancy that is roughly proportional to $|\mathbf{q}|$.

Next, one can clearly appreciate, by comparing the slopes of the curves shown in Fig. 4.3, that the discrepancy between the phonon and metric results decreases as we increase the plane-wave cutoff. This happens because the discrepancy depends on the magnitude of the plane-wave coefficient at the boundary of the cutoff sphere (i.e., those falling outside the intersection of the two circles in Fig. 4.2); this is expected to decrease quickly with the cutoff, consistent with our results. Also, we see that the discrepancy between the metric and phonon charge-density responses is an order of magnitude smaller for Kr than He and Ne; This is a direct consequence of the much softer pseudopotential associated to Kr as compared to Ne and He.

As a final comment we look at the calculated values corresponding to wavevectors $\mathbf{q}$ that are not necessarily commensurate with the $\mathbf{k}$-mesh. (For example we have used an $8\times8\times8$ MP $\mathbf{k}$-mesh for He and Ne systems, so the point $q = 0.1$ doesn't match the $\mathbf{k}$-mesh.) The perfect linear trend of the distance function for all $\mathbf{q}$-values, irrespective of the exact or inexact cancellation in Eq. 4.26 (see discussion in Sec. 4.3) is a clear proof that the $\mathbf{k}$-mesh is dense enough, so that the finiteness of the plane-wave cutoff is the main source of error in this test.

We stress that the discrepancies that we discussed above are perfectly in line with the expected trends, and thus confirm the correctness of the implementation.

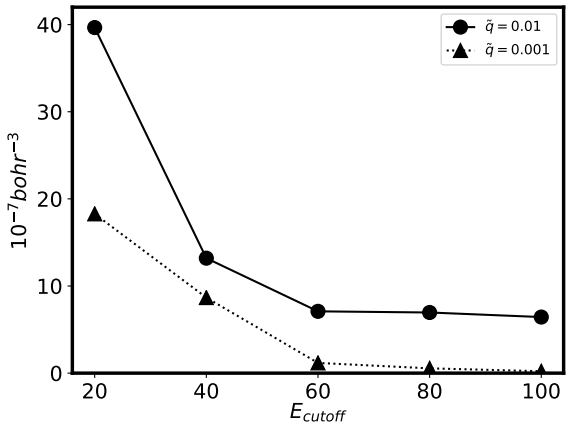

FIGURE 4.4: Cell integrated difference, $d(-in_{\alpha}^{1,\beta}(\mathbf{r}), n_{\alpha\beta}^{strain}(\mathbf{r}))$, between the first order term of the long wave expansion applied to the metric response density and the uniform strain response, calculated as in Ref. [33], for an He atom in a box undergoing a longitudinal mechanical perturbation. The two curves refer to two different values of the finite difference increment used for getting $n_{\alpha}^{1,\beta}(\mathbf{r})$.

4.4.3 Charge density response: Strain vs. metric

A second test of the metric implementation is based on its relationship with the response to a uniform strain. Indeed, the first derivative respect to the wavevector $\mathbf{q}$ of the metric perturbation should coincide with the strain perturbation of Hamann *et al.* [33], which is already implemented in the official release of the ABINIT code [see Eq. 4.14]. To prove this point, here we use the distance function of Eq. 4.34 to compare the charge-density response functions $f(\mathbf{r}) = -i\partial n_{\mathbf{q}}^{\beta}(\mathbf{r})/\partial q_{\alpha}$ and $g(\mathbf{r}) = n^{(\alpha\beta)}(\mathbf{r})$, which should coincide according to Eq. 4.32. The derivative respect to $\mathbf{q}$ of the metric response is performed by finite differences, and using two different spacing values: $\Delta q = \frac{2\pi}{a_0}\{0.01; 0.001\}$, where a_0 is the lattice parameter of the primitive cubic cell. In Fig. 4.4 I show $d(f, g)$ for the crystal of noninteracting He atoms as function of the energy cutoff, E_{cut}. As expected, the discrepancy rapidly goes to zero at larger values of E_{cut}, again proving the correctness of the implementation. We also note that, by reducing the spacing value for the numerical calculation of the $\mathbf{q}$-derivative, the consistency between the metric and strain results increases by one order of magnitude.

TABLE 4.1: $Q_L/6$ for He and Ne atoms, in e Bohr^2 (Short-circuit electrostatic boundary conditions).

CutOff	He, 5 Bohr		Ne, 7 Bohr		Kr, 14 Bohr	
(Ha)	metr	phon	metr	phon	metr	phon
40	0.4392	0.4660	1.7338	1.7928	5.8433	5.8382
60	0.4392	0.4322	1.8129	1.8208	5.8635	5.8618
80	0.4396	0.4418	1.8135	1.8111	5.8635	5.8635
100	0.4398	0.4398	1.8135	1.8135	5.8635	5.8635

TABLE 4.2: $Q_L/6$ along the [100] direction for Si and along the [110] direction for $SrTiO_3$. Values are in unit of e Bohr^2 (SC electrostatic boundary conditions). The two different columns for Si refer to two different **k**-mesh used: 12×12×12 and 16×16×16, respectively.

CutOff	Si(12)		Si(16)		STO_3	
(Ha)	metr	phon	metr	phon	metr	phon
20	478.379	478.456	478.391	478.409		
40	478.597	478.644	478.597	478.605		
60	478.601	478.653	478.601	478.612	111.793	111.658
80	478.601	478.653			111.662	111.666
100	478.601	478.653			111.684	111.673

4.4.4 Octupoles

We now compare the longitudinal octupoles calculated either using the metric or the standard acoustic phonon perturbation.

In order to extract the dynamical octupoles from both $n_{\mathbf{q}}^{(\beta)}$ and $n_{\mathbf{q}}^{u_\beta}$ one has to perform the third derivatives respect to $\mathbf{q}$, Eq. 4.33. In practice they can be calculated by a fitting procedure of the cell-integrated electronic density response functions to monochromatic perturbations with different values of $\mathbf{q}$ around the Γ-point. In the specific case of the octupoles we only focus on the imaginary part, see Eq. 4.33.

For this test we have employed the three noble gas atoms (He, Ne, and Kr), Si in the diamond structure, and cubic $SrTiO_3$. The directions chosen to calculate the longitudinal octupole are [100] and [110] for Si and $SrTiO_3$, respectively, while the wavevector amplitudes that we use for the cubic fit are $q_i = \{0.01; 0.02; 0.03\}$ (in reduced units of $2\pi/a_0$). Note that, in the case of the phonon response, the electronic charge also has a non-zero linear term as a function of $\mathbf{q}$, whose slope gives the electronic contribution to the Born effective charge of the displaced sublattice. Such a linear term is not present in the metric response, as the atoms are not moving

in the curvilinear frame.

In Table 4.1 we report the values of $Q_L/6$ for the He, Ne and Kr atoms, while the corresponding values for bulk Si and $SrTiO_3$ are shown in Table 4.2. As expected, the agreement between the metric and the phonon results increases with increasing the plane wave cutoff; such an agreement becomes essentially perfect in the case of the isolated noble-gas atoms at an energy cutoff of 100 Ha. The metric results converge much faster as a function of E_{cut} than the phonon results. Moreover, the test between the silicon octupole calculated with a $12\times12\times12$ and a $16\times16\times16$ MP **k**-mesh shows that the metric calculation also converges much faster with respect to the number of **k**-points.

The relatively worse convergence behavior in the phonon case can be tracked down once again to the geometric term, $\Delta n^{\beta}_{\mathbf{q}}(\mathbf{r})$. Indeed, if Eq. 4.24 was exactly satisfied, the cell integral of $n^{\beta}_{\mathbf{q}}(\mathbf{r})$ would vanish identically, and would not contribute to the calculated octupolar moment. However, in practical calculations Eq. 4.24 is violated, as we have already commented in Section 4.4.2 and summarized by Fig. 4.2. The violations is bigger at lower-energy cutoffs or coarser k-point samplings, and it can introduce an additional, spurious $\mathcal{O}(\mathbf{q}^3)$ contribution to the macroscopic density response. Since $\Delta n^{\beta}_{\mathbf{q}}(\mathbf{r})$ is rather large, this can have a negative impact on the overall convergence. Thus, the numerical tests in Tab. 4.1 and 4.2 reveal a further (and formerly unexpected) advantage of the metric perturbation presented here, i.e., a significant economy in terms of computational resources compared with the standard phonon treatment.

4.5 FxE tensors from metric perturbation

Finally, here we calculate the bulk clamped-ion FxE coefficients using the wavefunctions response to the metric perturbation. Following the results of Sec. 2.2.4, the wavefuncition response to a metric perturbation is employed to calculate the curvilinear adiabatic functions, $|\delta u^{(\beta)}_{n\mathbf{k},\mathbf{q}}\rangle$, which allows to obtain the static polarization response, via Eq. 3.50. Then, the second **q**-derivative of $\overline{\mathbf{P}}^{stat}_{\alpha\beta}$ gives the clamped-ion flexoelectric tensor, $\overline{\mu}'_{\alpha\beta,\gamma\delta}$. As done for the previous results, these derivatives are taken numerically with $\Delta q = (2\pi/a_0)0.005$. Interestingly note that, since the metric response to a uniform translation is zero, $|u^{(\beta)}_{n,\mathbf{k},\mathbf{q}=0}\rangle = 0$, then the current density operator for non-local pseudopotential, Eq. 2.63, is only needed up to the first order in **q**.

In the following we will always compare our results to the values obtained with a Cartesian phonon perturbation, which have been conveniently corrected removing the extra contribution proportional to the diamagnetic tensor (see Sec. 3.3).

All the reported flexoelectric tensor components are in type-II form, and, since here we are dealing with cubic crystals, the flexoelectric tensor has only three independent components, which are indicated as the longitudinal (μ_{11}), transverse (μ_{12}), and shear (μ_{44}) flexoelectric coefficients henceforth (also remind that in cubic crystals the diamagnetic susceptibility is isotropic, $\chi^{\text{mag}}_{\gamma\lambda} = \delta_{\gamma\lambda}\chi^{\text{mag}}$).

4.5.1 Isolated spherical atoms

We start by considering the toy model of a material made of isolated (i.e., noninteracting), spherical charge densities. This isolated rigid charge (IRC) model was already studied in the context of flexoelectricity [74, 76, 79], since it has an analytic expression for the FxE tensor components in terms of the isotropic quadrupole moment of the ground-state charge distribution,

$$Q^{\text{NG}} = \int d^3r\, \rho_{GS}(\mathbf{r}) x^2. \tag{4.35}$$

Such schematic IRC model can be seen as a good approximation of a fictitious lattice of isolated noble gas (NG) atoms. Clearly a solid of this kind does not exist because there is no force keeping the atoms together; however it represents a good numerical test for the metric implementation.

On one side, since in a IRC model the atoms almost do not interact between each other, then it is possible to caclulate directly the induced current density and the related FxE tensor. They are

$$\begin{aligned} \overline{\mu}^{\text{NG}}_{11} &= \epsilon \frac{Q^{\text{NG}}}{2\Omega} \\ \overline{\mu}^{\text{NG}}_{44} &= \frac{Q^{\text{NG}}}{2\Omega}, \end{aligned} \tag{4.36}$$

where ϵ is the isotropic clamped-ion dielectric constant, $\epsilon_{ij} = \epsilon\delta_{ij}$ (the subscript "NG" remind that the results are valid for noble gases). The explicit presence of the dielectric constant in $\overline{\mu}^{\text{NG}}_{11}$ is taking into account the macroscopic electric field induced by longitudinal atomic displacements in mixed EBC. In practice this is small in the case of the IRC model [19].

The dynamical contribution is proportional to the magnetic susceptibility. This model is a perfect example of system that satisfies the requirements of the Langevin

	$\overline{\mu}'_{11}$		$\overline{\mu}'_{12}$			$\overline{\mu}'_{44}$ (10^{-3})		
	metr	phon	metr	phon	$\epsilon Q^{\mathrm{NG}}/2\Omega$	metr	phon	χ^{mag}
He	−0.479	−0.479	−0.479	−0.479	−0.479	0.0	−0.3	−0.464
Ne	−1.843	−1.844	−1.841	−1.842	−1.842	−0.7	−0.6	−1.655
Kr	−6.477	−6.470	−6.476	−6.476	−6.479	−0.3	−0.5	−5.921

TABLE 4.3: Clamped-ion flexoelectric coefficients calculated using the metric and phonon implementations, as well as the quadrupole moments of the ground-state charge density. All quantities are in units of pC/m.

theory of diamagnetism, which relates the magnetic susceptibility to the quadrupole moment of the spherical ground state charge

$$\chi^{\mathrm{mag}} = \frac{Q^{\mathrm{NG}}}{2\Omega}, \tag{4.37}$$

where again the dielectric constant is needed to correct the slight polarizability of the atoms.

Then, reminding the results in Eq. 3.60, one can immediately remove the dynamical contributions from the values in Eq. 4.36, and obtain the static FxE coefficients:

$$\begin{aligned} \overline{\mu}'^{,\mathrm{NG}}_{11} &= \overline{\mu}'^{,\mathrm{NG}}_{12} = \epsilon \frac{Q^{\mathrm{NG}}}{2\Omega} \\ \overline{\mu}'^{,\mathrm{NG}}_{44} &= 0. \end{aligned} \tag{4.38}$$

Note that these values were also obtained in Ref. [74], by consideration on the induced bulk flexoevoltage.

Table 4.3 gives the clamped-ion FxE coefficients calculated for noble gas atoms using the metric and phonon implementations; the latter have been obtained by removing the contribution proportional to the diamagnetic contribution. By comparing the $\overline{\mu}'^{,\mathrm{NG}}_{11}$, $\overline{\mu}'^{,\mathrm{NG}}_{12}$, and $\epsilon Q^{\mathrm{NG}}/2\Omega$ columns, one can see that Eq. 4.38 is perfectly satisfied for both the metric and phonon methods, as well as $\overline{\mu}'^{,\mathrm{NG}}_{44}$ vanishes. The main source of error is the numerical differentiation of the induced polarization, $\overline{\mathbf{P}}^{\mathbf{q},stat}_{\alpha\beta}$, with respect to $\mathbf{q}$. The results of Table 4.3 indicate that the metric implementation is an accurate method for calculating flexoelectric coefficients, with increased efficiency as discussed above.

	$\overline{\mu}'_{11}$		$\overline{\mu}'_{12}$		$\overline{\mu}'_{44}$	
	metr	phon	metr	phon	metr	phon
$SrTiO_3$	-0.885	-0.884	-0.826	-0.826	-0.082	-0.083
Si	-1.411	-1.410	-1.049	-1.050	-0.189	-0.190

TABLE 4.4: Flexoelectric constants for $SrTiO_3$ and Si calculated using the phonon and metric implementations (units are nC/m); their orbital magnetic susceptibilities, χ^{mag}, are respectively -8.3×10^{-3} and 10.2×10^{-3}nC/m.

4.5.2 Cubic materials

We will now focus on the bulk clamped-ion FxE coefficients for two prototypical materials: $SrTiO_3$ (in the high-temperature cubic phase) and Si. The second derivative respect to $\mathbf{q}$ of Eq. 2.67 gives the type-I FxE coefficients using the phonon response. As before, the phonon values are corrected with a contribution proportional to χ^{mag}, as prescribed by Eq. 3.60. We can see from Table 4.4 that the agreement between the metric and phonon implementations is excellent.

As observed in previous calculations of the clamped-ion FxE coefficients [19, 78], the following relation holds between the order of magnitude of the FxE tensor components: $\overline{\mu}'_{11} \simeq \overline{\mu}'_{12} \gg \overline{\mu}'_{44}$.

In spite of the small magnitude of χ^{mag}, these results are sufficiently converged to see clearly that the rotation-gradient correction is required for accurate agreement between the metric and phonon implementations. Indeed, if this correction is neglected, then one get $\overline{\mu}'_{12} = -0.810$ and $\overline{\mu}'_{44} = -0.091$ for $SrTiO_3$, and $\overline{\mu}'_{12} = -1.070$ and $\overline{\mu}'_{44} = -0.180$ for Si, which have clear discrepancies with the metric results in Table 4.4.

In Figs. 4.5 the convergence of the FxE coefficients of $SrTiO_3$ and Si is shown as a function of k-point mesh. It results that the metric implementation is significantly more rapid to converge than the phonon implementation (they have similar convergence behavior with respect to plane-wave cutoff). The slower convergence of the phonon approach may have several possible origins. First, there may be additional numerical errors associated with the separate calculation of χ^{mag} that is needed for the phonon implementation but not for the metric. Second, as mentioned in Ref. [19], the expansion of the nonlocal contribution to the current density operator in the case of the metric implementation can be truncated to a lower order in $\mathbf{q}$ than in the phonon case. Third, the two implementations differ with respect to the treatment of the local potential at $\mathbf{q} = 0$, as we shall briefly discuss hereafter.

It is well known that the "external potential" of a phonon perturbation diverges in the limit of $\mathbf{q} \to 0$. Such divergence is carried by the $\mathbf{G} = 0$ Fourier component

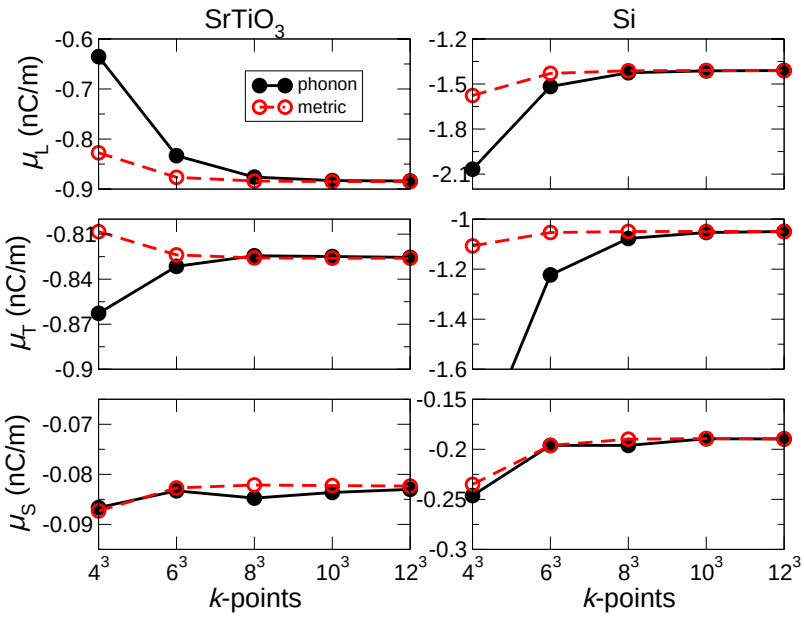

FIGURE 4.5: Convergence of the FxE coefficients of $SrTiO_3$ and Si with k-point mesh for the phonon and metric implementations.

of the local potential (sum over sublattices of Eq. 4.16),

$$\sum_\kappa V_{\mathbf{q}}^{\mathrm{loc},\tau_{\kappa\beta}}(\mathbf{G}=0) = -iq_\beta \frac{1}{\Omega}\sum_\kappa v_\kappa^{\mathrm{loc}}(\mathbf{q}), \tag{4.39}$$

where the contribution of each individual sublattice goes like

$$v_\kappa^{\mathrm{loc}}(\mathbf{q}) \sim 4\pi\frac{Z_\kappa}{q^2}. \tag{4.40}$$

(Recall that Z_κ is the total pseudopotential charge.) The local pseudopotential contribution to the metric perturbation, Eq. 4.9, is characterized by an analogous divergence, but the latter is exactly cancelled by an equal and opposite divergence in the geometric Hartree term, Eq. 4.11,

$$V_{\mathbf{q}}^{\mathrm{H0},(\beta)}(\mathbf{G}=0) = 4\pi i\frac{q_\beta}{q^2}n^{(0)}(\mathbf{G}=0) \tag{4.41}$$

[recall that $n^{(0)}(\mathbf{G}=0) = (1/\Omega)\sum_\kappa Z_\kappa$, as the cell must be overall charge-neutral]. Then $\hat{H}^{(\beta)}_{\mathbf{k},\mathbf{q}}$ remains finite (in fact, it vanishes) in the limit $\mathbf{q}\to 0$, and this might also help explain the superior numerical behavior of the metric perturbation in the

convergence tests.

In summary, these calculations have clearly demonstrated the superiority of the metric implementation for determining the clamped-ion FxE coefficients in terms of computational cost. For the case of $SrTiO_3$, for example, a calculation of the induced transverse polarization for a perturbation of a given $\mathbf{q}$ [i.e, Eqs. 2.67 and 3.50] using the metric implementation took less than 17% of the cpu time of the phonon implementation, mostly because separate calculations for the different sublattices was not required. Additional savings in the calculation of the FxE coefficient also come from the fact that a calculation of χ^{mag} is not required for the metric implementation.

Chapter 5

Flexoelectricity for practical applications: Silicon flexovoltaic devices

5.1 Introduction

In this chapter we will describe a practical application of the theory of flexoelectricity to a prototypical solar-cell device, whose field of research already counts a tight synergy between scientific community and industry.

A central issue to improving the efficiency of a solar cell, and ultimately increasing the total photocurrent, consists in reducing the recombination rate of the photo-excited carriers. Since they typically need to travel a long way before reaching the electrodes, nanostructuring, either in the form of wires or membranes, has been explored in recent years as a means of avoiding the above drawback [39]. On one hand, the higher surface-to-volume ratio guarantees that a larger fraction of the electron-hole pairs reaches the boundary; on the other hand, the reduced size allows for a much greater design flexibility, as the bulk material properties can be modified (almost) at will via an appropriate control of morphology and surface chemistry. These effects, however, largely depart from the established working principles of solar cells in use today, calling for a substantial advance in their fundamental understanding in order to be harnessed and exploited in applications.

In this context, mechanical deformations have attracted considerable attention as they can be used, in principle, to enhance the photovoltaic efficiency of an arbitrary nanostructure without degrading the transport properties of the constituent material. Indeed, earlier first-principles calculations of silicon nanowires [90] and nanomembranes [31] indicate that inhomogeneous strain fields can lead to a spatial separation of the wavefunctions associated to the hole and electron states. Recently, very promising experimental results [30, 92] have corroborated the previous theoretical results. However, the theoretical studies performed so far have focused on capturing the total response of a mechanically deformed device, without disentangling the effects of surfaces, quantum confinement and macroscopic deformations. This implies that it is currently difficult to predict whether a given morphology and strain field is beneficial or detrimental to the photovoltaic efficiency of a nanostructure, unless it exactly matches the already studied cases.

The aim of this work is precisely to show how the recent developments in the theory of flexoelectricity allow for an elegant, systematic solution to such key questions. As we will see shortly, flexoelectricity is intimately related to the concept of "absolute deformation potentials", describing the tilt of a given electron band induced by a strain gradient. This connexion will allow us to predict the "effective electric" field acting on the carriers in terms of a small set of materials constants.

The Chapter is structured as follows: in Sec. 5.2 we will present the working principles of a "flexovoltaic" device, i.e. a photovoltaic device whose performance

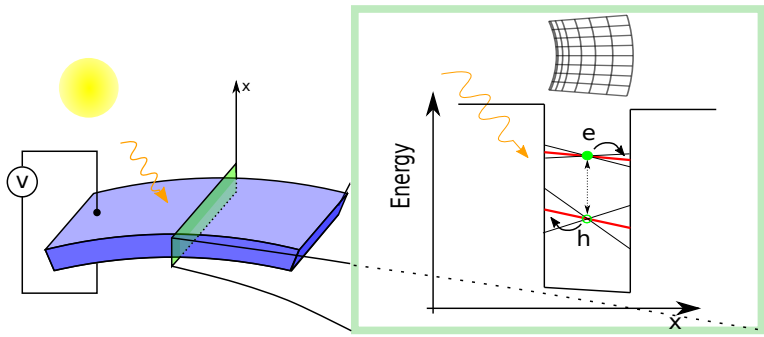

FIGURE 5.1: In a centrosymmetric material, the photoexited carriers have no preferential direction where to migrate, and the recombination rate is high. On the contrary, in presence of a strain-gradient deformation, as induced by simple bending, inversion symmetry is broken, the electronic bands tilt and electron and holes are actively split towards the opposite boundaries generating a *flexo-photovoltage*.

is enhanced by the flexoelectric effect. The theory to analyze the response of such device is presented in Sec. 5.3. Finally in Sec. 5.4 and 5.5 we will apply this theory to crystalline silicon in different geometries and with different electrostatic boundary conditions (EBC).

5.2 The flexovoltaic idea

In order to define the flexoelectric contribution to the photocurrent, the authors of Ref. [30] use the following formula (analogues to the p-n junction case):

$$J = -\mu_e n \mathcal{E}_e + \mu_h p \mathcal{E}_h, \tag{5.1}$$

where μ_e and μ_h are the mobility of the electrons in the CBM and of the holes in the VBM respectively, n and p are the electron and hole densities, and $\mathcal{E}_i$ are the effective electric fields experienced by the electrons and the holes respectively. Such fields are generated by a strain gradient deformation and in general are different as consequence of the fact that the band edges respond differently to the applied strain. The idea is schematically illustrated in Fig. 5.1. Of course, we can not a priory exclude additional contributions to the flexo-photovoltaic effect (e.g. "shift-current" effects to the breakdown of inversion symmetry); we shall defer a more complete analysis to a future study and assume that Eq. 5.1 is the dominant contributions henceforth.

Within such picture, the main ingredients that one needs in order to estimate the performance of flexovoltaic devices are the strain-induced internal fields, $\mathcal{E}_i$, that are "seen" by a photoexcited carrier in a certan energy level i. These quantities are commonly known as absolute deformation potentials (ADPs) [86] in the context of electronic-structure theory, and their calculation might appear, at first sight, straightforward. However the established theory, [62, 86], only addresses the case of *longitudinal* deformations, and neglects the potential contribution of surface effects; both limitations are too drastic for the accurate description of a nanostructure subjected to a realistic deformation field. It was only very recently that, by exploiting the intimate connection between flexoelectricity and the theory of ADPs, it was possible to generalize their definition to an arbitrary strain-gradient component [73], thereby setting the stage for the first-principles design of "flexovoltaic" devices. In the next section we will precisely show the link between the ADP theory and flexoelectricity.

5.3 The theory of absolute deformation potentials

In the previous section we have stressed the importance of studying the variation of the energy levels induced by strain gradient deformations, since they quantify the effective electric field, $\mathcal{E}_i$.

One of the aims of the ADP theory is to establish if the variation of the electronic levels induced by an inhomogeneous strain deformation can be rigorously defined using bulk quantities (and eventually how). If the answer were positive, the ADPs would be truly bulk properties, which do not depend on the surface and geometry of the sample, with remarkable advantages both theoretically and experimentally. Unfortunately this is not always the case. Here we start to revise such theory for the case of an infinite solid, showing its connection to the flexoelectric theory.

First, it is important to observe that the absolute value of any energy level in an infinite solid is defined modulo an arbitrary constant, which is the same for all levels. This arbitrariness reflects the fact that there no a unique choice for the reference energy in an infinite system. (On the contrary, in a finite system this constant is uniquely defined by the geometry of the system and the EBC.) It is sensible to define the difference between a given electronic level $E_{n\mathbf{k}}$ and the average electrostatic potential, ϕ,

$$\tilde{E}_{n\mathbf{k}} = E_{n\mathbf{k}} - \phi, \tag{5.2}$$

where $\mathbf{k}$ is the wave number and n is the band index, which in the present discussion is restricted to be v for the VBM or c for the CBM. From Eq. 5.2 it is clear that

$\tilde{E}_{n\mathbf{k}}$ is well defined at the bulk level, since both $E_{n\mathbf{k}}$ and ϕ are affected by the same arbitrariness.

We now consider an inhomogeneous strain, $\varepsilon_{\alpha\beta}(\mathbf{r})$, that linearly varies along the $\hat{\mathbf{q}}$ direction, $\varepsilon_{\beta\gamma}(\mathbf{r}) = \bar{\varepsilon}_{\beta\gamma}\,\hat{\mathbf{q}}\cdot\mathbf{r}$, and we consider (i) a non piezoelectric crystal, and (ii) well defined EBC along $\hat{\mathbf{q}}$. Adopting a semi-classical picture, in such a way that the inhomogeneous strain varies on a scale much bigger than the crystal unit cell, the ADP, $\mathcal{D}^{\beta\gamma}_{n\mathbf{k}}$, related to the electronic band extreme[1], $\{n\mathbf{k}\}$, is defined as [61, 73]

$$\mathcal{D}^{\beta\gamma}_{n\mathbf{k}}\bar{\varepsilon}_{\beta\gamma} = \frac{\partial\tilde{E}_{n\mathbf{k}}}{\partial\varepsilon_{\beta\gamma}}\bar{\varepsilon}_{\beta\gamma} + \Delta\phi. \tag{5.3}$$

The first term in Eq. 5.3 is the band structure (BS) term, which is local in space and describes the response of the electronic energy band to a uniform strain, $\varepsilon_{\beta\gamma}$, calculated respect to the average electrostatic potential. This is a bulk property and it can be easily obtained using an infinite crystal; it was already treated in the past [12]. The second term in Eq. 5.3 describes the electrostatic potential changes induced by the uniform strain gradient. This term embodies the dependence of ADPs on the macroscopic electric field generated by the strain gradient perturbation [86], and the requirement (ii) is necessary to uniquely define $\Delta\phi$.

Clearly $\Delta\phi$ is non-local since the electrostatic variation in general depends on the charge density response in all space, and therefore one would wonder if it is possible to define such contribution in terms of bulk quantities. Ref. [62] demonstrated that this is the case for of an infinite non-polar crystal (i.e. its Born effective charges are zero), with the constraint of preserving the translational periodicity in the plains perpendicular to $\hat{\mathbf{q}}$. More recently Stengel [73] relaxed the previous requirements by establishing a connection between the flexovoltage coefficients, introduced in Sec. 3.1.4, and $\Delta\phi$. In practice, for a non-piezoelectric crystal, the average electrostatic variation induced by a generic strain gradient that linearly increases along $\hat{\mathbf{q}}$ is [73]

$$\Delta\phi = -e\,\varphi^{\hat{\mathbf{q}}}, \tag{5.4}$$

$$\varphi^{\hat{\mathbf{q}}} = \frac{\mu_{\alpha\lambda,\beta\gamma}}{\epsilon_0\epsilon_{\hat{\mathbf{q}}}}\hat{q}_\alpha\hat{q}_\lambda\hat{q}_\beta\hat{q}_\gamma, \tag{5.5}$$

where $-e$ is the electron charge and $\varphi^{\hat{\mathbf{q}}}$ is the *flexovoltage* (FxV) coefficient, and we have assumed open circuit (OC) EBC along $\mathbf{q}$; $\epsilon_{\hat{\mathbf{q}}} = \hat{\mathbf{q}}\cdot\boldsymbol{\epsilon}\cdot\hat{\mathbf{q}}$ is the relative permittivity, and ϵ_0 is the vacuum permittivity.

[1] for a generic energy level an additional term dependent by the group velocity is present

The established connection between $\Delta\phi$ and the flexoevoltage allows to use Eq. 5.3 in a much broader class of deformations, e.g. involving flexural modes of finite slabs. In particular, the relation 5.5 and 5.4 hold in the latter case, as bending is associated with a strain gradient that is oriented along the radial direction; an unsupported membrane naturally impose OC conditions along the same direction.

We now show how the two contributions to the ADPs can be calculated, with particular reference to the case of silicon. In Sec. 5.5 we will perform an extensive analysis of a silicon membrane in OC EBC. Then, we will move to discuss the changes that affect Eq. 5.5 when SC EBC are considered.

5.3.1 Macroscopic electrostatic term

In the present section we focus on how to extract from first principles the second term of Eq. 5.3, that is the macroscopic electrostatic contribution, via Eq. 5.5.

As shown in Chapter 3, the total flexolectric tensor, Eq. 3.22, is the sum of three contributions: a purely electronic (clamped-ion) term, a "mixed" and a lattice-mediated contribution. In Si only the former two are active, since the Born effective charges identically vanish.

Regarding the mixed contribution, the piezoelectric internal-relaxation term $\Gamma^{\kappa}_{\rho\beta\gamma}$ can be calculated looking at the forces on the atom κ along the Cartesian direction ρ induced by a uniform strain $\varepsilon_{\beta\gamma}$. The polarization response tensor, $\overline{P}^{(1,\lambda)}_{\alpha,\kappa\rho}$, is completely determined by the quadrupoles of the induced charge response to an acoustic phonon, Eq. 3.39. In the case of Silicon crystal [62] the bulk piezoelectric internal-strain tensor has only one independent component, $\Gamma^{\kappa\alpha}_{\beta\gamma} = (-1)^{\kappa}|\epsilon_{\alpha\beta\gamma}|\gamma$, and the same holds for polarization response tensor, $\overline{P}^{(1,\alpha)}_{\beta,\kappa\gamma} = (-1)^{\kappa}|\epsilon_{\alpha\beta\gamma}|\overline{P}^{(1)}$.

We have already discussed different strategies to calculate the electronic flexoelectric contribution. In particular, the most general approach presented in this thesis consists in using the metric wave perturbation together with the current density response, as discussed in Chapter 4. However, since this work on the flexoelectric response of Si was performed before the development of such tools, here we will report the results for the electronic felxoelectric contribution obtained following the strategy of Ref. [78] and outlined in Sec. 3.2.1 for a cubic crystal.

In practice, the three independent components can be calculated as follows: first the two *longitudinal* tensor components along the [100] and [110] crystalllographyc direction, defined in Eq. 3.41, are obtained through the octupolar moments, via Eq. 3.40. Next, in order to obtain the missing independent component of the electronic flexoelectric tensor, we calculate the transverse flexovoltage coefficient by using a slab geometry, as prescribed by Ref. [74, 78]. Indeed, for such geometry

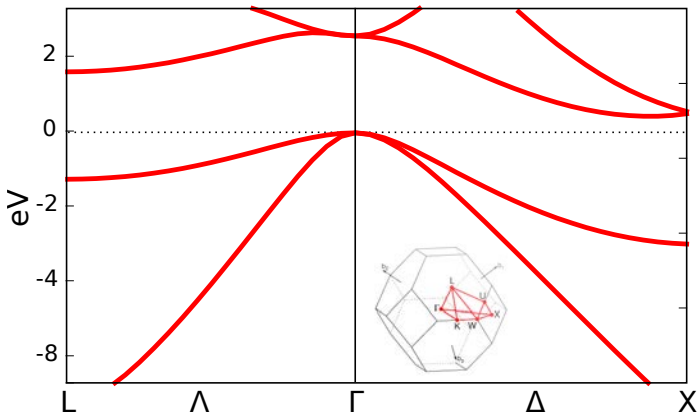

FIGURE 5.2: Electronic bands of bulk Si in the diamond structure using our pseudopotential. The Fermi level is set to zero. The inset shows the Brillouin zone and its high symmetry points (figure from Ref. [72]).

one can demonstrate that the surface contributions do not induce any net charge accumulation (see Appendix B), and therefore the interior electrostatic response is fully determined by the bulk flexoelectric component, μ_{12}, provided that the slab is sufficiently thick.

5.3.2 Band-structure term

The first term of Eq. 5.3 is the so-called band-structure (BS) term, which is the *relative* (referred to the macroscopic electrostatic potential) response of the valence (v) and conduction (c) band edges to a uniform strain. The evaluation of both BS edges is well known [18], and is facilitated by the use of crystal symmetry. In the case of silicon, both the valence band maximum (VBM) and conduction band minimum (CBM) are three-fold degenerate (for simplicity we do not take into account the spin orbit splitting), and they are located respectively at the Γ point and along the three equivalent Δ directions (See Fig. 5.2). The band splitting of the VBM due to a strain ($\varepsilon_{\alpha\beta}$) is described by the eigenvalues of the following matrix [12, 18]:

$$\delta\hat{H}^{BS}_{v,\Gamma} = \begin{pmatrix} l\varepsilon_{xx} + m(\varepsilon_{yy} + \varepsilon_{xx}) & n\varepsilon_{xy} & n\varepsilon_{zx} \\ n\varepsilon_{yx} & l\varepsilon_{yy} + m(\varepsilon_{xx} + \varepsilon_{zz}) & n\varepsilon_{yz} \\ n\varepsilon_{zx} & n\varepsilon_{yz} & l\varepsilon_{zz} + m(\varepsilon_{xx} + \varepsilon_{yy}) \end{pmatrix}, \quad (5.6)$$

where $(l+m)/2$ describes the isotropic BS term, while $(l-m)/2$ and n quantify the splitting induced by a longitudinal and shear strain, respectively. The BS term

related to the CBM located along the direction $\hat{k}$ in the Brillouin zone is [2]

$$D^{BS}_{c,\hat{\mathbf{k}}_i} = \alpha\, tr(\boldsymbol{\varepsilon}) + \beta \hat{\mathbf{k}}_i \cdot \boldsymbol{\varepsilon} \cdot \hat{\mathbf{k}}_i, \tag{5.7}$$

where the index i identifies the CBM along the direction $\hat{\mathbf{k}}_i$ in the reciprocal space (Cartesian coordinates, $i = x, y, z$), and due to the cubic symmetry, $\hat{\mathbf{k}}_i \cdot \boldsymbol{\varepsilon} \cdot \hat{\mathbf{k}}_i = \varepsilon_{ii}$. In Eq. 5.7, α is the uniform shift due to an isotropic deformation and β specify the relative shift between the different valleys.

5.4 Results

After calculating all the independent parameters presented before in order to describe the ADPs related to the VBM and CBM of silicon, we will use these results to study the electronic response of different membranes. In the present case a membrane is defined as a slab which is sufficiently thick to recover the bulk properties in its interior. This includes systems down to few nanometers thick. In the present section we will study the voltage drop in such unsupported systems for different type of strain gradient deformations. In particular we will report the voltage drop in OC EBC, which is the electrostatic condition used to define the open-circuit voltage. In the next section, we will discuss how the results changes in the case of SC EBC.

5.4.1 Bulk material constants

Our calculations are performed in the framework of the local-density approximation to density-functional theory as implemented in the ABINIT [26] code. The core-valence interaction is described by Troullier-Martins [83] norm-conserving pseudopotentials. We used a plane-wave cutoff of 30 Ha and sampled the Brillouin zone of the Si cell by means of a $8 \times 8 \times 8$ Monkhorst-Pack [54] mesh. With these parameters, we obtain an equilibrium lattice parameter of a_0=10.10 bohr and the elastic constants that are $C_{11} = 159.8$ GPa, $C_{12} = 61.7$ GPa and $C_{44} = 76.3$ GPa, and the relative permittivity is $\epsilon = 13.2$, which are in line with literature values.

To calculate the flexoelectric tensor for silicon we focus on the electronic and mixed terms, appearing in Eq. 3.22, separately. We start by calculating the electronic one. Following the procedure detailed in the previous sections and in Ref. [78], first it is required to calculate the longitudinal dynamical octupoles along the [100] and [110] direction, $Q^{(3)}_{[100]}$ and $Q^{(3)}_{[110]}$. The two octupoles can be obtained as in Eq. 4.33,

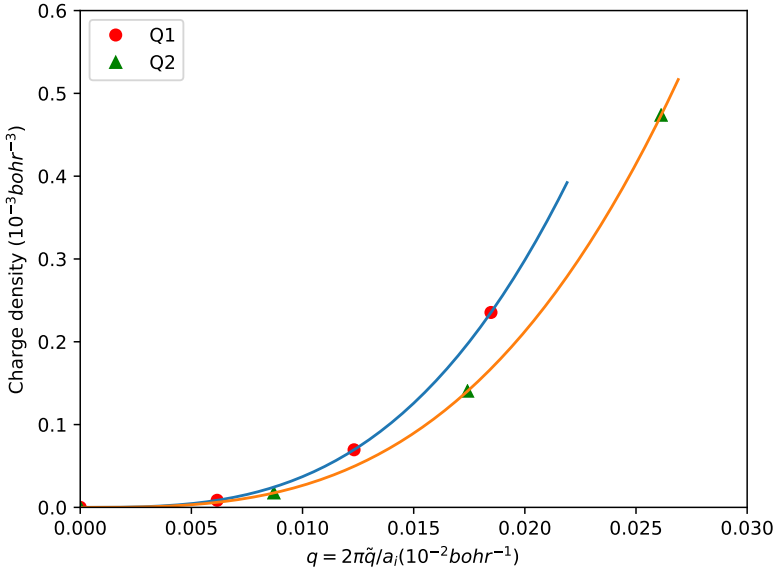

FIGURE 5.3: Fitting procedure to get the longitudinal octupoles, $Q^{(3)}_{[100]}$ and $Q^{(3)}_{[110]}$.

and discussed in Sec. 4.4.4. In Fig. 5.3 we report the imaginary part of $\sum_\kappa \bar{\rho}^{\mathbf{q}}_{\kappa\bar{\mathbf{q}}}$, calculated for $\mathbf{q} = \{0.1, 0.2, 0.3\}$ (in reduced units of $2\pi/a_0$), and for both the longitudinal phonons along the [100] and [110] directions. The cubic fitting of these results gives the following octupolese values (atomic units) $Q^{(3)}_{[100]} = -28.05\,\text{bohr}^2$ and $Q^{(3)}_{[110]} = -56.39\,\text{bohr}^2$, and by Eq. 3.40 they allow to calculate the electronic contribution to the flexoelectric response.

In order to disentangle the information about μ_{12} and μ_{44} contained in $\mu_{[110]}$, we have followed the strategy of Ref. [78], analyzing the response density of a silicon slab geometry (oriented along the (100) direction) to get the transverse flexoelectric tensor, μ_{12}. In practice, we use a slab that is thick five and half conventional bulk cubic cells along the out-of-plane direction, and free surfaces are passivated with H atoms. Such a response is then processed via an external module that solves the Poisson equation in curvilinear coordinates [74]. This gives $\varphi_{12} = -8.93\,\text{V}$. Using the previous calculated values, and reminding the definitions of the two longitudinal FxV coefficients analogous to Eq. 3.41, $\varphi_{[100]} = \varphi_{11}$ and $\varphi_{[110]} = \varphi_{11} + \varphi_{12} + 2\varphi_{44}$, we are able to obtain all the three independent flexovoltage coefficients, which are reported in Tab. 5.2.

(V)		This work	HV	RCB
$\varphi_{[100]}$		-12.03	-11.97	-12.0
$\varphi_{[110]}$	$\varphi^{el}_{[110]}$	-24.19	–	–
	$\varphi^{mix}_{[110]}$	1.84	–	–
	$\varphi^{tot}_{[110]}$	-22.35	-22.22	-22.2

TABLE 5.1: Here are listed the value of the two longitudinal flexovoltage, $\varphi^{tot}_{[100]}$ and $\varphi^{tot}_{[110]}$, which are the only two independent values that can be calculated using the bulk charge density response respectively along the [100] and [110] direction, together with reference values. HV and RCB stand respectively for Ref. [36] and Ref. [62], and remind the difference in the definition of $\mu_{[110]}$ between this work and HV's work. For $\mu_{[110]}$ we have disentangled the two contributions, the electronic and mixed term, tanks to our calculation of $Q^{(2)}$ and Γ.

(V)	φ^{el}			φ^{mix}	φ^{tot}
	(a)	(b)	(c)		
11	-12.15	-12.14	-12.03	–	-12.03
12	-9.03	-9.03	-8.93	–	-8.93
44	-1.63	-1.63	-1.61	0.92	-0.69

TABLE 5.2: Final values of the three independent bulk flexovoltages for silicon. The electronic contributions are compared with other two independent results: (a) are from Ref. [65]; (b) are from the the previous Chapter 4, Tab. 4.4; (c) are the values calculated here.

VB		CB	
l	-14.96	α	-11.61
m	-7.91	β	9.00
n	-9.80		

TABLE 5.3: The parameters that describe the BS deformation potential of silicon to a generic mechanical deformation. Values in eV.

	b	d	Ξ_u	$(\Xi_d + \frac{1}{3}\Xi_u - a)$	a	Ξ_d
this work	-2.35	-5.65	9.00	1.65	-10.26	-11.61
Ref. [87]	-2.35	-5.32	9.16	1.72	–	–

TABLE 5.4: DP, comparison with values reported in Ref. [87]. The relations connecting the present notation to Ref. [87] are: $b = (\frac{l-m}{3})$; $d = \frac{n}{\sqrt{3}}$; $\Xi_u = \beta$; $\Xi_d = \alpha$; $a = \frac{l+2m}{3}$.

Still, the case of [110] the total flexoelectric coefficient has also a non-zero mixed-term contribution, while for $\mu_{[100]}$ it is zero. The value of the quadrupole has been calculated with a fitting procedure similar to the octupole case, and the results is $Q^{(2)} = 1.02$ bohr, while the internal atomic relaxation is $\Gamma = 0.70$ bohr. Summing up all the contributions we obtain the values for $\mu_{[100]}$ and $\mu_{[110]}$ that are reported in Tab. 5.1, compared with previous references.

Regarding the band-structure parameters, we use the finite difference method; in particular, they are calculated by performing simulations of appropriately strained (we use strains of the order of 0.5%) bulk cells. The BS terms for the VBM and CBM are defined by the eigenvalues of $\delta\hat{H}^{BS}_{v,\Gamma}$ and by Eq. 5.7, respectively. The five parameters appearing in Eq. 5.6 and Eq. 5.7 are reported in Tab. 5.3 and a comparison with Ref. [87] is reported in Tab. 5.4, where our parameters have been conveniently converted. The agreement is generally excellent.

5.4.2 Optimal Flexovoltaic silicon membrane

The powerfulness of the present approach illustrated by the number of different membrane geometries for which we are now able to analyze the absolute CBM an VBM response, based on the few parameters calculated in the previous section. As an example, here we have considered membranes oriented along the [100], [111] and [110] direction; their response has been studied as function of the deformation type and its orientation in the surface plane. For sake of clarity, in order to define the deformations treated in the following we refer to Fig. 5.4 where the membrane

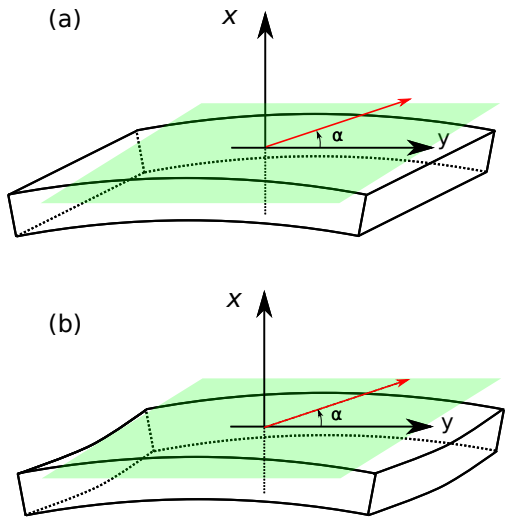

FIGURE 5.4: The two type of deformations considered here: (a) the plate bending; (b) the beam bending. The red line identify the main bending direction, which varies in the green plane and is identified by the angle α.

is oriented along $\hat{x}$ and the main bending is along $\hat{y}$; we consider two different bending types: (I) simple bending plus the longitudinal internal relaxation along the direction normal to the membrane (plate bending), which is defined by the following local effective strain

$$\begin{aligned} \varepsilon_{eff}^{I} &= \varepsilon_{yy} - \nu^{I}\varepsilon_{xx} \\ \nu^{I} &= \frac{C_{12}}{C_{11}} \end{aligned} \tag{5.8}$$

(II) the previous bending, with the longitudinal relaxation, plus the anticlastic relaxation in the third direction (beam bending limit) which is defined by the following effective local effective strain

$$\begin{aligned} \varepsilon_{eff}^{II} &= \varepsilon_{yy} - \nu_{x}^{II}\varepsilon_{xx} - \nu_{z}^{II}\varepsilon_{zz} \\ \nu_{x}^{II} &= \frac{C_{12}C_{13} - C_{11}C_{23}}{C_{13}C_{13} - C_{11}C_{33}} \\ \nu_{z}^{II} &= \frac{C_{13}C_{23} - C_{33C_{12}}}{C_{13}C_{13} - C_{11}C_{33}}. \end{aligned} \tag{5.9}$$

Both deformations are sketched in Fig. 5.4. In practice, for both deformations we vary the main bending direction (red in Fig. 5.4), which is identified by the angle

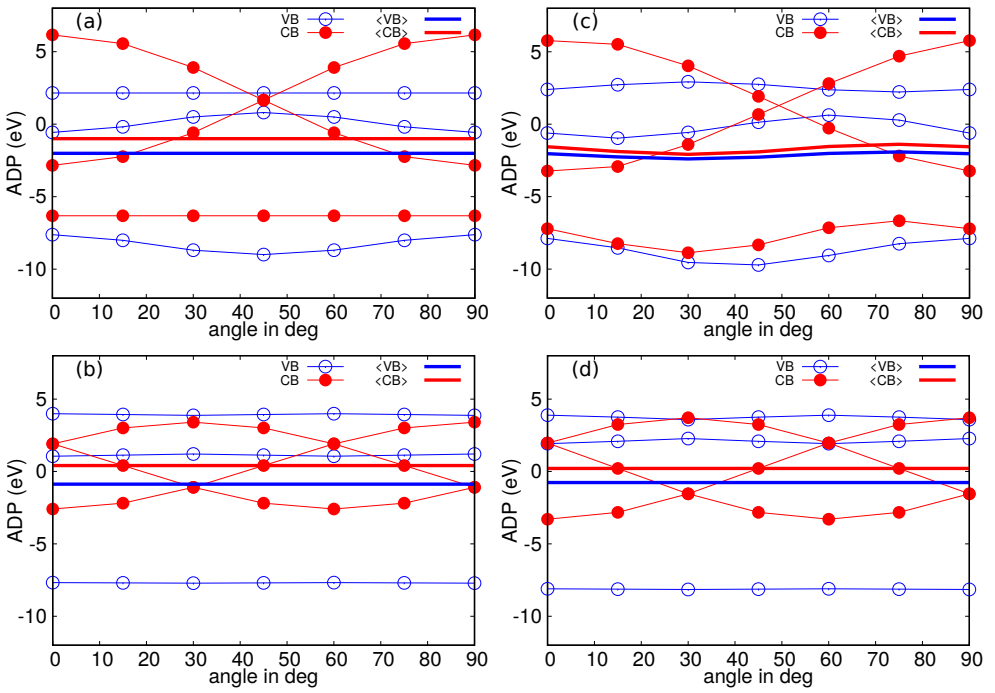

FIGURE 5.5: (a)-(c) show the ADP for a silicon membrane oriented along the [100] direction and deformed as a plate banding and a beam bending respectively. The ADP values are plotted as function of the α parameter that describes the in-plane rotation of the membrane (b)-(d) show the ADP for a silicon membrane oriented along the [11-1] direction, again for the two different types of deformations considered in the text. The $\alpha = 0$ geometry coincide with the pictures represented in Fig. 5.4.

in the surface plane, α, measured anticlockwise from the following reference crystallographic directions (case $\alpha = 0$): [010], [-110] and [1-11] respectively for the slab oriented along the [100], [111] and [110] direction. Therefore for each α value, the definitions in Eq. 5.8 and Eq. 5.9 must be conveniently rotated.

Using the theory described in Sec. 5.3, specialized to the present geometries, we get the ADPs for each single band as function of the α parameter. These results are shown as thin lines in Fig.s 5.5 and 5.6 for the three slabs and the two bending types. It is immediately clear that the single band splitting shows a quite complex response, with both CBM and VBM band subspace displaying splits associated to positive and negative ADPs.

In order to extract a more accessible picture for possible photovoltaic applications, we focus on the ADP averages of the CBM and VBM (the thicker lines in

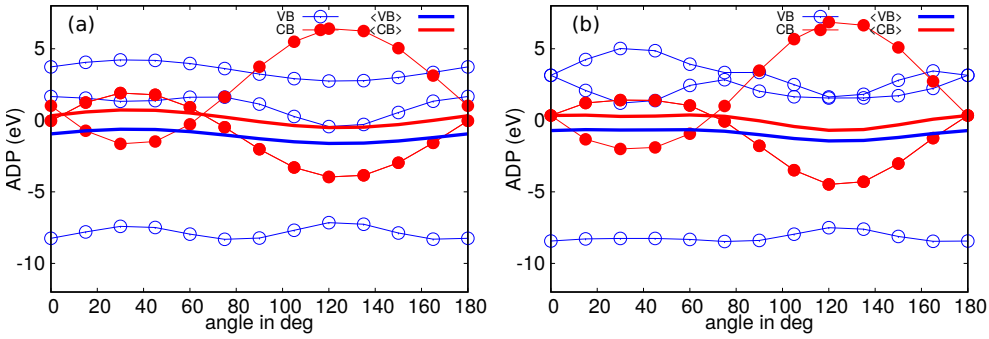

FIGURE 5.6: (a)-(b) show the ADP for a silicon membrane oriented along the [110] direction and deformed as a plate banding and a beam bending respectively. The ADP values are plotted as function of the α parameter that describes the in-plane rotation of the membrane The $\alpha = 0$ geometry coincide with the y-direction that coincides with [1-11].

Fig.s 5.5 and 5.6). Interestingly all the cases studied her show that the VB response is always more negative than the CB. This is a consequence of the fact that under a volume dilation the energy gap of silicon increases. Moving back to our flexovoltaic device, the best geometry that minimizes the electron-hole recombination can be identified by requiring that photo-excited electrons and holes are pushed towards the two opposite surfaces of the membrane. This means that, since electrons and holes have opposite charge, the average ADPs of the conduction and valence band should have the same sign; that is the two type of carriers experience forces in opposite direction. Looking at the [100] membrane results, we see that the *average* ADPs for both the VB and CB have the same sign (negative). On the contrary this is never satisfied for the [111] case, while it is true only for specific α-values in the [110] geometry. We can conclude that only for silicon membrane oriented along the [100], the electrons in the CB and the holes in the VB are pushed on the two opposite surfaces, independently by the in-plane main bending direction. It is finally worth noting that the average ADPs show a clear non trivial α-dependence only for the [110] membrane and in the specific case of beam-bending deformation for the [100] membrane.

Note that in all the directions that we studied, the degeneracy splittings are about an order of magnitude larger than the average (volumetric) shift of the band edges. This means that the response may be more complex than the naive picture of Eq. 5.1.

Comparison with previous works

The previous analysis can be loosely related with the results of Ref. [31], where the authors have carried out the explicit *ab initio* simulation of bent silicon nanostructures with different orientations. While comparing the results obtained in the previous sections with those of Ref. [31] one should keep in mind that the latter are related to systems that are only few atomic layers thick (between 5 and 8 depending by the surface orientation) while the analysis performed in the present Chapter is intended for membranes with thickness around ten nanometers or more.

As result of their study, Guo and Van Hove were able to identify the locations in space of the absolute VBM and CBM. They can be compared with the results obtained for the ADPs of each single splitted band. In particular one must identify the biggest *absolute value* for both the ADPs of the valence and conduction band subspaces; then their sign indicates on which surface is located the edge. For example, Guo and Van Hove obtained that the bended membrane corresponding to our [111]-oriented case with $\alpha = 0$, shows a perfect spatial split of the band edges, located at the two opposite surfaces. The same conclusion can be obtained just looking at Fig. 5.5-(b) and using the above considerations: The highest absolute value between the ADPs of the splitted VBM is -7.67 eV, while for the CBM it is -2.59 eV; since these two band edges have ADPs with the same sign, they must be located on the opposite surfaces of the membrane (remind that electron and hole have opposite charges and thus experience opposite forces.)

Another system explicitly studied in Ref. [31] is the membrane oriented along the [110] with $\alpha = 0$. In this case their main conclusion was that the *global* wavefunction associated to the CMB is not confined on one of the two surfaces but is homogeneously spread along all the thickness of the membrane. Again, the same result can be deduced by looking at Fig. 5.6-(a): the ADPs associated with the CBM are almost zero suggesting a quite flat valence-band edge.

While the present theory is good for unsupported membranes with insulating surfaces, a realistic device, however, needs to have metallic electrodes in order to collect the photocurrent. To describe uch case, the theory developed so far needs to be generalized to the short circuit (SC) case. As we shall see shortly, this can be achieved at the price of only few extra supercell simulations necessary in order to study the band alignment at the interface between the membrane and the metal, and its changes with respect to the applied strain. This is discussed in the next paragraph where we use, as test system, silicon membranes with titanium electrodes.

5.5 Metallic electrodes

The previous study was performed in OC EBC, with major emphasis on the electronic response inside the membrane. As mentioned before, in that particular case the electronic response of the interior of the bended membrane is a bulk property. Here we will focus in more details on the effects produced by SC EBC, which in a realistic setup are enforced by sandwiching the membrane between two short-circuited metallic electrodes. The ADP definition 5.3, where the BS term has been split from the electrostatic response, allows to recast all the changes due to the different EBC in $\Delta\phi$. We will start by a formal analysis; then we will present the numerical results for our target case.

Consider a symmetric membrane, with metallic electrodes grown on both surfaces, in such a way that the unperturbed system is symmetric respect the center of the dielectric. It is useful to develop our analysis by comparing the SC case with an unsupported membrane in OC, and proceed by steps (refer to Fig. 5.7).

We start applying an uniform effective strain, ε_{eff}. For the unsupported system the steps in the electron potential energy profile, Φ_{DV}, corresponding to the surface dipoles vary of the same quantity, $\Delta\Phi_{DV} = d\Phi_{DV}/d\varepsilon_{eff}$. By keeping constant the potential in the vacuum region outside the dielectric and comparing with the unperturbed case, we observe that the electron potential energy has been shifted by an amount proportional to $\Delta\Phi_{DV}$ (Fig. 5.7-(b)). In the SC system the electrostatics is governed by the requirement that the Fermi level of the two metallic electrodes must be always aligned. Since also the electrodes are experiencing the same strain of the dielectric, the difference between the electrostatic potential and the Fermi level in the metal, $\tilde{\varepsilon}_F = \varepsilon_F - \phi$, changes proportionally to $\Delta\tilde{\varepsilon}_F = d\tilde{\varepsilon}_F/d\varepsilon_{eff}$, which is conveniently calculated as the bulk variation of $\tilde{\varepsilon}_F$ induced by ε_{eff} at fixed ε_F. It follows that the electron potential energy inside the dielectric is rigidly shifted of $\Delta\tilde{\varepsilon}_F$ (green line in Fig. 5.7-(e)). However, as in the OC case, also the interface dipole varies, $\Delta\Phi_{DM}$. Then, the total variation inside the dielectric of the electron potential energy respect to the unperturbed case is the sum of the two contributions: $\Delta\tilde{\varepsilon}_F + \Delta\Phi_{DM}$; the first one is a bulk property of the metal, while the second is a interface property.

We now move to the bending case, The effective strain in the center of the membrane is zero, while the surfaces are experiencing an opposite local strain. As already discussed in Sec. 3.1.4, for the unsupported membrane in OC the previous surface effects are now opposite. Moreover, inside the membrane the electron potential energy will be tilted due to the bulk FxE response. Then, we have reobtained the conclusions of Sec. 3.1.4, stating that the internal electrostatic response

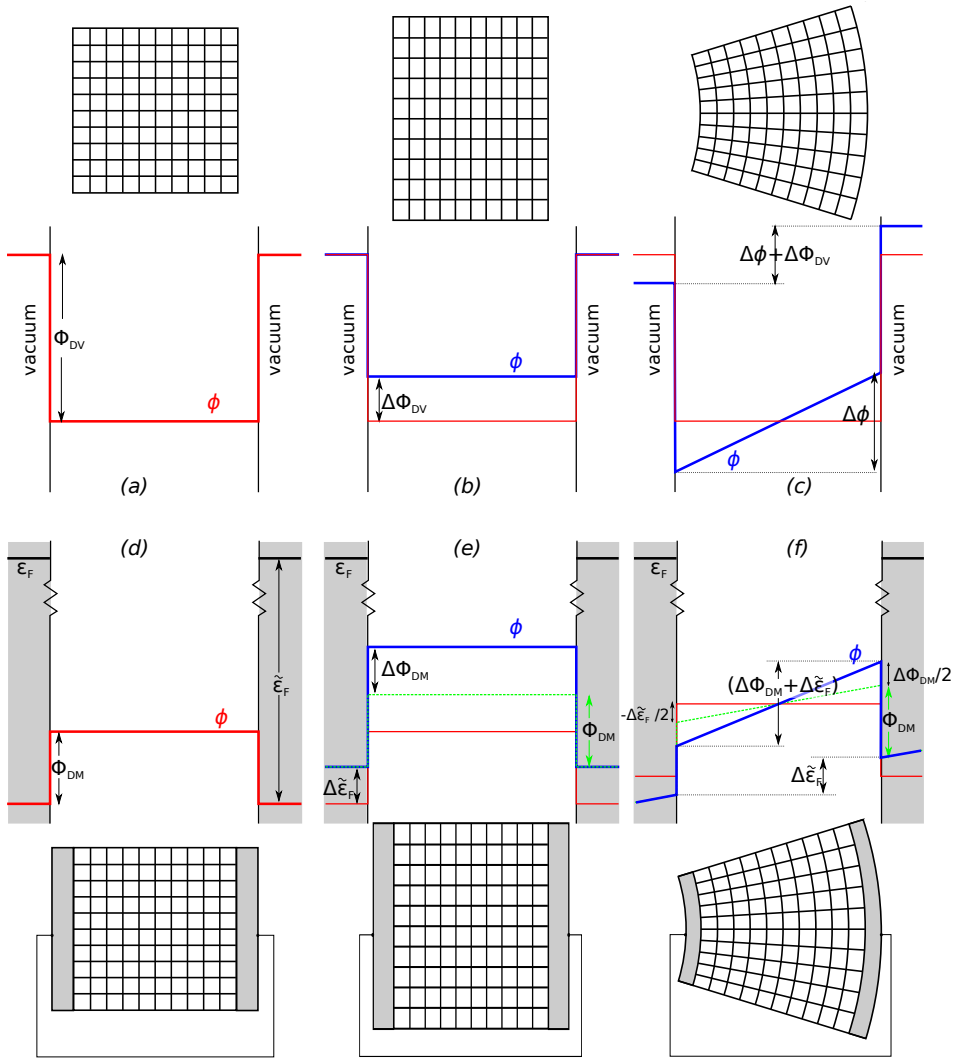

FIGURE 5.7: Electronic potential energy profile across the dielectric membrane for the unsupported open circuit case (a,b,c), and for the short circuit case, in which it has been added two metallic electrodes (d,e,f). (a,d) show the unperturbed systems; (b-e) show the effects of a uniform strain ($\varepsilon = 1$); (c-f) show the effects of a uniform strain gradient ($\Delta\varepsilon = 1/t$ where t is the thickness of the membrane). Legend of colors for the electronic energy profile: red is the unperturbed case; green-dashed (only for the SC cases) is an intermediated step, where only the effects of $\Delta\tilde{\varepsilon}_F$ are considered; blue is the final results for the mechanically perturbed cases. Finally, the black lines in the SC cases are the Fermi level.

is simply a bulk property. On the contrary, both surface and bulk effects will contribute to the total response of the membrane (Fig. 5.7-(c)): the electron potential energy difference between the two vacuum regions is proportional to $\Delta\Phi_{DV} + \Delta\phi$, where $\Delta\phi$ was defined as minus the flexoevoltage response, Eq. 5.5, in eV units.

To understand the bending effects in SC EBC, the starting point is again the Fermi level inside the two opposite electrodes, which must be aligned. Since the metallic electrodes are also experiencing a strain gradient deformation, their electrostatic potential is tilted. This would induce a tilt in the electron potential energy inside the dielectric, which is proportional to $\Delta\tilde{\varepsilon}_F$ (green line in Fig. 5.7-(f)). Still, this is not the only contribution, since also the interface dipoles change of an opposite quantity, generating a further tilt in the electron potential energy of the dielectric that is proportional to $\Delta\Phi_{DM}$. By means of the previous analysis we can conclude that in the SC case, the bulk flexoelectric response is completely screened, but the dielectric still experiences an effective electric field. In the framework of the ADFs theory, Eq. 5.3, this can be included by substituting Eq. 5.5 with

$$\Delta\phi = (\Delta\Phi_{DM} + \Delta\tilde{\varepsilon}_F)\left(\varepsilon_{eff}\Big|_{\text{surf}_R} - \varepsilon_{eff}\Big|_{\text{surf}_L}\right), \tag{5.10}$$

where ε_{eff} is the local effective strain on right (R) and (L) surface.

In conclusion the electron potential energy inside the dielectric undergoes to a tilt respect to the unpertrubed case, $\Delta\phi$, which is entirely deremined by the metal and the surface specific properties.

We now specialize the previous analysis to a concrete case: a silicon membrane oriented along the [100] direction and perturbed by a flexural deformation in the plate-bending regime (in our previous notation it would be a type I deformation with $\alpha = 0$). The metallic electrodes considered here are Ti; in particular we impose the Ti crystal to be in a FCC structure distorted to a tetragonal shape, with an in-plane lattice parameter compressed of 5 % respect to its pristine structure, in order to match half the diagonal of the silicon cubic face. Due to geometry considerations, there are two obvious choices to define the interface between the two elements; the first Ti layer can be aligned with the first or the second to the last Si layer. We adopt the latter case since it is energetically favourable. Even though this structure is artificial, it allows to highlight the main features of the present analysis. By employing a supercell with 22 Si layers and 20 Ti layers, we get the band-alignment diagram shown in Fig. 5.8.

Using a finite difference method, where we compare the variation of the electrostatic potential line-up due to a uniform effective strain defined by Eq. 5.8, we

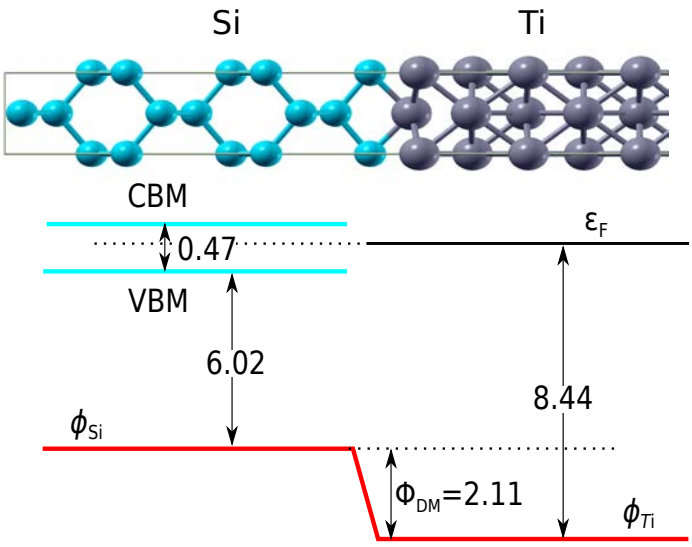

FIGURE 5.8: Bands end electron potential energy alignment at the Si-Ti interfaces. Values in eV.

obtain $\Delta\Phi_{DM} = 4.30$ eV. From bulk simulation of our strained FCC reference structure for the Ti atom we calculate $\Delta\tilde{\varepsilon}_F = 2.16$ eV. Finally, the bulk BS values for the average VBM and CBM manifold for the present case are -6.30 eV and -5.28 eV, respectively. With these values, we are able to calculate the band profile for a generic bending value, $\Delta\varepsilon_{eff}$. In Fig. 5.9 we report the result for an effective strain gradient that is equal to $\Delta\varepsilon_{eff} = 0.1/t$, where t is the thickness of the membrane.

As we have done for the introductory analysis related to Fig. 5.7, we compare this result with a the correspondent OC silicon membrane, whose dangling bonds at the surface have been passivated with H atoms, and experiencing the same effective strain. For such geometry we obtain $\Delta\Phi_{DV} = -4.60$ eV, while using the result reported in Tab. 5.2 we obtain a bulk flexovoltage contributions of $\Delta\phi = 4.34$ eV. Using the same BS terms as before, we obtain the band profile of Fig. 5.10.

We observe that in both cases there is a partial cancellation between $\Delta\phi$ and the BS terms. Nevertheless, the VBM and CBM still are tilted across the longitudinal direction of the membrane, resulting in a non-zero effective field experienced by the photo-excited carriers. In particular we observe that in the two different configuration the effective electric field change sign, and while in the OC case the VBM is more tilted than the CBM, in the SC case is the other way around.

In conclusion, we believe to have given a remarkable proof of the possible application of the FxE theory, when combined with the theory of ADPs, to engineering optimal flexovoltaic devices.

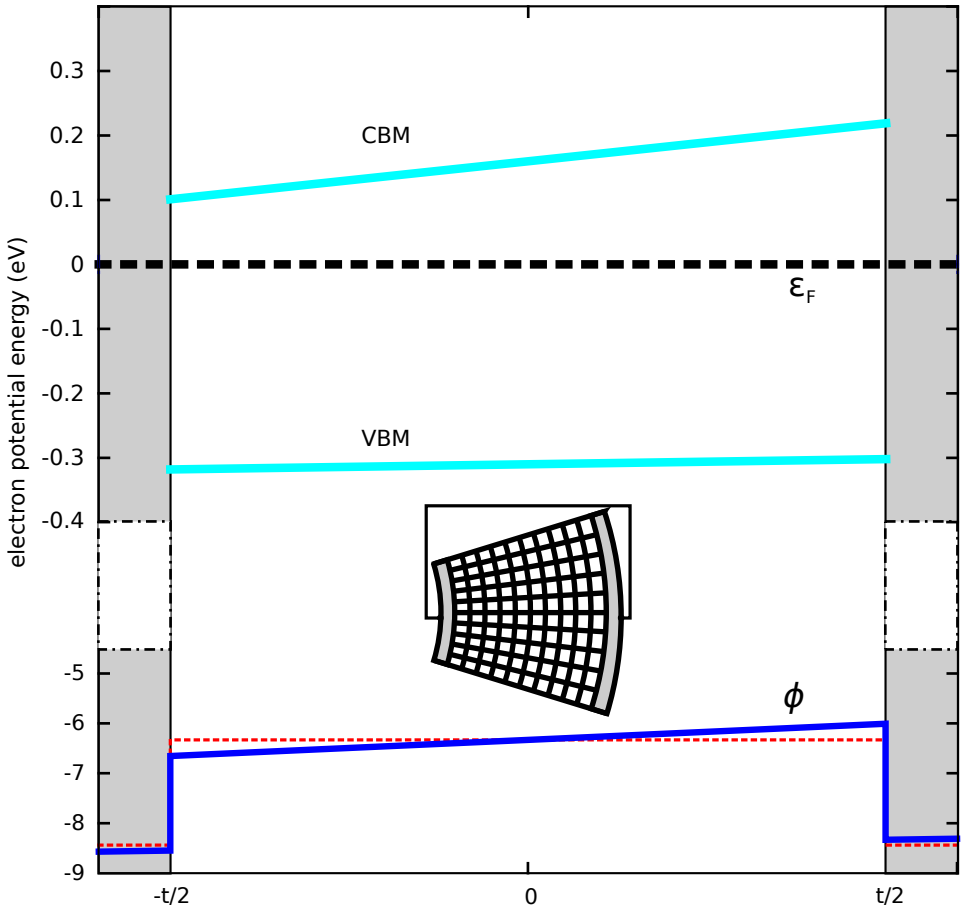

FIGURE 5.9: Electron potential energy and band profiles for the silicon membrane with short-circuited Ti electrodes, oriented along the [100] direction in the plate bending regime. The applied strain gradient is: $\Delta\varepsilon_{eff} = 0.1/t$, where t is the membrane thickness. This corresponds to a curvature radius of $R = 10t$.

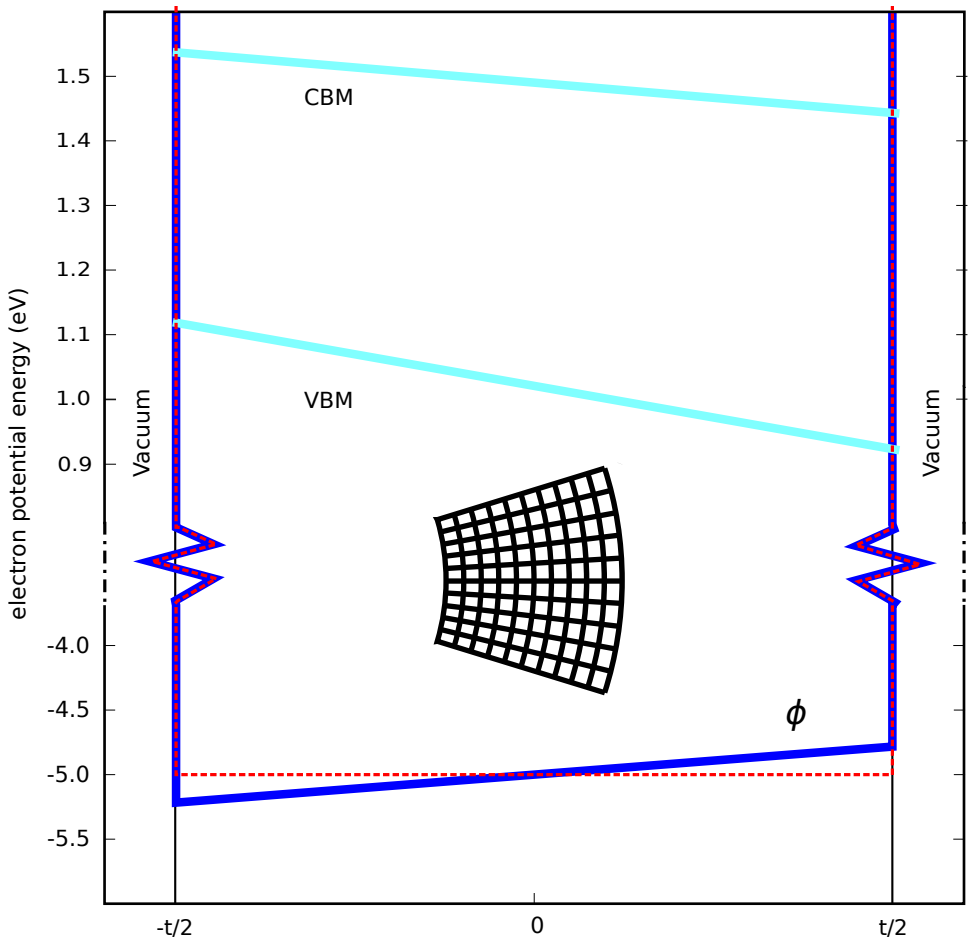

FIGURE 5.10: Electron potential energy and band profiles for the unsupported silicon membrane with surfaces passivated by H atoms. The applied strain gradient is: $\Delta\varepsilon_{eff} = 0.1/t$, where t is the membrane thickness.

Chapter 6

Polar ferroelastic twin walls in $SrTiO_3$

6.1 Introduction

The first-principles theory of flexoelectricity developed in the first half of this work was employed in Chapter 5 in order to study how different silicon geometries can be engineered for solar-cell applications. In this Chapter we will discuss another example where the flexoelectric response of an insulating crystal plays a remarkable role and its correct description is essential to capture the global physical response of the system. In addition to the focus on flexoelectricity itself, one of the main aims of this Chapter consists in presenting a generalized methodology to study the crystal response to other inhomogeneous perturbations. This generalization, which closely follows Ref. [73], is based on a long-wave expansion of the dynamical matrix, and it establishes an ideal foundation to develop accurate effective models starting from full *ab initio* results.

Effective models are essential to study a variety of systems that are too large to be treated fully from first principles and/or when the goal is to rationalize a given physical effect by using only the most relevant order parameters. These models are inspired to the phenomenological Landau theories, especially useful to capture the essential physics involved in phase transitions. Here we will develop an effective energy expansion in order to study the polarity at the ferroelastic domain walls in $SrTiO_3$ (STO).

Domain walls (DWs) usually show up in the low-temperature phases of ferroic crystals, which are characterized by a lower symmetry respect to the higher temperature phase. The transition can be understood by identifying a primary order parameter, associated with a given crystal distortion that condensates below the transition temperature. The energy landscape of the low temperature phase is characterized by different minima, all with the same energy. These minima correspond to equivalent structures, but with the primary order parameter pointing in distinct spatial directions. All these equivalent structure typically coexist in the low temperature phase, in different regions called "domains". Connecting the domains there are the domain walls (DWs) that are the regions where the primary order parameter shows a discontinuity and changes sign.

DWs, especially in ferroic materials, are a recognized source of unusual physical effects. Indeed, in the DW region one or more degrees of freedom undergo to a large variation on a short length scale, which means that *gradient couplings* (e.g., flexoelectricity) can have a strong impact on the local physics. Recently these unusual physical effects where employed for electronic device applications [13]. Therefore a theoretical understanding and rationalization of the DW properties is crucial.

Here we focus on the emergence of polarity at DWs that divide two nonpolar phases. More specifically we will focus on ferroelastic twin boundaries (TBs), which are walls separating twin phases where a strain component changes sign.

In this context the orthorhombic $CaTiO_3$ (CTO) is the first and best studied example. CTO is a cubic perovskite at high temperature that undergoes to a phase transition to an anti-ferrodistortive (AFD) phase, which is characterized by the non-polar rotations of the oxygen octahedra. The AFD phase in CTO is defined by a complex pattern of octahedron rotations that is the combination of two anti-phase rotations along two Cartesian axis and an in-phase rotation along the third one ($a^-a^-c^+$ in Glazer notation). The ferroelastic DWs of the low temperature non-polar phase were first theoretically predicted to show a local polarity via an empirical atomistic model [24], and later transmission electron microscopy results confirmed [1] the prediction. Recently a first-principles [3] analysis on the origin of the ferroelastic DWs in CTO has postulated an *improper* origin of the polarization, which would emerge from trilinear couplings between tilt modes that are enabled in the domain-wall region. Therefore, while the polar behaviour of the TBs in CTO is now demonstrated, its origin seems to be quite complex involving both gradient-mediated and anharmonic terms.

STO is another perovskite with a ferroelastic phase that is induced by AFD tilts below 105 K, but with a simpler structure: the oxygen octhaedron rotate in anti-phase along one of the three fold Cartesian axis ($a^0a^0c^-$) only. The oxygen rotations also induce a deformation of the original cubic cell that becomes tetragonal (elongated in the same direction of the octahedron rotation axis). Moreover STO is an incipient ferroelectric, i.e. it has a very soft polar mode, and it can become ferroelectric, for example, by just applying external strain [32]. At DWs the inversion symmetry of the teragonal phase is locally broken, and hence DWs could show a polar behaviour, even if the bulk ferroelastic domains are nonpolar [68]. Therefore TBs of STO are very promising candidates where looking for a polar response of non polar crystals.

Existing phenomenological works emphasized a flexoelectric origin of the polarization at twin boundaries in $SrTiO_3$ since it is a universal effect of all insulators [55]. Such an interpretation was confirmed by numerical simulations based on a simplified atomistic model [70]. However one could wonder if flexoelectricity is the only main contribution to the polar response of TWs in STO, or if other "improper" mechanisms, for example similar to the tri-linear coupling proposed for CTO [3], play a relevant physical role. Direct experimental evidence of polarity at the TWs of STO is scarce, and mostly indirect evidence of a polar response was

reported [69]. Thus for STO, in contrast to CTO, even a clarification on the real existence of a polar response at the TBs is needed. [Only very recent work has reported a direct signal of polarity at the TWs in STO [21].]

In this scenario, two are the main points that we plan to address in the present work: (i) demonstrate the polarity at the TBs in STO on the base of an *ab initio* study: phenomenological theories and empirical potentials can hardly push their accuracy beyond order-of-magnitude estimates (many of the relevant coupling coefficients, e.g. the flexoelectric tensor, are difficult to access experimentally); (ii) understand the microscopic physical origin of this polarity, by looking at the couplings that may induce a polar response, including gradient-mediated and "improper" couplings.

In order to answer to these questions we will construct an effective energy expansion, which is function of few relevant order parameters, by starting from full DFT calculations and performing a series of well defined approximations. This is a novel procedure that is based on the long-wavelength expansion of the linear and nonlinear interatomic force constants (IFCs) of the reference bulk phase. It is a quite general procedure that can be applied to other systems where gradient terms play a relevant role. Therefore the first part of this Chapter is devoted to presenting the approach for extracting the effective energy expansion. In the second part, this continuum model is employed in order to study the polarity at the TWs of STO.

6.1.1 Geometry of the problem

First of all it is important to fix the geometry of ferroelastic DWs in STO. The conventional tetragonal cell of the unrelaxed AFD phase ($a^0a^0c^-$) is shown in Fig. 6.1-(a). Its volume is four times the primitive cubic cell, with translation vectors $\mathbf{a}_1 = a_0/\sqrt{2}(1,1,0)$, $\mathbf{a}_2 = a_0/\sqrt{2}(-1,1,0)$ and $\mathbf{a}_3 = a_0(0,0,1)$, and the AFD axis oriented along the third. We shall use the 20-atoms cell for the high temperature phase, Fig. 6.1-(d), and we will refer to it as the "conventional tetragonal cell" of the cubic phase.

Moving now to the ferroeleastic DWs, the plane of the walls is oriented perpendicular to the [110] pseudocubic direction, $\hat{s}$ direction, and it separates two AFD domains, whose respective oxygen tilt axes are oriented at 90° with respect to each, Fig 6.1. This geometry has the great advantage that originates a one-dimensional (1D) problem [11, 55]. Indeed one can identify the relevant vector or tensor quantities by projecting them on the perpendicular, $\hat{s}$, or parallel, $\hat{r}$=[1-10], directions to the wall, while the third remaining direction coincides with the Cartesian axis $\hat{x}$. The AFD pseudovector, which identifies the oxygen octahedral rotations, has two

components, ϕ_s and ϕ_r, respectively. In this scenario it is the shear tensor component, ε_{rs}, that change sign across the ferroelestic DW. Moreover, by symmetry, the only in-homogeneous spacial direction is $\hat{s}$, while the macroscopic polar response is only allowed by symmetry along the $\hat{r}$ direction. (The polarization response is always perpendicular to the gradient direction.) This last observation will be essential while developing a microscopic theory, in order to work in well defined electrostatic boundary conditions. Note that two different twin wall (TW) types exist in STO, differing by the AFD pseudovector component, ϕ_r or ϕ_s, that changes sign across the wall. We shall indicate as "head-to-tail" (HT) and "head-to-head" (HH) the case where respectively ϕ_r and ϕ_s changes sign (see Fig. 6.1.(e-f)); They are respectively equal to the "tail-to-head" (TH) and "tail-to-tail" (TT) case.

In the result section we will perform a detailed comparison on the polar origin at the TWs in STO for the two types. As result we get that the two DWs have a different total polarization response and therefore they can be potentially identified by its interaction with an external electric field.

6.2 A multiscale harmonic approach

In order to build phenomenological energy expansions, the most popular strategy can be summarized as follows: (i) choose the relevant order parameters for describing the system under study; (ii) build an expression for the energy as function of the previously identified order parameters by taking into account the symmetries of the crystal (which can eventually forbid given coupling terms); (iii) set the value of the coupling coefficients for example using experimental results or calculating them by first principles simulations. Clearly, employing *ab initio* simulations in order to extract coupling coefficients has the advantage of corroborate the study on a strong background that is free of phenomenological inputs. The power of this approach has been shown for studying bulk homogeneous phases and phase transitions [93], where only coupling between uniform order parameters are involved, and thus they can be easily calculated within bulk simulations.

When dealing with inhomogeneous systems, where one or more order parameters are function of the position in space, e.g. the case of DWs, then gradient-mediated terms can not be discarded and they must be included into the energy expansion. As an example one can specialize the model in Ref. [20] to the geometry described in section 6.1.1 for ferroelastic DWs in STO; the results is a 1D phenomenological energy expansion that is function of the polarization P along the direction $\hat{r}$, the strain, $\varepsilon_{\alpha\beta}$, and the two AFD order parameters, ϕ_r and ϕ_s. The

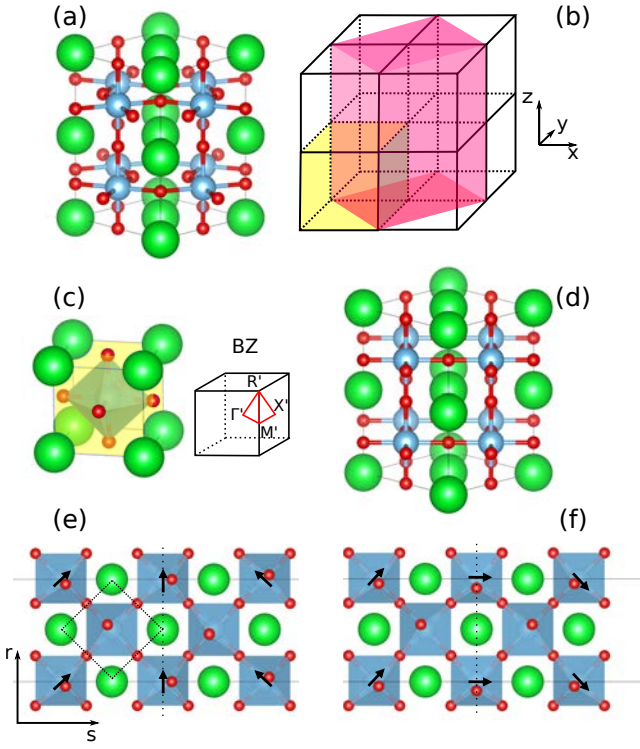

FIGURE 6.1: (a): Un-relaxed tetragonal cell of the AFD phase; (b): Simplified sketch that compare the primitive cubic cell of the high temperature phase (yellow cube) with respect the tetragonal cell; (c) Cubic primitive cell of the High temperature phase; (d): Conventional tetragonal cell, whose volume coincide with the cell in (a) but here the phase structure is the cubic one; (e-f): Schematic illustration of the two different TBs considered in this work, respectively HH (e) and HT (f) configurations; dashed square indicates the primitive cell of the cubic reference phase and arrows indicate the local tilt vector.

explicit expression is

$$\begin{aligned}\mathcal{E} =& \frac{C_{\alpha\beta,\gamma\delta}}{2}\varepsilon_{\alpha\beta}\varepsilon_{\gamma\delta} + \frac{1}{2\chi_0}P^2 + \frac{k}{2}|\boldsymbol{\phi}|^2 + A|\boldsymbol{\phi}|^4 - e_\alpha\varepsilon_{\alpha\alpha}P^2 - R_{ij\alpha\beta}\phi_i\phi_j\varepsilon_{\alpha\beta} - Q_i\phi_i^2P^2 \\ &+ \frac{D_i}{2}(\partial\phi_i)^2 + \frac{G}{2}(\partial P)^2 - fP\partial\varepsilon_{rs},\end{aligned} \tag{6.1}$$

where the Latin indices run over $\{\hat{r},\hat{s}\}$ while the Greek indices run over $\{\hat{r},\hat{s},\hat{x}\}$. All independent order parameters in Eq. 6.1 are only function of the s coordinate, thus all the derivate must be intended along the $\hat{s}$ direction. In Eq. 6.1 the homogeneous couplings are the elastic coefficient, $C_{\alpha\beta,\gamma\delta}$, the isotropic electric susceptibility, χ_0, the quadratic and quartic energy coefficients associated to the oxygen tilts, κ and A, which describe the double well potential associated to the tilts, the electrostricition coupling e_α, the rotostriction coupling, $R_{ij\alpha\beta}$, the biquadratic coupling, Q_i; on the other side the gradient mediated couplings are the self-dispersion of the polarization and the oxygen rotations, respectively G and D_i, and the flexoelectric coupling f.

The presence of gradient-mediated couplings brings up the problem of how they can be calculated *ab initio*. Indeed, as discussed in Chapter 3, the periodic boundary conditions enforced in first principles calculations clash with the concept of spacial gradients. To overcome these difficulties, inspired by the bulk theory of flexoelectricity, we will generalize the concept of long wave expansion of the forces induced by an acoustic phonon to the case of an arbitrary lattice distortion. The idea is that the real-space gradient of a given order parameter can be related to the dispersion of specific microscopic modes around the Γ point. Therefore, by identifying a connection between a specific set of normal modes at the Γ point with the continuum vector fields it is possible to obtain a macroscopic model starting from the dynamical matrix.

In contrast to the normal procedure, where DFT calculations are employed only as a final step to calculate the energy couplings, here we shall enforce a much deeper connection to the full DFT Hamiltonian, and construct the effective continuum model via a series of well defined approximations. In the following of this section we will show in detail this procedure using the ferroelastic DWs of STO as a test case. The final result will be an effective energy expansion similar to Eq. 6.1, where each coefficient is connected to a well defined microscopic *ab initio* quantity, including the gradient-mediated couplings.

6.2.1 The microscopic model

The first step consists in building a microscopic model that describes the energetics of the crystal distortions; the aim is to get phonon dispersions that match the full *ab initio* results. In the harmonic approximation, the Lagrangian density as function of the atomic displacements, $\mathbf{u}_\kappa^l$, is

$$\mathcal{L}(u_{l\kappa\alpha}, \dot{u}_{l\kappa\alpha}) = \frac{1}{2\Omega}\sum_{l\alpha\kappa} m_\kappa (\dot{u}_{l\kappa\alpha})^2 - \frac{1}{2\Omega}\sum_{l\kappa l'k'} \mathbf{u}_\kappa^l \cdot \mathbf{\Phi}_{\kappa k'}^{ll'} \cdot \mathbf{u}_{\kappa'}^{l'}. \tag{6.2}$$

where κ label the atomic spice and l the unit cell, and $\mathbf{\Phi}_{\kappa k'}^{ll'}$ is the force constant matrix. Taking advantage of the periodicity of the crystal, one can use the Fourier transform of the displacement vectors

$$\mathbf{u}_\kappa^l = \frac{\Omega}{(2\pi)^2}\int_{BZ} d^3q\, \mathbf{u}_\kappa^{\mathbf{q}} e^{i\mathbf{q}\cdot\mathbf{R}_l}. \tag{6.3}$$

Then, by defining the Lagrangian density in reciprocal space as [75]

$$\int_\Omega \mathcal{L}\, d^3r = \frac{\Omega}{(2\pi)^3}\int \mathcal{L}^{\mathbf{q}}\, d^3q, \tag{6.4}$$

one obtains

$$\mathcal{L}^{\mathbf{q}}(u_{\kappa\alpha}^{\mathbf{q}}, \dot{u}_{\kappa\alpha}^{\mathbf{q}}) = \frac{1}{2\Omega}\sum_{\alpha\kappa} m_\kappa (\dot{u}_{\kappa\alpha}^{\mathbf{q}})^2 - \frac{1}{2\Omega}\sum_{\kappa k'} \mathbf{u}_\kappa^{\mathbf{q}} \cdot \mathbf{\Phi}_{\kappa k'}^{\mathbf{q}} \mathbf{u}_{\kappa'}^{\mathbf{q}} \tag{6.5}$$

where $\Phi_{\kappa\alpha,\kappa'\beta}^{\mathbf{q}}$ is defined in Appendix A.

Following a common procedure, it is possible to solve the previous dynamical problem by using the normal modes and decoupling the sublattice displacements into the sum of independent harmonic oscillators:

$$\mathcal{L}^{\mathbf{q}}(v_w^{\mathbf{q}}, \dot{v}_w^{\mathbf{q}}) = \frac{1}{2\Omega}\sum_w M_w \left((\dot{v}_w^{\mathbf{q}})^2 - (\omega_w^{\mathbf{q}})^2 v_w^{\mathbf{q}\,2} \right), \tag{6.6}$$

where $v_w^{\mathbf{q}}$ is the amplitude of the normal mode, w, M_w are for the moment arbitrary mass constants and their values are chosen by the physical units that we will assign to the amplitudes of each mode, and $(\omega_w^{\mathbf{q}})^2$ are the eigenvalues of the dynamical matrix,

$$\hat{D}_{\kappa\alpha,\kappa'\beta}^{\mathbf{q}} = |\kappa\alpha\rangle \frac{\Phi_{\kappa\alpha,\kappa'\beta}^{\mathbf{q}}}{\sqrt{m_\kappa m'_\kappa}} \langle\kappa'\beta|. \tag{6.7}$$

[For clarity of notation one has $\langle w\mathbf{q}|\hat{D}^{\mathbf{q}}|lk\mathbf{q}\rangle = \delta_{wk}\left(\omega_w^{\mathbf{q}}\right)^2$, where $|w\mathbf{q}\rangle$ are the unitary lattice distortion.] The normal modes are related to the collective atomic displacements, $u_{\kappa\alpha}^{w\mathbf{q}}$, by

$$u_{\kappa\alpha}^{w\mathbf{q}} = v_w^{\mathbf{q}}\sqrt{\frac{M_w}{m_\kappa}}\langle\kappa\alpha|w\mathbf{q}\rangle. \tag{6.8}$$

As we will show shortly, the amplitudes $v_w^{\mathbf{q}}$ of the Γ modes will be the link between the microscopic theory to the macroscopic continuum model, since they can be identified as the macroscopic order parameters.

The next step towards a macroscopic model consists in rewriting Eq. 6.5 by explicitly using only the vectors associated to the Γ point, $|w0\rangle$. This is justified by the fact that $|w0\rangle$ is a complete basis for representing all the relevant modes in the conventional 20-atom cell, and moreover the displacements at Γ are by definition macroscopic distortions of the lattice. Then, the projection of the generic normal mode, $|k\mathbf{q}\rangle$, on the Γ basis set, $|w\rangle = |w0\rangle$, gives

$$\mathcal{L}^{\mathbf{q}}(v_k, \dot{v}_k) = \frac{1}{2\Omega}\left(\sum_k M_k(\dot{v}_k)^2 - \sum_{kw}\sqrt{M_k M_w}\langle k|\hat{D}^{\mathbf{q}}|w\rangle\,\tilde{v}_k^{\mathbf{q}}\tilde{v}_w^{\mathbf{q}}\right), \tag{6.9}$$

where $\tilde{v}_w^{\mathbf{q}} = \sum_{k'} v_{k'}^{\mathbf{q}}\langle w|k'\mathbf{q}\rangle$. Note that now the dynamical matrix at a generic $\mathbf{q}$ point can couple different eigenmodes, $w \neq k$.

Eq. 6.9 is still exact, i.e. it is just a different form of writing Eq. 6.2. Now, we will perform the long wave expansion of Eq. 6.9. In practice the dynamical matrix must be expanded as shown in Ref. [75]. Here we have decided to include up to the flexoelectric terms. Since the lattice mediated flexoelectric contribution is related to the second derivative of the force constant matrix respect to $\mathbf{q}$ (see Chapter 3), then we carry out the expansion up to the $\mathbf{q}^2$ terms. Therefore the dynamical matrix in Eq. 6.9 is replaced by the following approximation

$$D^{\mathbf{q}} \approx D^{(0)} - iq_\gamma D^{(1,q_\gamma)} - \frac{q_\gamma q_\delta}{2}D^{(2,q_\gamma q_\delta)}, \tag{6.10}$$

where the same notation of Eq. 3.15 has been used. From a mathematical point of view the approximation 6.10 holds as far as the $\tilde{v}^{\mathbf{q}}$ rapidly vanish far from Γ (i.e. the associated continuum parameter defined in Eq. 6.14 is a smooth on the scale of the lattice spacing).

The expansion 6.10 has the usual problem related to the fact that the dynamical matrix is not analytic in a neighbourhood of Γ. This issue was already discussed in paragraph 3.1.3, and it is caused by longitudinal macroscopic electric fields induced by polar displacements. However, since our present focus is on the polarization

parallel to the wall plane, $\hat{r}$, and we are working within a 1D problem, macroscopic field are irrelevant and no further precaution is needed.

Before moving on and dealing with a second crucial approximation, it is important to discuss the symmetry of the $|w\rangle$ modes. As we have stressed before, for the STO case the dynamical matrix is related to the conventional tetragonal cell of the undistorted cubic phase. However, since the primitive cell of such phase is the cubic one, which is four times smaller than the conventional cell, then the Γ eigenvectors of the former coincide, by a one-to-one relation, with the eigenvectors associated to the Γ', R', M' and X' point of the irreducible BZ of the cubic primitive cell - the prime is added to distinguish points in the BZ related to the cubic primitive cell. Then each mode $|w\rangle$ uniquely belongs to one of the four high symmetry points in the irreducible Brillouin zone (BZ) of the cubic primitive cell. It follows that the Lagrangian 6.9 can be rewritten in a clearer form, since at the harmonic level couplings between eigenmodes of different symmetry are not allowed; therefore one obtains

$$\mathcal{L}^{\mathbf{q}} = \mathcal{L}^{\mathbf{q}}_{\Gamma'} + \mathcal{L}^{\mathbf{q}}_{R'} + \mathcal{L}^{\mathbf{q}}_{L'} + \mathcal{L}^{\mathbf{q}}_{X'}, \tag{6.11}$$

where each term on the r.h.s. refers to the point that is specified by the subscript letter.

Now it is easy to recognize that, although the eigenvectors $|w\rangle$ are a complete basis, not all the lattice distortions contribute to the physical effects studied here. Then, we shall perform a second approximation by choosing a subset of modes, $|\{w\}\rangle$, of the conventional unit cell, $|\{w\}\rangle \subset |w\rangle$; this will include: (i) the soft polar mode along the $\hat{r}$ direction, $|O\rangle$, since it is the one that most contribute to the total polarization response [82]; (ii) the oxygen rotations along $\hat{r}$ and $\hat{s}$, since they define the AFD domains, $|\phi_r\rangle$ and $|\phi_s\rangle$; (iii) all three acoustic modes, $|A_\alpha\rangle$, which define the local strain, as we will show in the next paragraph. Note that on one side the modes of point (i) and (iii) belong to the Γ' symmetry, and we will identify them as: $|\tilde{\Gamma}'\rangle = \{|A_\alpha\rangle \oplus |O\rangle\}$; on the other side the oxygen rotations belong to the R' symmetry, and for convenience in we define $|\tilde{R}'\rangle = \{|\phi_r\rangle \oplus |\phi_s\rangle\}$. Then, the subspace $|\{w\}\rangle$ is defined as:

$$|\{w\}\rangle = \{|\tilde{\Gamma}'\rangle \oplus |\tilde{R}'\rangle\}. \tag{6.12}$$

With this approximation applied to Eq. 6.11, the Lagrangian becomes

$$\mathcal{L}^{\mathbf{q}} \approx \mathcal{L}^{\mathbf{q}}_{\tilde{\Gamma}'} + \mathcal{L}^{\mathbf{q}}_{\tilde{R}'}, \tag{6.13}$$

where the two terms on the r.h.s. are containing the contributions from the $|\tilde{\Gamma}'\rangle$ and $|\tilde{R}'\rangle$ modes, respectively.

Finally the microscopic model, which has the aim of reproducing the full *ab initio* results in a neighborhood of Γ, is obtained by plugging the the dynamical matrix expansion, Eq. 6.10, into Eq. 6.9 and retaining only the subset of lattice displacement defined in Eq. 6.12. Note that there is no coupling between the polar and acoustic modes, mediated by the $\hat{D}^{(1,\mathbf{q})}$ matrix, since in the cubic phase of STO each atomic position coincides with a point of center inversion symmetry.

To conclude, we want to stress that the choice of the subspace 6.12, which was postulated using three sensible considerations about the physical problem studied here, must be verified. Indeed we will show in the following that in order to recover an acceptable agreement between the prediction of the present microscopic model and the full DFT results, it is necessary for STO to include explicitly in $|\{w\}\rangle$ another crystal distortion, describing the antiferroelectric (AF) mode of the Ti atoms.

6.2.2 Connections to continuum models

Following Ref. [75], the contact point between the continuum energy functional and the microscopic dynamics is conveniently performed in reciprocal space, where the amplitude of the lattice distortions, $\tilde{v}_k^{\mathbf{q}}$, can be related to the macroscopic order parameters, $v_k(\mathbf{r})$, by the Fourier transform

$$v_k(\mathbf{r}) = \frac{1}{\sqrt{(2\pi)^3}} \int d^3q \, \tilde{v}_k^{\mathbf{q}} e^{i\mathbf{r}\cdot\mathbf{q}}. \tag{6.14}$$

Applying such transform to Lagrangian functions, $\mathcal{L}_{\tilde{\Gamma}'}^{\mathbf{q}}$ and $\mathcal{L}_{\tilde{R}'}^{\mathbf{q}}$, one obtains the following effective energy expressions

$$\begin{aligned} E_{\tilde{\Gamma}'} &= \frac{C_{\alpha\beta,\gamma\delta}}{2}\varepsilon_{\alpha\beta}\varepsilon_{\gamma\delta} + \frac{1}{2\chi_0}P^2 + \frac{G}{2}(\partial P)^2 - fP\partial\varepsilon_{rs} \\ E_{\tilde{R}'} &= \frac{k}{2}|\boldsymbol{\phi}|^2 + \frac{D_i}{2}(\partial\phi_i)^2, \end{aligned} \tag{6.15}$$

which are precisely the harmonic terms of Eq. 6.1. The advantage of the present derivation is that for all the harmonic coupling coefficients we have obtained a microscopic expression, as function of the dynamical matrix.

In order to get the explicit microscopic formulae for each coefficient of Eq. 6.15, one has to assign the correct units to the amplitudes $\tilde{v}_k^{\mathbf{q}}$, to recover the standard

definition of the macroscopic order parameters. For the acoustic case we set

$$U_\alpha^{\mathbf{q}} = \tilde{v}_{A_\alpha}^{\mathbf{q}} \tag{6.16}$$

where $U_\alpha^{\mathbf{q}}$ are the Fourier components of the macroscopic displacement field, $u_\alpha(\mathbf{r})$. Note that Eq. 6.16 holds only if the mass M_A is equal to the total mass of the unit cell [75],

$$M_A = M = \sum_\kappa m_\kappa, \tag{6.17}$$

as one can easily understand by reminding Eq. 6.8. For the soft polar mode, in order to recover the macroscopic polarization, P, one has to set [75]

$$P^{\mathbf{q}} = \frac{Z_{\hat{r}\hat{r}}(\tilde{v}_O^{\mathbf{q}})}{\Omega}, \tag{6.18}$$

where $Z_{\alpha\beta}$ is the effective charge tensor of the soft polar mode; this is defined as

$$Z_{\alpha\beta} = \sum_{\kappa\gamma} Z_{\alpha\gamma}^{\kappa^*} \sqrt{\frac{M}{m_\kappa}} \langle \kappa\gamma | O_\beta \rangle, \tag{6.19}$$

where $Z_{\alpha\gamma}^{\kappa^*}$ is the Born effective charge of each sublattice κ, Eq. 2.53, and $|O_\beta\rangle$ is the soft polar mode in direction β.

Using these choices one recovers the type-I elastic tensor [79],

$$[\alpha\beta, \gamma\delta] = -\frac{M}{2\Omega} \langle A_\alpha | \hat{D}^{(2,\gamma\delta)} | A_\beta \rangle, \tag{6.20}$$

which is define in Appendix A, Eq. A.12. This is connected to the familiar (type-II) elastic tensor, $C_{\alpha\beta,\gamma\delta}$, by Eq. A.16. In a similar way, one obtains

$$\begin{aligned} (\chi_0)^{-1} &= \frac{M}{\Omega} (Z)_{\hat{r}\gamma}^{-1} \langle O_\gamma | \hat{D}^{(0)} | O_\gamma \rangle (Z)_{\hat{r}\gamma}^{-1} \\ G &= -\frac{M}{2\Omega} (Z)_{\hat{r}\rho}^{-1} \langle O_\rho | \hat{D}^{(2,\hat{s}\hat{s})} | O_\omega \rangle (Z)_{\hat{r}\omega}^{-1} \\ f &= \frac{M}{4\Omega} (Z)_{\hat{r}\rho}^{-1} \langle O_\rho | \hat{D}^{(2,\hat{s}\hat{s})} | A_{\hat{r}} \rangle. \end{aligned} \tag{6.21}$$

We now move to the AFD energy, $E_{\tilde{R}'}$. Generally speaking, since the oxygen rotations are small (in the bulk AFD phase of STO the rotations are $\sim 2^\circ$), it is convenient to express ϕ_i as the displacement of the rotated oxygen atoms projected on its own cube face, in length units [11]. This choice sets the amplitudes $\tilde{v}_{\phi_i}^{\mathbf{q}}$ equal to the Fourier components of the continuum parameter ϕ_i, and fix once and for all

the value M_ϕ to be

$$M_\phi = 2m_O, \tag{6.22}$$

where m_O is the oxygen mass. [Note that the relation 6.22 holds specifically when the conventional tetragonal cell of twenty atoms is used.] With this choice, the coefficients in $E_{\tilde{R}'}$, can be calculated as follows

$$\begin{aligned} \kappa &= \frac{2m_O}{\Omega}\langle\phi_i|\hat{D}^{(0)}|\phi_i\rangle \\ D_i &= -\frac{2m_O}{\Omega}\langle\phi_i|\hat{D}^{(2,\hat{s}\hat{s})}|\phi_i\rangle. \end{aligned} \tag{6.23}$$

6.2.3 Anhamronic couplings

Up to here we have developed an harmonic model. However, anharmonic couplings are essential to describe the energy landscape that includes the AFD crystal phase. Moreover, in the case of STO a polar response can only be triggered through anharmonic couplings between the polarization and the other order parameters. Indeed, in previous studies [71] great emphasis was given to the biquadratic coupling, since it directly connects the polarization and the oxygen rotations, which drive the phase transition to the AFD phase. Note that in general anharmonic terms can mix distortions that belongs to different Brillouin points, lifting the prescription that the $\tilde{\Gamma}'$ and $\tilde{R}'$ modes can not couple.

Using the previously identified order parameters (i.e. the strain, $\varepsilon_{\alpha\beta}$, the polarization, P, and the oxygen rotations, ϕ_i), in the case of STO one see that the homogeneous anharmonic terms allowed by symmetry are exactly the ones appearing in Eq. 6.1,

$$E_{anh} = A|\boldsymbol{\phi}|^4 - e_\alpha\varepsilon_{\alpha\alpha}P^2 - R_{ij\alpha\beta}\phi_i\phi_j\varepsilon_{\alpha\beta} - Q_i\phi_i^2P^2. \tag{6.24}$$

Since they are all function of common homogeneous parameters, they can be easily calculated by first principles, via a series of finite-difference calculations of total energies related to crystal structure, in which the different order parameters have been froze-in. Example of such calculations can be fund in literature [40, 60, 93], included a specific study on the combined effects of strain and oxygen rotation for an homogeneous phase of STO [66].

6.3 New coupling terms

In this section we will discuss additional couplings that have been taken intro account in the present 1D effective model for the ferroelastic DWs of STO. The are

named "new" because, to our knowledge, their explicit inclusion into effective energy models based on first-principles calculations was never reported before.

In the first paragraph we will present an extra gradient-mediated anharmonic coupling, and the strategy in which it can be calculated by fist principles, using the methodology presented before. In the second paragraph instead we will discuss the new terms that must be added to the effective model as consequence of including the AF mode of the Ti atoms as an explicit parameter.

6.3.1 Rotopolar coupling

Here we are interested in perform a systematic study of all the possible mechanisms that can induce a polar response at the TWs of STO. In particular, we shall include all the relevant gradient mediated couplings; based on symmetry considerationsone can show that exist an extra tri-linear coupling that can not be discarded a priori: the rotopolar coupling. This directly connects the polarization and the gradient of the oxygen rotations, and in the case of our geometry it is

$$E_{rot} = W_{ij} P \phi_j \partial \phi_i. \tag{6.25}$$

Note that W_{ij} bears some similarities to the "flexoantiferrodis-tortive" (FxAFD) coupling described in Ref. [20]; however, at difference with FxAFD, the rotopolar coupling have two different values for W_{rs} and W_{sr}, i.e. it is not symmetric under permutation of the two indices.

The first principles calculation of the coupling coefficients W_{ij} presents two difficulties: this is a tri-linear coupling and it involves inhomogeneous terms. Ideally, the inhomogeneous issue can be solved by using a long wave expansion, as done before with the dynamical matrix, applied now to the Fourier components of the third derivative of the lattice energy variation respect to the atomic displacements,

$$N^{ll'l''}_{\kappa\alpha,\kappa'\beta,\kappa''\gamma} = \frac{\partial^3 E}{\partial u^{l}_{\kappa\alpha} \partial u^{l'}_{\kappa'\beta} \partial u^{l''}_{\kappa''\gamma}}. \tag{6.26}$$

However, this tensor is not directly accessible within standard DFPT codes. Here, to overcome this difficulty we have calculated the elements of Eq. 6.26 by performing one of the three lattice derivatives by finite difference. In practice, one can rewrite the previous quantity as

$$N^{\mathbf{q}}_{\kappa\alpha,\kappa'\beta,\kappa''\gamma} = \frac{\Delta\Phi^{\mathbf{q}}_{\kappa\alpha,\kappa'\beta}(u_{\kappa''\gamma})}{\lambda}, \tag{6.27}$$

where $\Delta\Phi^{\mathbf{q}}_{\kappa\alpha,\kappa'\beta}(u_{\kappa''\gamma}) = \left(\Phi^{\mathbf{q}}_{\kappa\alpha,\kappa'\beta}(u^{\mathbf{q}}_{\kappa''\gamma}) - \Phi^{\mathbf{q}}_{\kappa\alpha,\kappa'\beta}\right)$, and $\Phi^{\mathbf{q}}_{\kappa\alpha,\kappa'\beta}(u_{\kappa''\gamma})$ is the dynamical matrix related to the reference crystal structure where the κ'' atom is displaced of a λ amount in direction γ. For the present discussion it is more convenient to work directly with collective atomic displacements associated to the lattice distortions of Eq. 6.12. Then, proceeding as before, after the long wave expansion of the the $N^{\mathbf{q}}_{\kappa\alpha,\kappa'\beta,\kappa''\gamma}$ tensor one can obtain the following expression for the rotopolar coupling:

$$W_{ij} = i\frac{\sqrt{2m_O M}}{2\Omega}\frac{\langle P|\Delta\hat{D}^{(1,\hat{s})}(\phi_j)|\phi_i\rangle}{\lambda} \tag{6.28}$$

where $\Delta\hat{D}^{(1,\hat{s})}(\phi_j)$ is it the first term of the long wave expansion applied to the dynamical matrix related to the conventional tetragonal cell with the oxygen atoms distorted of a λ amount according to the mode $|\phi_j\rangle$ (more details on the practical calculation of all the coefficients can be found in the following Sec. 6.4).

6.3.2 Anti-ferroelectric mode of the Ti atoms

Choosing the subspace $|\{w\}\rangle$ is always a delicate step because one can accidentally omit lattice distortions that are essential to establish a physically correct continuum model. Therefore it is always necessary to go trough a verification of such choice, by comparing the model outcomes with full DFT results. We will discuss the practical side of this testing procedure in Sec. 6.4.1, where the results for the STO case are presented. The major outcome of such testing procedure is that the displacements defined in Eq. 6.12 alone fail to correctly describe the phonon dispersion associated to the ϕ_r distortion (this is shown in Fig.6.2). In order to improve this dispersion, which ultimately is related to the inhomogeneous effects of ϕ_r, it is reasonable to look for all the extra displacements that couple with $|\phi_r\rangle$.

Due to symmetry constrains [20, 66], it turns out that, at the lowest order in a long wave expansion, only the anti-ferroelectric (AF) displacements of the Ti atoms, $|\mathrm{AF}_{Ti_\alpha}\rangle$, couple with the AFD modes. $|\mathrm{AF}_{Ti_\alpha}\rangle$ belong to the R' set of displacements, and at the harmonic level the most general expression for its coupling with $|\phi_\beta\rangle$ is

$$-\frac{i}{2}\epsilon_{\alpha\beta\gamma}\sqrt{M_{AF_{Ti_\alpha}}M_{\phi_\beta}}\langle \mathrm{AF}_{Ti_\alpha}|D^{(1,\gamma)}|\phi_\beta\rangle, \tag{6.29}$$

where $\epsilon_{\alpha\beta\gamma}$ is the Levi-Civita symbol. Note that this is a gradient mediated term, since the first $\mathbf{q}$-derivative of the dynamical matrix appears.

In the specific case of the 1D model for ferroelastic DWs in STO, only the AF mode in direction $\hat{x}$ is involved, and it precisely couples with ϕ_r. To incorporate

explicitly the effects of the AF mode, we have redefined the subset of lattice displacements, $|\tilde{R}'\rangle$, by adding $|\mathrm{AF}_{Ti_x}\rangle$:

$$|\tilde{R}'\rangle \rightarrow \{|\phi_r\rangle \oplus |\phi_s\rangle \oplus |AF_{Ti}\rangle\}, \tag{6.30}$$

where from now on we will omitted the redundant subscript x from the AF mode. By exploring other couplings that can be triggered by the explicit treatment of the AF mode, one finds that exists another tri-linear contribution to the polarization, induced by the AFD mode along the s direction, which we will call N. In conclusion, the extra terms that we have included in our effective model for STO are

$$E_{\mathrm{Ti}} = \frac{\kappa^{Ti}}{2}\left(u^{Ti}\right)^2 + SP(\partial\phi_r) + NPu^{Ti}\phi_s, \tag{6.31}$$

where u^{Ti} is the macroscopic order parameters describing the AF distortion of the Ti atoms, and each coefficient can be written in terms of microscopic quantities as

$$\begin{aligned}
\kappa^{Ti} =& \frac{M_{Ti}}{\Omega}\langle \mathrm{AF}_{Ti}|\hat{D}^{(0)}|\mathrm{AF}_{Ti}\rangle \\
S =& -\frac{i}{2}\sqrt{2m_O M_{Ti}}\langle \mathrm{AF}_{Ti}|D^{(1,\hat{s})}|\phi_r\rangle \\
N =& \frac{\sqrt{2m_{Ti}M}}{2\Omega}\frac{\Delta\langle P|\hat{D}^{(0)}(\phi_r)|\mathrm{AF}_{Ti}\rangle}{\lambda}.
\end{aligned} \tag{6.32}$$

As before, the factor M_{Ti} is arbitrary, and it is fixed by choosing the physical units for the continuum parameter, u^{Ti}. The most natural choice are length units, which sets

$$M_{Ti} = 2m_{Ti}, \tag{6.33}$$

where m_{Ti} is the mass of the Ti atoms. [Note that Eq. 6.33 is valid for the specific case of the conventional tetragonal cell.]

6.4 Continuum model for STO

For the ferroeleastic DWs of STO, summing up all the results of the previous sections, one get the following 1D model:

$$\begin{aligned} E =& \frac{C_{\alpha\beta,\gamma\delta}}{2}\varepsilon_{\alpha\beta}\varepsilon_{\gamma\delta} + \frac{\kappa}{2}|\boldsymbol{\phi}|^2 + A|\boldsymbol{\phi}|^4 + \frac{\chi_0^{-1}}{2}P^2 \\ & - R_{i\alpha}\phi_i^2\varepsilon_{\alpha\alpha} - Q_i\phi_i^2P^2 - e_\alpha P^2\varepsilon_{\alpha\alpha} \\ & + \frac{D_i}{2}(\partial\phi_i)^2 + \frac{G}{2}(\partial P)^2 - fP\partial\varepsilon_{rs} - W_{ij}P(\partial\phi_i)\phi_j \\ & + \frac{\kappa^{\mathrm{Ti}}}{2}(u^{\mathrm{Ti}})^2 + NPu^{\mathrm{Ti}}\phi_s + S(\partial\phi_r)u^{\mathrm{Ti}}, \end{aligned} \tag{6.34}$$

where the Latin index run over $\{\hat{r},\hat{s}\}$ while the Greek index dun over $\{\hat{r},\hat{s},\hat{x}\}$. Although it is similar to the phenomenological expression 6.1, this model 6.34 has been derived staring from full *ab initio* results, and via two well controlled approximations: (i) the long wave expansion of the dynamical matrix, Eq. 6.10; (ii) the selection of an explicit subspace of lattice distortion , Eq. 6.30;

This allows, on one side, to systematically identify and include in our effective model all the coefficients that fall inside the well defined boundaries of the approximations. On the other side, we have obtained an explicit microscopic formula to calculate each coupling appearing in Eq. 6.34, including the gradient mediated terms. Then all those coefficients can be readily extracted by performing a bunch of DFTP calculations, and projecting the long wave dynamical matrix expansion on the selected set of lattice displacements.

In practice the most tricky part is to get the dynamical matrix expansion itself. We shall calculate the $\mathbf{q}$-derivatives of $\hat{\mathbf{D}}^{\mathbf{q}}_{\kappa\kappa'}$ by using the real space moments of the dynamical matrix,

$$\hat{\mathbf{D}}^{(n,\hat{\mathbf{q}})}_{\kappa\kappa'} = \sum_l \frac{\boldsymbol{\Phi}^l_{\kappa,\kappa'}}{\sqrt{m_\kappa m_{\kappa'}}}\,[\hat{\mathbf{q}}\cdot(\mathbf{R}_l+\boldsymbol{\tau}_\kappa-\boldsymbol{\tau}_{\kappa'})]^n\, e^{i\mathbf{q}\cdot(\mathbf{R}_l+\boldsymbol{\tau}_\kappa-\boldsymbol{\tau}_{\kappa'})}, \tag{6.35}$$

where $\boldsymbol{\tau}_\kappa$ are the undistorted position of the sublattices in the conventional tetragonal cell. $\boldsymbol{\Phi}^l_{\kappa,\kappa'}$ can be derived by performing DFPT calculations for a strip of $\mathbf{q}$-points along the direction $\hat{\mathbf{q}}$, followed by a Fourier transform. Since we have expressed the anharmonic terms as function of the dynamical matrix of a distorted structure, see Eq. 6.27, then the same procedure to calculate its $\mathbf{q}$-derivatives holds also for the anharmonic couplings, with the only difference that now the DFPT caluculation must be performed using the distorted structure where one of the lattice distortion has been frozen-in. For example, in the case of the rotopolar coupling W_{sr}, we have

built a crystal structure with the oxygen atoms rotated along the $\hat{r}$ direction, by a λ amount, and the related force constant matrix projected on the polar mode and $|\phi_s\rangle$ shall give W_{sr}, as prescribed by Eq. 6.28.

The final list of values for each coefficient in Eq. 6.34 is reported in Tab. 6.1.

Details on the *Ab initio* calculations The *ab initio* calculations have been performed with norm-conserving pseudopotentials, taking into account explicitly 10

	US	SV	this work		a.u.	
κ	-3.01	-22.5	-20.62	10^{-6}	Ha	bohr^{-5}
A	5.16	4.92	5.26	10^{-5}	Ha	bohr^{-7}
C_{11}	11.43	13.02	13.14	10^{-3}	Ha	bohr^{-3}
C_{12}	3.64	3.30	3.83	10^{-3}	Ha	bohr^{-3}
C_{44}	4.32		4.16	10^{-3}	Ha	bohr^{-3}
R_{11}	1.23	1.68	1.95	10^{-4}	Ha	bohr^{-5}
R_{12}	-2.37	-2.70	-2.74	10^{-4}	Ha	bohr^{-5}
R_{44}	-2.18		-2.42	10^{-4}	Ha	bohr^{-5}
Q_r			-0.28	10^{-1}	Ha	bohr^{-1}
Q_s			-1.95	10^{-1}	Ha	bohr^{-1}
N			-1.53	10^{-2}	Ha	bohr^{-3}
χ_0			120.00		Ha	bohr
κ^{Ti}			3.54	10^{-3}	Ha	bohr^{-5}
D_r			1.95	10^{-3}	Ha	bohr^{-3}
D_s			1.00	10^{-3}	Ha	bohr^{-3}
S			1.29	10^{-3}	Ha	bohr^{-4}
e_x			-0.18		Ha	bohr
e_s			1.31		Ha	bohr
e_r			1.84		Ha	bohr
G			5.43		Ha	bohr^3
f			-4.70	10^{-2}	Ha	
W_{rs}			2.11	10^{-3}	Ha	bohr^{-2}
W_{sr}			0.29	10^{-3}	Ha	bohr^{-2}

TABLE 6.1: Calculated model parameters compared with the available literature data (US=Uwe and Sakudo [84], SV=Sai and Vanderbilt [66]). The elastic and rotostriction coefficients are repoted in the more common Voigt notation for the Cartesian axis The calculated value of κ is reported in italics, as we have replaced it with a phenomenological function of temperature, Eq. 6.36. Note that the χ_0 value calculated within the zero-temperature first-principles calculations, matches with the experimental value of the dielectric constant at $T \sim 80$ K [88]; $4\pi\chi_0 \sim 1500$.

electrons for Sr, 12 for Ti and 6 for O. The pseudopotentials have been generated using the FHI98PP code and the exchange-correlation term has been treated using the local-density approximation (LDA). Finally the energy cut-off used is 70 Ha and in all the first-principles simulations we have employed a Monkhorst-Pack mesh equivalent to 8x8x8 grid in the primitive cubic cell. With these input parameters we obtain a bulk lattice constant value for the cubic structure of 7.2675 bohr.

The coefficient κ needs a deeper discussion. The values reported in Tab. 6.1 was calculated with DFT simulations. However it is well known that DFT systematically overestimate κ [66], and ultimately inducing an higher AFD value at $T = 0$ K than the experimental findings. This is due to the fact that κ is connected to the frequency of soft AFD phonon modes which are highly sensitive to the pseudopotential approximation.

Actually, in a Landau theory picture, the quadratic coupling of the unstable order parameter is the only one that shows an explicit dependence of the temperature, changing from a positive to a negative value as moving across the transition temperature. Following this reasoning, for obtaining the results presented in the section below, we will replace the DFT value of κ with a function that linearly change respect to the temperature:

$$\kappa(T) = \alpha_0(T - T_\phi), \tag{6.36}$$

where T_ϕ is the transition temperature from the cubic to the AFD phase in STO, $T_\phi = 105$ K, and α_0 is the linear coefficient chosen in order to recover the experimental value of $\phi_{AFD} = 2.1^\circ$ at $T = 0$ K [16], which means $\alpha_0 = 0.047 \cdot 10^{-6}$ Hartree/bohr^2.

6.4.1 Validating the macroscopic model

Testing the microscopic model is crucial in order to check the accuracy of the effective energy expansion. In practice, the aim here is to verify that the chosen subspace of normal modes at the Γ point, $|\{w\}\rangle$, is sufficient to reproduce all the relevant physical effects in which we are interested here. For simplicity here we will only focus on the harmonic terms; then the macroscopic model is given by the sum of $E_{\tilde{\Gamma}'}$, $E_{\tilde{R}'}$ and the harmonic terms of E_{Ti}, Eq.s 6.15 and 6.31. Since the initial goal as to build an approximation for the phonon dispersions of selected normal-modes, $|\{w\}\rangle$, in an neighborhood of Γ, then we will directly compare the phonon dispersion curves obtained using full *ab initio* calculations to those provided by the macroscopic model.

In fig. 6.2 we report the phonon dispersion curves associated to the normal modes of the 1D model for STO. In panel (a) the dispersion of the three acoustic modes and the soft polar mode are shown. The solid lines are the full DFT results (the ticker solid lines highlight the transverse branches that are the relevant for the present 1D model), while the dot-dashed blue lines represent the results of the macroscopic harmonic model. Fig. 6.2 illustrates that the model describes the phonon dispersion associated to the transverse acoustic mode and transverse polar mode to a good approximation. This gives us the confidence that the spatial gradients of ε_{rs} and P are correctly treated. In the same panel the red dashed lines are the results of a modified macroscopic model where we remove the flexocoupling between the optical and acoustic branches, f. Clearly, the acoustic (red) branch shows a worse agreement with respect to the DFT result, corroborating the idea that the flexoelectric coupling has an important role in spatially inhomogeneous systems.

In panel (b), the phonon dispersions associated to the oxygen octahedron rotations ϕ_s and ϕ_r are shown. Again the black thick lines are the full DFT results, while the blue dashed lines are calculated using our model.

This test was extremely important in order to identify the importance of the AF mode of the Ti atoms on the ϕ_r dispersion. Indeed, in the same panel (b), we show (light blue dashed line) the results of the macroscopic model without including the S coupling, i.e. the result as simply obtained by $E_{\tilde{R}'}$ in Eq. 6.15. It is clear that the agreement with the DFT line is poor, and the Ti mode plays an important role in the modulated tilt patterns.

In conclusions the testing procedure is an essential step that gives a quite important indication on the degree of reliability of the macroscopic model, and ultimately of the continuum effective expansion that is build on top of it. Moreover the testing procedure can unveil new couplings that can introduce new physical effects, as it is the case here with the AF mode of the Ti atoms.

6.5 Twin walls in STO

6.5.1 Details on the solution of the continuum model

Here we present the details on the conjugate gradient minimization of Eq.6.34. The continuum fields have been discretized to a one dimensional mesh along the direction $\hat{s}$, and the spacing has been set equal to $a_{[110]} = a_0/\sqrt{2}$, where a_0 is the equilibrium lattice parameter of STO as calculated from first principles. Thus, the mesh coincides with the atomic layers of the Sr atoms along the [110] direction.

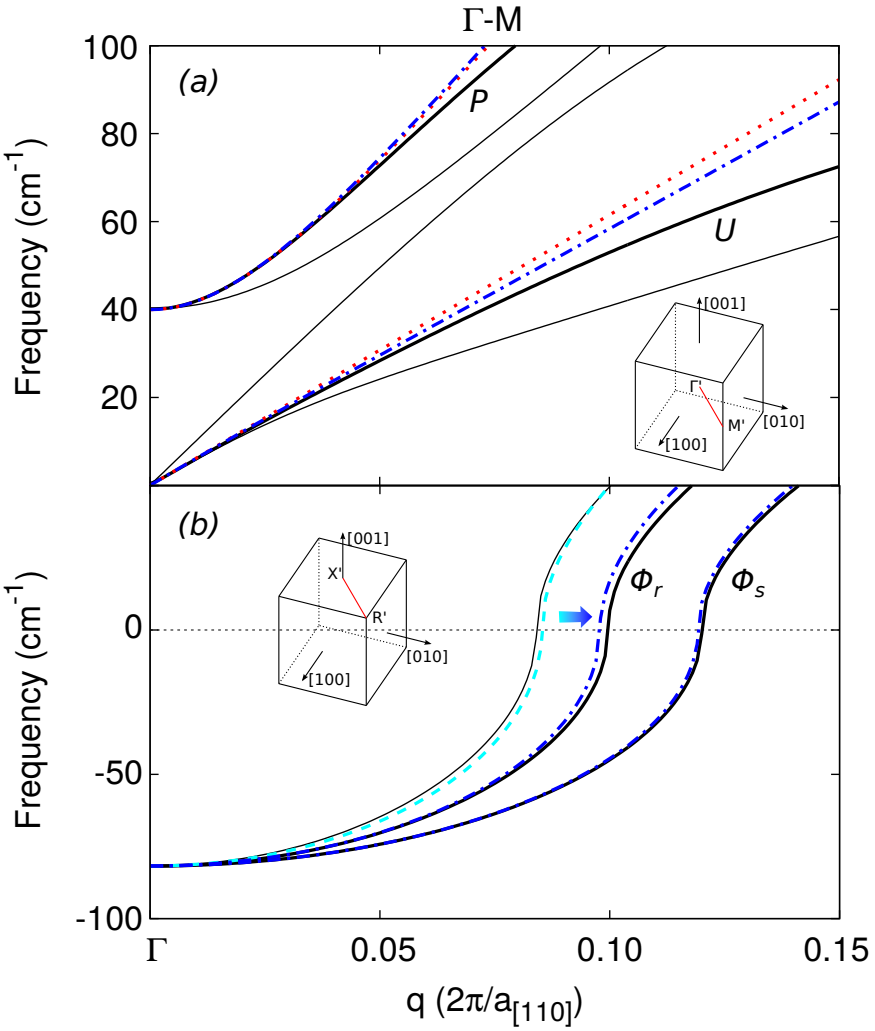

FIGURE 6.2: Phonon frequencies as function of the wavevector q in reduced coordinates, where $a_{[110]} = a_0\sqrt{2}$ and a_0 is the cubic lattice parameter of STO. In panel (a) the phonon dispersions are plotted along the Γ-M direction, adn in panel (b) along the R'-X' (see inset). Solid curves are first-principles data, while dashed and dot-dashed are the results of the model (see text).

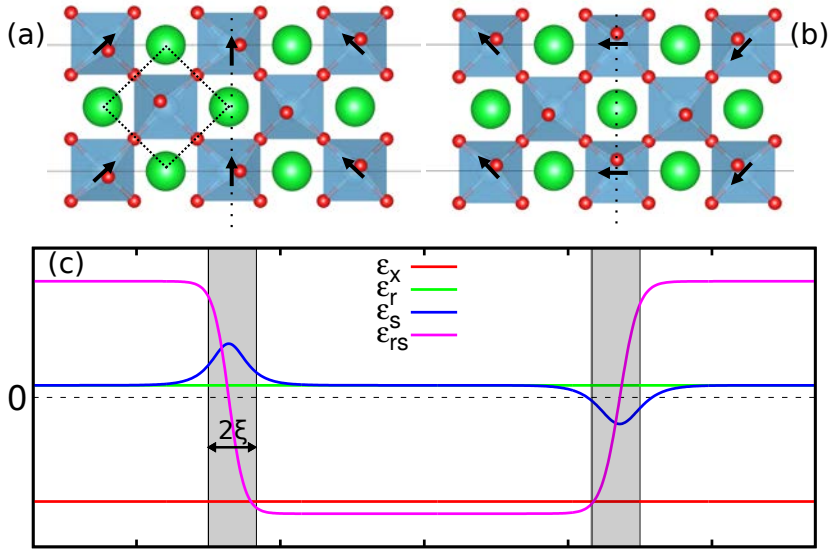

FIGURE 6.3: Evolution of the strain across the ferroelastic twin walls. (a) and (b): illustrations of the two types of ferroelastic twin walls considered in this work (respectively HH and HT). Note that these are just schematic illustrations of how the order parameter evolves from one domain to the next - as discussed in the main text, the actual length scale of the transition is much larger than suggested by the cartoons. (c): Evolution of the individual strain components across the two DWs. Note that ε_{rr} and $\varepsilon_x x$ are uniform and fixed to their bulk value, in order to reproduce the correct mechanical boundary conditions for the domain wall structure.

The gradients of a given continuum field, f, are expressed as effective nearest-neighbor interactions between the mesh points. This is equivalent to adopting the following finite-difference formula:

$$\partial f_{i+1} = \frac{f_{i+2} - f_i}{2a_{[110]}} \tag{6.37}$$

where the subscript indicates the mesh point at which the field (or its gradient) is sampled.

Periodic boundary conditions have been enforced; as consequence, the simulated geometries always involve supercells that include at least two equal and oppositely oriented twin walls. For example, in order to study a H-T DW, the supercell includes an H-T and a T-H boundary, or to study a H-H one has to include an H-H and T-T boundary. To avoid interactions between the two DWs, a supercell size of $300\, a_{[110]}$ has been set.

The relaxation of the strain components must be performed with care, in order to respect the mechanical compatibility conditions of the problem. Indeed, the ferroelastic DWs must preserve translational symmetry along the $\hat{r}$ and $\hat{x}$ direction. Therefore, the transverse strain components (referring to the DWs orientation) ε_{rr} and ε_{xx} must be uniform throughout the structure. Their values have been fixed to the respective equilibrium bulk values of the distorted tetragonal phase. Conversely, ε_{ss} and ε_{rs} are free to relax during the energy minimization, in order to fit the local distortion that occur in a neighborhood of the ferroelastic TWs.

As an example, the starting conditions for simulating an H-H configuration consist in setting the ϕ_s parameter to a sinusoidal profile with period to the supercell length and ϕ_r to a constant value. Then the minimization procedure will give the result shown in Fig.s 6.3, where profiles of the strain components across the supercell are shown. Note that if the supercell is too small, then it is energetically convenient for the system restore a unique uniform AFD phase, since the dispersion coefficients, G carry the main contribution to the energy. However, a supercell length of $600\, a_{[110]}$ is more than enough to obtain two well separated TWs at 80 K.

6.5.2 Thickness and energy

In Fig.6.4 we show the relaxed structural order parameter profile for the two types of DW. Note that, the AFD component that changes sign across the DWs show an antisymmetric profile with respect to $s \to -s$. The analytic solution (with some simplifications) [11, 68] is proportional to $\tanh(s/\xi)$, where 2ξ is defined as the DW thickness. The present model matches fairly well such trend; then, we used

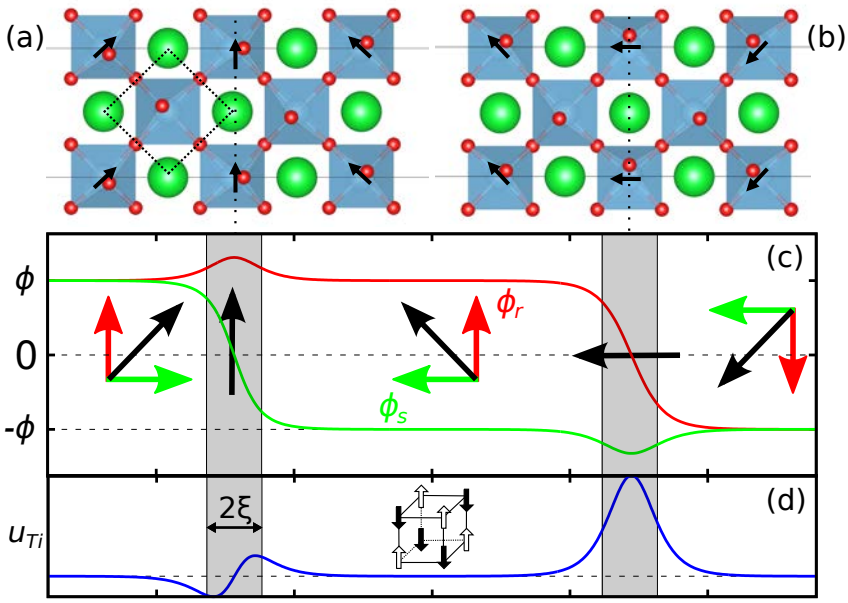

FIGURE 6.4: (a),(b) Schematic illustration (not to scale) of the two different types of TBs considered in this work, respectively HH (a) and HT (b). Sr (large green balls), O (small red balls), and the oxygen octahedra are shown; the dashed square indicates the primitive cell of the cubic reference phase; the arrows indicate the local tilt vector. (c) Evolution of ϕ_s and ϕ_r across the two TBs. A local decomposition of the tilt vector (black arrows) into $\hat{s}$ (green) and $\hat{r}$ (red) is also shown. The shaded area indicates the nominal wall thickness 2ξ. (d) Amplitude of the u^{Ti} mode in arbitrary units. The inset illustrates the AFE character of the Ti displacements, resembling spins in a G-type antiferromagnet. The length scale is in units of ξ.

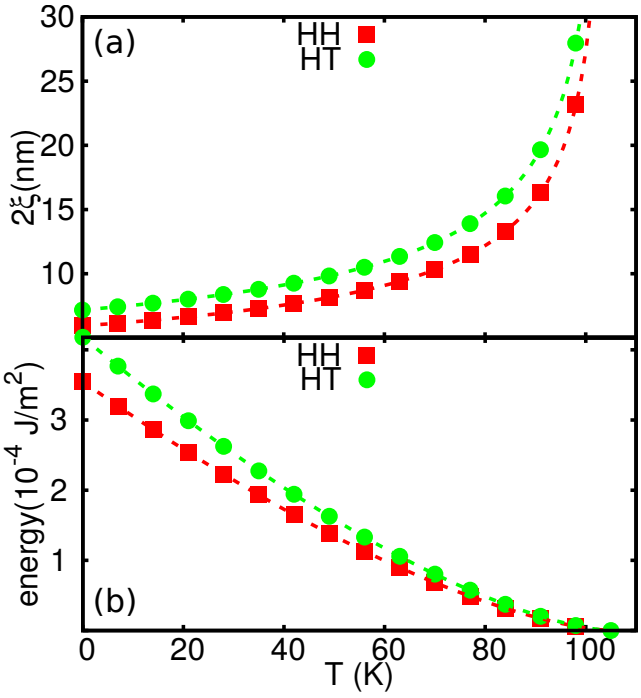

FIGURE 6.5: (a) Domain wall thickness 2ξ as a function of temperature. (b) Formation energy per surface unit as a function of temperature.

a fit to $\tanh(s/\xi)$ to extract the DW's thickness. On the other hand, the constant component of the AFD mode across the DW shows a characteristic bump in correspondence of the boundary. Again, this is in agreement with earlier analytical works [11]. The presence of a bump on the inversion-symmetric AFD component is due to the fact that the system tries to preserve a constant amplitude for the oxygen tilt pseudovector.

A study on the DWs' thickness as function of temperature is reported in Fig. 6.5. As we mentioned earlier, the temperature has been introduced into the continuum model by varying the κ coefficient according to the Curie-Weiss law, Eq. 6.36.

In Fig. 6.5 we plot the DW width. Interestingly, for a temperature around 80 K, we get widths that are $2\xi \sim 11 - 14$ nm, which is almost one order of magnitude thicker than the established literature values for either $SrTiO_3$ [11, 55] or other ferroelastic materials [68]. This discrepancy can be traced back to the D_i gradient coefficients. The values calculated here from first principles are much larger than

the values commonly used in literature [11]. Moreover HT thickness is always bigger than in the HH case because the gradient coupling D_{ss} is smaller than D_{rs}. We remind that here all the gradient-mediated coefficients have been calculated on the base of phonon band dispersions, for which DFT is known to have an excellent degree of accuracy.

The thickness of the DWs predicted by the present model fits with the experimental observation that they are highly mobile, even at the lowest temperatures [41]. Moreover, in retrospect, this result also justifies the continuum approximation employed in this Chapter, instead of a direct DFT study that would be computationally inaccessible.

Another important quantity that characterizes the ferroelastic DWs' formation is the formation energy. Comparing the relative formation energy between the two types of DWs, Fig. 6.5, another surprise emerges: the HT walls, which were formerly believed [55] to be the "easy" type of twin boundaries, are in fact more costly than HH walls. Again, this can be traced back to the gradient coefficients D_i.

Finally, it is interesting to note that the expected [11] scaling of the thickness, 2ξ, and energy, E, as a function of κ and the D_i coefficients are accurately respected by our results: $\xi_i \sim \sqrt{D_i/\kappa}$ and $E_i \sim \kappa^2\sqrt{D_i/\kappa}$.

6.5.3 Domain wall polarity

We move now to the main result of this work, regarding the induced electrical polarization at either type of domain boundary. For the following results, we shall work at a reference temperature of $T_{\text{ref}} = 80$ K. which is chosen out of convenience. Indeed also the χ_0 parameter shows a temperature dependence [88]; however DFT calculations, which are formally performed at 0 K, usually overestimate such coefficient. Here, the calculated value of χ_0 matches the experimentally measured [88] dielectric constant of $SrTiO_3$ precisely at 80 K. Therefore, in order to be consistent in the following results we will restrict our analysis to T_{ref}. It is important to stress that the main conclusions that will be presented in the following are, nevertheless, valid at any temperature below the ferroelastic transition.

Looking back at the effective energy, Eq. (6.34), one can see that there are three *improper* (linear in P) mechanisms that can induce a polarization at the wall: flexoelectricity, rotopolar copuling, and the trilinear coupling mediated by u^{Ti}. In order to quantitatively appreciate the impact of each one of these mechanisms, we analyze them by introducing one by one. We shall start with an Hamiltonian where W_{ij}, S and N are artificially set to zero; then progressively they are switched on and at the same time their impact on the total (integrated) polarization at either

wall ($\langle P\rangle_{\mathrm{HH,HT}}$) is monitored. As example a profile of the macroscopic polarization, $P(s)$, at the two DWs is reported in Fig.6.6. Note that the electrostriction and biquadratic couplings also have an impact on $\langle P\rangle$, although they fall in a different category since they both go like P^2. Therefore, in order to quantify their importance, we shall perform the computational calculations twice, either with or without the latter two terms (see the difference between full and empty circles in Fig. 6.6).

The total integrated polarization for both the TWs is reported in Fig. 6.6. The A points are the results for the simplest artificial case ($W_{ij} = S = N = 0$), showing that the polarity of HH and HT walls is essentially the same. This is understood by the fact that the flexoelectric contribution acting on $\langle P\rangle$, which is the only mechanism of order P at play here, can only depend [70] on the total discontinuity in the shear strain component, $\Delta\varepsilon_{rs}$, and this is the same at both types of walls. Then, the small difference between $\langle P\rangle_{HH}$ and $\langle P\rangle_{HT}$ is only due to the P^2 terms, i.e. the electrostriction and biquadratic couplings.

In retrospect, we have also got the important result that the P^2 contributions to the total polarization are much less remarkable that the flexoelectric coupling.

Next, by switching on the new rotopolar coupling, W_{ij}, we get the results B. This mechanism introduce a great difference on the total polarization between the two TWs. Indeed its contribution to $\langle P\rangle$ is dominated by W_{rs} at HT walls, and by W_{sr} at the HH walls. Since W_{sr} is very small 6.1, at HH walls the polarization is almost unaffected; conversely, W_{rs} is large and almost cancels the flexoelectric effect at HT walls.

If the analysis was stopped, then one would be forced to conclude that the total polarization at the HH ferroelastic DW is bigger than the HT case, $\langle P\rangle_{\mathrm{HH}} > \langle P\rangle_{\mathrm{HT}}$. However the procedure to built an effective model, starting from the microscopic DFT results has already proved the importance of introducing the u^{Ti} order parameter. This couple via a trilinear coupling with P and the AFD tilts. Then, turning on the N coupling has a dramatic impact on $\langle P\rangle$, to the point that it reverses (C point) the ordering of $\langle P\rangle_{\mathrm{HH}}$ and $\langle P\rangle_{\mathrm{HT}}$ The trilinear coupling can be thought as an effective additional contribution to W_{rs}, while its contribution to W_{sr} vanishes. Therefore the most affected wall type is the HT, where ϕ_r changes sign. This explains why u^{Ti} has a much larger amplitude at the HT wall, Fig. 5.1.

By looking at the empty circles of Fig. 5.1, calculated by excluding the biquadratic / electrostrictive couplings, one concludes that the effects of these couplings are a systematic suppression, somewhat stronger at the HH walls, of the gradient-induced polarization. This observation implies that the P^2 terms alone are unlikely to trigger a ferroelectric state at either type of twin boundary, and corroborates improper mechanisms as the main driving force for P.

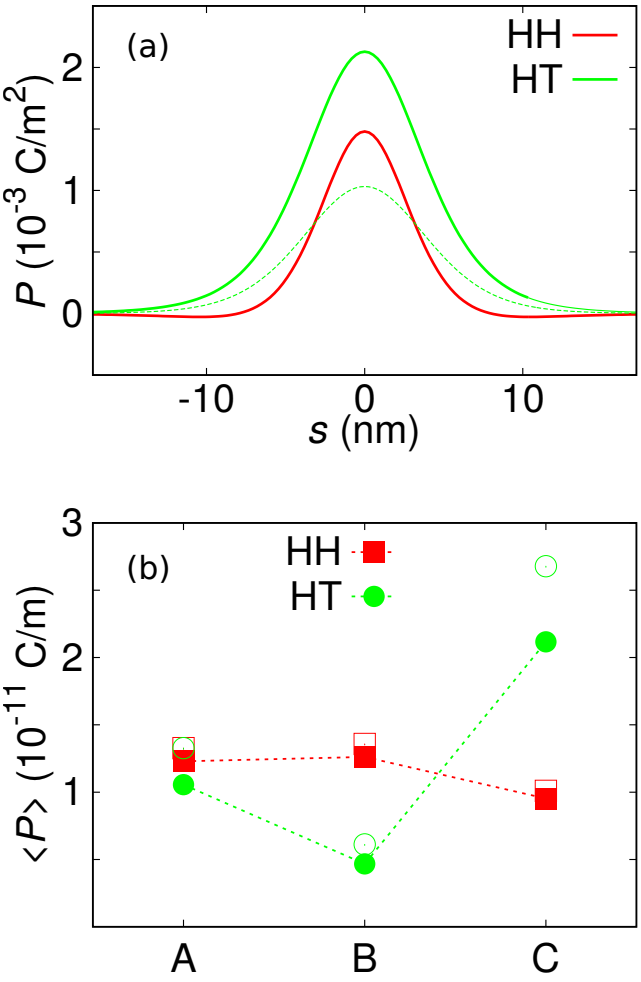

FIGURE 6.6: (a) Polarization profile across the two DWs; the dashed line refers to the result B, i.e., without including u^{Ti} in the simulation. (b): Total polarization integrated across the DW as a function of the addition of different couplings in the Hamiltonian. The empty and filled symbols refer to the results obtained while excluding or including the biquadratic and electrostrictive terms. The polarization vector is always oriented towards the apex of the twin boundary.

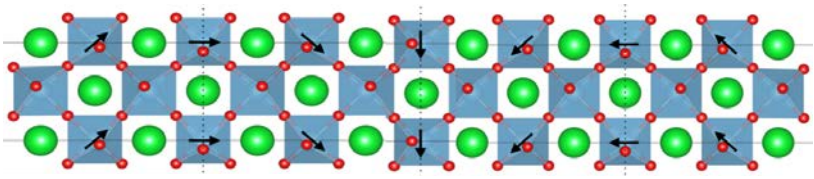

FIGURE 6.7: An AFD cycloid.

6.5.4 Conclusions

As result of our analysis, we have obtained that the two different types of ferroelastic DWs in STO have a polar character, and the total polarization at the two walls is different. In particular we have identified two main causes that induce a different polar response between the HH and HT configuration: the rotopolar coupling and the activation of the AF mode.

Interestingly, if in the former we take replace $\boldsymbol{\phi}$ with the magnetization vector ($\mathbf{M}$), we obtain the Lifshitz invariant already discussed in the context of inhomogeneous magnetic materials, Ref. [56], where it was suggested that spin cycloids can induce a macroscopic polarization response. Similarly, by engineering the ferroeleastic domain walls in STO, one could induce a *macroscopic* ferrielectric-like polarization, P_{mac}, in a periodic twin wall structure. It suffices to alternate HT and HH wall types, as illustrated in Fig. 6.7, to obtain (L is the average domain width) $P_{\text{mac}} = (\langle P \rangle_{\text{HH}} - \langle P \rangle_{\text{HT}})/(2L) \neq 0$. This result can be easily understood even without doing the calculations. There is an insightful visual proof that such a structure indeed does break macroscopic inversion symmetry: By following the evolution of the AFD pseudovector across the structure, one can easily identify a counterclockwise rotation of $\boldsymbol{\phi}$ for increasing s.

In conclusions, these results open new perspectives for breaking macroscopic inversion symmetry (and hence engineering an effective piezoelectric and/or pyroelectric behavior) via twinning – Ref. [70] explored the potential of defects (kinks, junctions, vortices) in the domain wall topology, while here we demonstrate that a macroscopic P can emerge even in "ideal" ferroelastic structures. These arguments can be readily generalized to other materials systems: For example, the improper mechanism pointed out [3] at $CaTiO_3$ twins can be simply (and quantitatively) rationalized as a rotopolar coupling. More generally, our work open new avenues for materials design via domain wall engineering, an increasingly popular strategy

where new functionalities emerge from spatial inhomogeneities, rather than the uniform crystalline phase itself.

Chapter 7

Conclusions

This work is a contribution to the development of a consistent microscopic description of the flexoelectric effect. This has been accomplished on one hand with the more fundamental work presented in Chapter 4, which focuses on the calculation of the bulk flexoelectric tensor within a first-principles electronic-structure framework. On the other hand, in Chapter 5 and 6 we have presented two different applications of the theory of flexoelectricity to real physical systems. In particular, we have studied flexoelectrically enhanced photovoltaic devices, where the electric fields generated by strain gradients facilitate the migration of the carriers to the electrodes, and functional domain walls in ferroelastic $SrTiO_3$, which acquire a polarity in spite of the bulk material structure being centrosymmetric.

The main conclusion of this work can be summarise in the following points:

- Through the formulation and implementation of the novel metric perturbation, defined as an acoustic phonon described in the frame that is co-moving with the atoms, we have achieved an efficient methodology to calculate the bulk FxE tensor for a generic crystal. Via an extensive numerical validation, we have demonstrated, that this procedure has clear advantages in terms of efficiency and ease of use with respect to earlier approaches. Interestingly, the metric-wave perturbation recovers the treatment of the uniform strain of Hamann et al. [33] as special case. In this regard, we have established the formal link between the already available "phonon" and "uniform strain" perturbations, which were previously considered to be conceptually distinct within the context of DFPT.

- Thanks to the recently established connection between the theory of ADPs and the flexoelectric theory, we were able to take advantage of the computed bulk FxE tensor of Si in order to study the electronic band response of a nanomembrane. In practice we have stressed their possible application to engineering an efficient nano-flexovoltage device, i.e. a solar cell device in which the photoexcited carrier pair is separated by the FxE effect. On one hand, our study of unsupported bent membranes unambiguously determines the (100)-oriented system to be the most effective at separating the photoexcited carriers. On the other hand, the application of metallic electrodes has the consequence of suppressing the bulk flexoelectric response, but remarkably an effective electric field is still acting on the photoexited carriers.

- Using our effective model we have identified three main mechanisms that quantify the polar response at the ferroelestic DWs in $SrTiO_3$: (i) the flexoelectric coupling, (ii) the rotopolar term, which is an inhomogeneous coupling

between the polarization and the antiferrodistortive tilts, and (iii) a tri-linear coupling involving the antiferroelectric mode of the Ti atoms, which again is activated by the inhomogeneous behaviour of the antiferrodistortive parameter close to the ferroelastic DWs. All these three terms must be carefully taken into account since their contribution to the total energy of the system are of the same order, resulting in mutual suppressions or enhancement.

The work presented in this thesis has opened many opportunity for the future research. The most recent calculations of the FxE tensor [65], aimed to finalizing a public implementation of flexoelectricity, is heavily based on the metric perturbation. Regarding the flexoevoltaic idea, this is a first example of how the theory of flexoelectricity can be used to understand the interplay between photocurrent and mechanical deformations. In light of the recent promising experimental results [92] on the flexophotovoltaic effect, we regard our study as a starting point for further boosting this field of research. Finally, the study on the ferroelastic domain walls in $SrTiO_3$ clearly open new prospectives for novel device concepts based on domain walls properties, which are currently of great interest in the scientific community. For example one can further explore the connection between cycloid of the antiferroditortive parameter in $SrTiO_3$ and the theory of cycloid in multiferroics, where the polarization is induced by gradients of the magnetic parameter.

Appendix A

Ionic response to a strain gradient deformation

In order to calculate the internal atomic relaxation induced by a monochromatic acoustic phonon in the long wave approximation, one can start from the equation of motion

$$m_\kappa \ddot{u}_{\kappa\alpha}(t) = \Phi^l_{\kappa\alpha,\kappa'\beta} u^l_{\kappa'\beta}(t), \tag{A.1}$$

where $u^l_{\kappa\alpha}(t)$ is the atomic displacement of the sublattice κ in the cell l, and $\Phi_{l\kappa\alpha,m\kappa'\beta}$ is the force constant matrix. Using the expression 3.12, one get

$$m_\kappa \left(\omega^{\mathbf{q}}\right)^2 U^{\mathbf{q}}_{\kappa\alpha} = \Phi^{\mathbf{q}}_{\kappa\alpha,\kappa'\beta} U^{\mathbf{q}}_{\kappa\alpha} \tag{A.2}$$

where

$$\Phi^{\mathbf{q}}_{\kappa\alpha,\kappa'\beta} = \sum_l \Phi^l_{\kappa\alpha,\kappa'\beta} e^{i\mathbf{q}\cdot(\mathbf{R}^l+\boldsymbol{\tau}_\kappa-\boldsymbol{\tau}_{\kappa'})}. \tag{A.3}$$

We now proceed to solve the previous Eq. A.2 for small wavevectors, i.e. $\mathbf{q} \to 0$. To this aim we express $\mathbf{q}$ as function of a small adimensional parameter ϵ ($\mathbf{q} \to \epsilon\mathbf{q}$), which gives the following expressions

$$\begin{aligned}
\omega^{\mathbf{q}} &= \epsilon\omega^{(1,\mathbf{q})} + \frac{\epsilon^2}{2}\omega^{(2,\mathbf{q})} + ... \\
U^{\mathbf{q}}_{\kappa\alpha} &= U^{(0,\mathbf{q})}_{\kappa\alpha} - i\epsilon U^{(1,\mathbf{q})}_{\kappa\alpha} - \frac{\epsilon^2}{2} U^{(2,\mathbf{q})}_{\kappa\alpha} + ... \\
\Phi^{\mathbf{q}}_{\kappa\alpha,\kappa'\beta} &= \Phi^{(0)}_{\kappa\alpha,\kappa'\beta} - i\epsilon\Phi^{(1,\mathbf{q})}_{\kappa\alpha,\kappa'\beta} - \frac{\epsilon^2}{2}\Phi^{(2,\mathbf{q})}_{\kappa\alpha,\kappa'\beta} + ...,
\end{aligned} \tag{A.4}$$

where we have used the convention of Eq. 3.15. Note that the zero order term of $\omega^{\mathbf{q}}$ is zero since here we are considering an acoustic phonon.

Inserting the previous expressions into Eq. A.2, and isolating the zero order in ϵ, one get

$$\Phi^{(0)}_{\kappa\alpha,\kappa'\beta} U^{(0,\mathbf{q})}_{\kappa'\beta} = 0, \tag{A.5}$$

which is satisfied only if

$$U^{(0,\mathbf{q})}_{\kappa'\beta} = U^{(0)}_{\beta}, \tag{A.6}$$

i.e. the displacement of all the sublattices is the same.

The first order equation is

$$\Phi^{(0)}_{\kappa\alpha,\kappa'\beta} U^{(1,\mathbf{q})}_{\kappa'\beta} + U^{(0)}_{\beta} q_\gamma \sum_{\kappa'} \Phi^{(1,\gamma)}_{\kappa\alpha,\kappa',\beta} = 0 \tag{A.7}$$

and the requirements for a non-singular solution is

$$\sum_{\kappa\kappa'} \Phi^{(1,\gamma)}_{\kappa\alpha,\kappa'\beta} = 0. \tag{A.8}$$

Then the solution of the first order equation is

$$\begin{aligned} U^{(1,\gamma)}_{\kappa'\alpha} &= -\Gamma^{\kappa}_{\alpha\beta\gamma} U^{(0)}_{\beta} q_\gamma \\ \Gamma^{\kappa}_{\alpha\beta\gamma} &= \tilde{\Phi}^{(0)}_{\kappa\alpha,\kappa'\delta} \Lambda^{\kappa'}_{\delta\beta\gamma}, \end{aligned} \tag{A.9}$$

where $\Gamma^{\kappa}_{\alpha\beta\gamma}$ is the internal relaxation tensor induce by a uniform strain deformation, $\varepsilon_{\beta\gamma}$, $\Lambda^{\kappa'}_{\delta\beta\gamma}$ is the piezoelectric force-response tensor, $\Lambda^{\kappa}_{\alpha\beta\gamma} = \sum_{\kappa'} \Phi^{(1,\gamma)}_{\kappa\alpha,\kappa'\beta}$, and $\tilde{\Phi}^{(0)}_{\kappa\alpha,\kappa'\delta}$ is the pseudoinverse of the force constant matrix [89].

Finally the second order equation is:

$$-\frac{1}{2}\Phi^{(0)}_{\kappa\alpha,\kappa''\lambda} U^{(2,\mathbf{q})}_{\kappa''\lambda} = m_\kappa \left[\omega^{(1,\mathbf{q})}\right]^2 U^{(0)}_{\alpha} - q_\gamma q_\delta T^{\kappa}_{\alpha\beta,\gamma\delta} U^{(0)}_{\beta}, \tag{A.10}$$

where

$$T^{\kappa}_{\alpha\beta,\gamma\delta} = -\frac{1}{2}\sum_{\kappa'} \Phi^{(2,\gamma\delta)}_{\kappa\alpha,\kappa'\beta} + \frac{1}{2}\left[\Phi^{(1,\gamma)}_{\kappa\alpha,\kappa'\rho}\Gamma^{\kappa'}_{\rho\beta\lambda} + \Phi^{(1,\lambda)}_{\kappa\alpha,\kappa'\rho}\Gamma^{\kappa'}_{\rho\beta\gamma}\right]. \tag{A.11}$$

Following Born and Huang [8], one can define

$$\begin{aligned} [\alpha\beta,\gamma\delta] &= -\frac{1}{2\Omega}\sum_{\kappa\kappa'} \Phi^{(2,\gamma\delta)}_{\kappa\alpha,\kappa'\beta} \\ (\alpha\delta,\beta\gamma) &= \frac{1}{\Omega}\sum_{\kappa} \Phi^{(1,\delta)}_{\kappa\alpha\kappa'\rho}\Gamma^{\kappa'}_{\rho\beta\gamma}. \end{aligned} \tag{A.12}$$

The requirement for a non-singular solution for Eq. A.10 gives

$$\left(M\left(\omega^{(1,\mathbf{q})}\right)^2\delta_{\alpha\beta}-q_\gamma q_\delta T_{\alpha\beta,\gamma\delta}\right)U_\beta^{(0)}=0, \tag{A.13}$$

where $M=\sum_{\kappa'}m_\kappa$ and $T_{\alpha\beta,\gamma\delta}=\sum_{\kappa'}T^\kappa_{\alpha\beta,\gamma\delta}$. Eq. A.13 can be recognized as the sound-wave equation [77]. Combining Eq.s A.10 and A.13, one get

$$\begin{aligned}U_{\kappa\alpha}^{(2,\mathbf{q})}&=2U_\beta^{(0)}q_\gamma q_\delta N^\kappa_{\alpha\beta\gamma\delta}\\ N^\kappa_{\alpha\beta\gamma\delta}&=\tilde{\Phi}^{(0)}_{\kappa\alpha\kappa'\rho}\hat{T}^{\kappa'}_{\rho\beta,\gamma\delta}\\ \hat{T}^\kappa_{\alpha\beta,\gamma\delta}&=T^\kappa_{\alpha\beta,\gamma\delta}-\frac{m_\kappa}{M}T_{\alpha\beta,\gamma\delta}\end{aligned} \tag{A.14}$$

where $N^\kappa_{\alpha\beta\gamma\delta}$ is the type-I flexoelectric internal-strain tensor.

Combining the results A.6, A.9 and A.14, it gives Eq. 3.13.

Finally, note that the elastic tensor is closely related with the tensor $T_{\alpha\beta,\gamma\delta}$; in practice one can shows that [8, 77]

$$C_{\alpha\beta,\gamma\delta}=-\frac{1}{\Omega}\left(T_{\alpha\delta,\beta\gamma}+T_{\alpha\gamma,\delta\beta}-T_{\alpha\beta,\gamma\delta}\right), \tag{A.15}$$

or equivalently

$$C_{\alpha\beta,\gamma\delta}=-[\alpha\beta,\gamma\delta]+[\alpha\gamma,\delta\beta]+[\alpha\delta,\beta\gamma]-(\alpha\beta,\gamma\delta). \tag{A.16}$$

Appendix B

Detailed analysis of surfaces in curvilinear coordinates

Beyond the surface contribution originating from the gradient rotations of the sample that exactly cancels the dynamical bulk term (Sec. 3.2.2), there is the surface piezoelectric response that have an non zero macroscopic effect on the FxE response of a finite object, as already discussed heuristically in section 3.1.4.

Here, using the curvilinear coordinates, we conduct a more detailed analysis of the surface response to a strain gradient deformation. As mentioned before, for slabs systems the key quantity to look at is the flexovoltage, defined in Eq. 3.28, i.e. the change in the *open circuit* voltage drop across the slab, ΔV, as function of the applied strain gradient, $\varepsilon_{\beta,\gamma\delta}$. Our attention for the flexoevoltage of a slab has two main justifications: (i) it is directly related to the experimentally measurable quantity ΔV; (ii) the voltage drop induced by the strain gradient deformation uniquely defines the local voltage drop is uniquely defined (up to a uniform constant that is fixed by the electrostatic boundary conditions) by the microscopic electric field $E(\mathbf{r})$, $E(\mathbf{r}) = -\nabla\Delta V(\mathbf{r})$, which in turn can be calculated from the the microscopic charge density response, using the Gauss equation.

In curvilinear coordinate the Gauss equation becomes [74]:

$$\nabla \cdot \Delta\tilde{\boldsymbol{E}} = -\nabla \cdot \boldsymbol{E}^{met} + \frac{\Delta\tilde{\rho}}{\epsilon_0}, \tag{B.1}$$

where $\boldsymbol{E}_{met}$ is a geometric term originating from the change of coordinates (more specifically from the linear term of the metric tensor in the curvilinear frame) and it is only function of the electric field of the unperturbed system, $\boldsymbol{E}(\boldsymbol{r})$:

$$\boldsymbol{E}^{met}_{\alpha}(\boldsymbol{r}) = \varepsilon_{\beta\gamma}(\boldsymbol{r})[\delta_{\beta\gamma}E_{\alpha}(\boldsymbol{r}) - \delta_{\alpha\beta}E_{\gamma}(\boldsymbol{r}) - \delta_{\gamma\alpha}E_{\beta}(\boldsymbol{r})]. \tag{B.2}$$

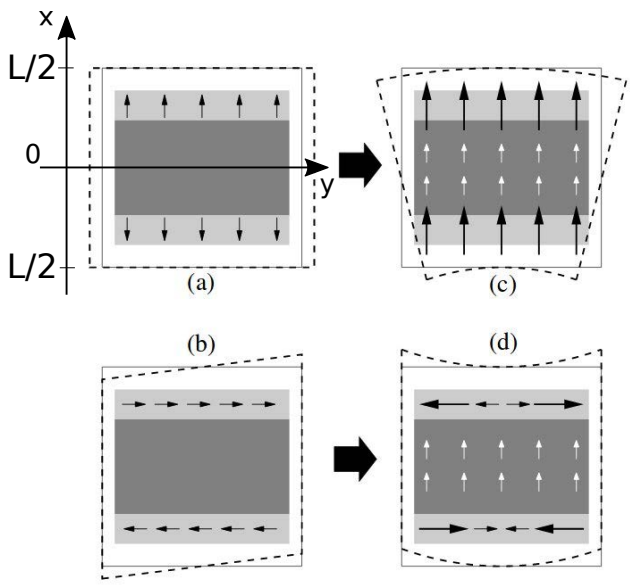

FIGURE B.1: Polarization response in a slab under: (a) uniform transverse strain deformation; (b) uniform transverse strain gradient deformation; (c) uniform shear strain; (d) uniform shear strain gradient deformation. Figure from Ref. [74].

The tilde symbol in Eq. B.1 identifies the curvilinear response functions, and in full generality one can write the generic curvilinear response function , $\tilde{f}(\boldsymbol{\xi})$, as

$$\tilde{f}(\boldsymbol{\xi}) = \varepsilon_{\beta\gamma}(\boldsymbol{\xi}) f^{U}_{\beta\gamma}(\boldsymbol{\xi}) + \varepsilon_{\beta\gamma,\delta}(\boldsymbol{\xi}) f^{G}_{\beta\gamma,\delta}(\boldsymbol{\xi}), \tag{B.3}$$

where $f^{U}_{\beta\gamma}(\boldsymbol{\xi})$ and $f^{G}_{\beta\gamma,\delta}(\boldsymbol{\xi})$ are the response to a uniform strain and uniform strain gradient, respectively. The advantage of working in the curvilinear frame is that in Eq. B.3 any response to a uniform translation of the crystal is already excluded. Note also the similarity of expression B.2 with Eq. 3.18; yet the latter is a macroscopic relation, while the former is a microsocpic relation.

In order to carry out an analysis on the surface and bulk contributions to the microscopic electric field and ultimately to the flexovotlage, it is essential to move back to the polarization response. The Poisson equation in curvilinear coordinates has the same form then in the Cartesian frame, with $\tilde{\mathbf{P}}$ enjoying an expression as Eq. B.3.

For shake of clarity here we consider a non piezoelectric slab centered in the origin and oriented along the $\hat{x}$ axis. Then $P^{U}_{\alpha,\beta\gamma}(\boldsymbol{\xi})$ is non zero only close to the surfaces (due to the surface piezoelectric response), while the strain gradient response function inside the slab is related to the flexoelectric tensor as follows

$$P^{G}_{\alpha\delta,\beta\gamma}(\boldsymbol{\xi} \sim 0) = \frac{\mu_{\alpha\delta,\beta\gamma}}{\epsilon_r}, \tag{B.4}$$

where ϵ_r is the electronic dielectric constant that appears since $P^{G}_{\alpha\delta,\beta\gamma}$ is defined in OC while μ is defined in SC.

Combining the Gauss and Poisson equations, the following relation between the *longitudinal* component of $\mathbf{P}$ and the electric field holds:

$$\frac{1}{\epsilon_0}\nabla \cdot \mathbf{P} = -\nabla \cdot \mathbf{E} - \nabla \cdot \mathbf{E}^{met}. \tag{B.5}$$

In order to proceed further, one has to specialize the previous Eq. B.5 for a defined deformation. Here we consider slabs of cubic crystals, which have three independent types of strain gradient deformations: the longitudinal, transverse and shear (Fig. B.1). The difference is that the first two deformations have a strain gradient that linearly grows in the same direction of the slab, preserving the in-plane periodicity, while in the shear case the strain gradient breaks the in the in-plane periodicity. Than two different dissertation must be done.

To avoid the unecessary complications, the following analysis focus only on the clamped ion electronic response of a slab. The atomic internal relaxation induced

by a strain gradient perturbation can be easily reincorporated following Ref. [74].

longitudinal and transverse case With reference to the Fig. B.1, the local strain along the slab is $\varepsilon_{\alpha\alpha}(x) = \varepsilon_{x,\alpha\alpha}x$, and the polarization has only the $\hat{x}$ component, which is

$$P_x(x) = \left(P^U_{x,\alpha\alpha}(x)x + P^G_{xx,\alpha\alpha}(x)\right)\varepsilon_{x,\alpha\alpha} \tag{B.6}$$

[setting $\alpha = x$ or $\alpha = y$ one recover the longitudinal or transverse case, respectively]. Then Eq. B.5 involves only the longitudinal components (the problem is one dimensional), and therefore the divergence can be remove, getting

$$\begin{aligned} E^U_{x,\alpha\alpha}(x) &= -\frac{1}{\epsilon_0}P^U_{x.\alpha\alpha}(x) - E_x(x)(1-2\delta_{\alpha x}) \\ E^G_{xx,\alpha\alpha}(x) &= -\frac{1}{\epsilon_0}P^G_{xx,\alpha\alpha}(x) \end{aligned} \tag{B.7}$$

Since $P^U_{x,\alpha\alpha}(x)$ and $E_x(x)$ are non zero only on the surface of the slab and they are antisymmetric respect to the origin, also $E^U_{x,\alpha\alpha}(x)$ is antisymmetric and localized only on the surface.

The potential drop across the slab is $\Delta V = -\int_{-\infty}^{+\infty} dx\, E_x(x)$, and reminding the definition of the flexovoltage, Eq. 3.28, toghether with relation B.4, one can write [76]

$$\varphi_{xx,\alpha\alpha} = -\int_0^{+\infty} dx\, E^U_{x,\alpha\alpha}(x) + \frac{\mu_{xx,\alpha\alpha}}{\epsilon_0\epsilon_r} \tag{B.8}$$

where the two right hand side terms can be identified as

$$\begin{aligned} \varphi^{surf}_{xx,\alpha\alpha} &= -\int_0^{+\infty} dx\, E^U_{x,\alpha\alpha}(x) \\ \varphi^{bulk}_{xx,\alpha\alpha} &= \frac{\mu_{xx,\alpha\alpha}}{\epsilon_0\epsilon_r}. \end{aligned} \tag{B.9}$$

Then in the longitudinal and transverse case the total flexovoltage of a slab can be decomposed in a surface and bulk contribution. The former is related to the piezoelectric surface response, while the latter is connected to the bulk flexoelectric response. Note that the electric field inside the slab, is uniquely determined by the bulk crystal FxE response.

shear case In the shear case the strain gradient is perpendicular to the slab, and following Fig. B.1 the local strain is $\varepsilon_{xy}(y) = \varepsilon_{y,xy}y$. Then the polarization response

is

$$\mathbf{P}(\mathbf{r}) = \varepsilon_{y,xy} \begin{pmatrix} P^{G}_{xy,xy}(x) \\ P^{U}_{y,xy}(x) y \\ 0 \end{pmatrix} \tag{B.10}$$

and $\mathbf{E}^{U}_{xy}(\mathbf{r})$ vanishes. Substituting these informations into Eq. B.5, one get

$$\partial_x E^{G}_{xy,xy}(x) = -\frac{1}{\epsilon_0} P^{U}_{y,xy}(x) - \frac{1}{\epsilon_0} \partial_x P^{G}_{xy,xy}(x) + E_x(x) \tag{B.11}$$

where now $P^{U}_{y,xy}(x)$ is symmetric respect to the origin (see Fig. B.1).

We can now calculate the voltage-drop, and the total flexovoltage response of the slab; the result is

$$\varphi_{xy,xy} = \frac{1}{\epsilon_0 \epsilon_r} \left[\mu_{xy,xy} - \int_0^{+\infty} dx\, P^{U}(x) - \epsilon_0 \phi_0 \right], \tag{B.12}$$

where $\phi_0 = \int_0^{+\infty} dx\, E_x(x)$ is the potential offset before the perturbation. Again, it is possible to identify a bulk term and a surface term as

$$\begin{aligned} \varphi^{surf}_{xy,xy} &= -\frac{1}{\epsilon_0 \epsilon_r} \left[\int_0^{+\infty} dx\, P^{U}(x) + \epsilon_0 \phi_0 \right] \\ \varphi^{bulk}_{xy,xy} &= \frac{\mu_{xy,cy}}{\epsilon_0 \epsilon_r}. \end{aligned} \tag{B.13}$$

However the important difference between the present deformation and the longitudinal or transverse case is that the bulk electric field $E^{G}_{xy,xy}(x \sim 0)$ is not only function of the bulk FxE response. Indeed Eq. B.11 is showing that the bulk electric field is function also of the surface contributions. In other words, the surface contributions in Eq. B.11 represent a surface charge density, $\sigma_{xy,xy} = \epsilon_0 \epsilon_r \varphi^{surf}_{xy,xy}$.

In conclusion, the flexovoltage response of a perturbed slab can be always written as the sum of a surface and a bulk term,

$$\varphi^{tot}_{\alpha\delta,\beta\gamma} = \varphi^{surf}_{\alpha\delta,\beta\gamma} + \varphi^{bulk}_{\alpha\delta,\beta\gamma}, \tag{B.14}$$

showing that the global flexoelectric response of a finite object has a surface dependence. Moreover, the electrostatic response in the bulk region, can show a direct dependence from the surfaces, as in the shear case. However, the splitting of Eq. B.14, defined by Eq.s B.9 and B.13, allows to tackle the problem of studying the FxE response of a finite object by studying separately the bulk and surface response.

Finally, note also that the surface and bulk contributions due to the local gradient rotations of the sample, discussed in the Sec. 3.2.2, are already automatically removed, since one can identified the $P(\xi)$ response function, in the curvilinear frame, only with the static contribution of Eq. 3.50.

Cubic crystals: Full bulk flexoelectric tensor by surface response

In Sec. 3.2.1 we have discussed that only the longitudinal flexoelectric response is accessible via the charge density response function. In particular, for cubic crystals the two independent longitudinal components of Eq. 3.41 can be calculated.

As first noted in Ref. [74], for the specific case of cubic crystals there is a strategy to calculate the third missing independent component of the electronic FxE tensor using the charge density response function as fundamental quantity. This is based on the results obtained for the slab geometry and in particular about the surface contribution to a slab response.

In particular, in the case of a slab with a transverse strain gradient distortion, no charge is accumulated at the surface and therefore the surface piezoelectric response is local; in other words the bulk electric field in open circuit EBC is only induced by the local strain gradient deformation (provided that the slab is thick enough), and therefore it is directly related to the bulk flexoelectric response. The solution of the Poisson equation in curvilinear coordinates, as shown in Ref. [78] and summarized in the previous section, can lead to value of $\varphi^{bulk}_{xx,yy}$ and $\mu^{bulk}_{xx,yy}$. This extra information together with the knowledge of $\mu_{[110]}$, Eq. 3.41, is sufficient to obtain all the three independent FxE tensor components.

Appendix C

Metric Hamiltonian

Here we carry out explicitly the derivation of the first-order pseudopotential terms in curvilinear coordinates, Eq.s 4.9 and 4.10,

Local potential

Following the results of Ref. [79], a generic (non-local) pseudopotential operator in the curvilinear coordinates is

$$\tilde{V}^{\mathrm{psp},(0)}(\boldsymbol{\xi},\boldsymbol{\xi}') = \sqrt{h(\boldsymbol{\xi})}\, V^{\mathrm{psp},(0)}(\mathbf{r}(\boldsymbol{\xi}),\mathbf{r}(\boldsymbol{\xi}'))\, \sqrt{h(\boldsymbol{\xi}')}, \tag{C.1}$$

where $h(\boldsymbol{\xi})$ is the determinant of the deformation gradient tensor, $h_{\alpha\beta} = \frac{\partial x_\alpha}{\partial \xi_\beta}$, that in the linear approximation is

$$h(\boldsymbol{\xi}) = 1 + i\mathbf{q}\cdot\boldsymbol{\lambda} e^{i\boldsymbol{\xi}\cdot\mathbf{q}} \tag{C.2}$$

By using the transformation properties of the Dirac delta, one can easily verify that the factors of $\sqrt{h}$ cancel out in the local part,

$$\tilde{V}^{\mathrm{loc},(0)}(\boldsymbol{\xi}) = V^{\mathrm{loc},(0)}(\mathbf{r}(\boldsymbol{\xi})). \tag{C.3}$$

Using Eqs. 2.34 and 4.1, this immediately leads to

$$\begin{aligned}
\tilde{V}^{\mathrm{loc},(0)}(\boldsymbol{\xi}) &= \sum_{l\kappa} v_\kappa^{\mathrm{loc}}[\boldsymbol{\xi} - \mathbf{R}_{l\kappa} + \boldsymbol{\lambda}\,(e^{i\boldsymbol{\xi}\cdot\mathbf{q}} - e^{i\mathbf{R}_{l\kappa}\cdot\mathbf{q}})] \\
&= V^{\mathrm{loc},(0)}(\boldsymbol{\xi}) + e^{i\boldsymbol{\xi}\cdot\mathbf{q}} \sum_{l\kappa}[1 - e^{i(\mathbf{R}_{l\kappa}-\boldsymbol{\xi})\cdot\mathbf{q}}] \times \\
&\quad \boldsymbol{\lambda}\cdot\boldsymbol{\nabla} v_\kappa^{\mathrm{loc}}(\boldsymbol{\xi} - \mathbf{R}_{l\kappa}).
\end{aligned} \tag{C.4}$$

and therefore, for the cell-periodic part of the first-order contribution,

$$V_{\mathbf{q}}^{\mathrm{loc},(\beta)}(\boldsymbol{\xi}) = \sum_{l\kappa}[1 - e^{i(\mathbf{R}_{l\kappa}-\boldsymbol{\xi})\cdot\mathbf{q}}]\,\frac{\partial}{\partial\xi_\beta} v_\kappa^{loc}(\boldsymbol{\xi} - \mathbf{R}_{l\kappa}). \tag{C.5}$$

Note the fact that the first-order potential vanishes identically at $\mathbf{q} = 0$, which is a consequence of adopting the curvilinear reference system.

To evaluate the Fourier transform it is useful to bring the derivative sign out of the lattice sum in $V_{\mathbf{q}}^{\mathrm{loc},(\beta)}(\boldsymbol{\xi})$, obtaining the following three pieces,

$$\begin{aligned} V_{\mathbf{q}}^{\mathrm{loc},(\beta)}(\boldsymbol{\xi}) \;=\; & \frac{\partial}{\partial\xi_\beta}\sum_{l\kappa} v_\kappa^{\mathrm{loc}}(\boldsymbol{\xi} - \mathbf{R}_{l\kappa}) \\ & -\frac{\partial}{\partial\xi_\beta}\left\{\sum_{l\kappa} e^{i\mathbf{q}\cdot(\mathbf{R}_{l\kappa}-\boldsymbol{\xi})} v_\kappa^{\mathrm{loc}}(\boldsymbol{\xi} - \mathbf{R}_{l\kappa})\right\} \\ & -iq_\beta\sum_{l\kappa} e^{i\mathbf{q}\cdot(\mathbf{R}_{l\kappa}-\boldsymbol{\xi})} v_\kappa^{\mathrm{loc}}(\boldsymbol{\xi} - \mathbf{R}_{l\kappa}) \end{aligned} \tag{C.6}$$

By performing the Fourier transform of the local atomic potential, we can readily obtain Eq. 4.9.

Separable potential

To evaluate the separable part, we restart from Eq. C.1 and we recall the following relations:

$$\sqrt{h} \;=\; 1 + \frac{i}{2}\boldsymbol{\lambda}\cdot\mathbf{q}\, e^{i\boldsymbol{\xi}\cdot\mathbf{q}}, \tag{C.7}$$

$$\begin{aligned} \zeta_{\mu\kappa}(\mathbf{r}(\boldsymbol{\xi}) - \mathbf{r}(\mathbf{R}_{l\kappa})) \;=\; & \zeta_{\mu\kappa}(\boldsymbol{\xi} - \mathbf{R}_{l\kappa}) + \\ & e^{i\boldsymbol{\xi}\cdot\mathbf{q}}\,[1 - e^{i(\mathbf{R}_{l\kappa}-\boldsymbol{\xi})\cdot\mathbf{q}}]\,\times \\ & \boldsymbol{\lambda}\cdot\boldsymbol{\nabla}\zeta_{\mu\kappa}(\boldsymbol{\xi} - \mathbf{R}_{l\kappa}). \end{aligned} \tag{C.8}$$

It is also useful to remind some basic properties of the Fourier transformation of separable operators. Assume that we wish to express, in Fourier space, the following cell-periodic function

$$F(\mathbf{r}, \mathbf{r}') = \sum_l f(\mathbf{r} - \mathbf{R}_{l\kappa}) g^*(\mathbf{r}' - \mathbf{R}_{l\kappa}). \tag{C.9}$$

We have, following Eq. (A19) of Ref. [28],

$$F(\mathbf{G}+\mathbf{k},\mathbf{G}'+\mathbf{k}) \;=\; \frac{1}{\Omega}e^{i(\mathbf{G}'-\mathbf{G})\cdot\boldsymbol{\tau}_\kappa} f(\mathbf{G}+\mathbf{k}) g^*(\mathbf{G}'+\mathbf{k}). \tag{C.10}$$

Another basic relationship that we need is

$$\int d^3r\, f^*(\mathbf{r}) e^{i\mathbf{K}'\cdot\mathbf{r}} = \Big(\int d^3r\, f(\mathbf{r}) e^{i\mathbf{K}'\cdot\mathbf{r}}\Big)^* = f^*(\mathbf{K}'). \tag{C.11}$$

Combining all the previous results, after some algebra, we get

$$V^{\mathrm{sep},(\beta)}_{\mathbf{k},\mathbf{q}}(\mathbf{G},\mathbf{G}') = \frac{1}{\Omega}\sum_{\kappa\mu} e_{\mu\kappa} e^{i(\mathbf{G}'-\mathbf{G})\cdot\boldsymbol{\tau}_\kappa} f^{(\beta,\mathbf{q})}_{\kappa\mu}(\mathbf{K},\mathbf{K}'), \tag{C.12}$$

with (the first two terms come from the volume factors, third and fourth from the linear variation of ζ, fifth and sixth from ζ^*)

$$\begin{aligned} f^{(\beta,\mathbf{q})}_{\kappa\mu}(\mathbf{K},\mathbf{K}') \;=\; & \frac{i}{2} q_\beta\, \zeta(\mathbf{K})\, \zeta^*(\mathbf{K}') \\ & + \frac{i}{2} q_\beta\, \zeta(\mathbf{K}+\mathbf{q})\, \zeta^*(\mathbf{K}'+\mathbf{q}) \\ & + iK_\beta\, \zeta(\mathbf{K})\, \zeta^*(\mathbf{K}') \\ & - i(K_\beta+q_\beta)\, \zeta(\mathbf{K}+\mathbf{q})\, \zeta^*(\mathbf{K}') \\ & - i(K'_\beta+q_\beta)\, \zeta(\mathbf{K}+\mathbf{q})\, \zeta^*(\mathbf{K}'+\mathbf{q}) \\ & + iK'_\beta\, \zeta(\mathbf{K}+\mathbf{q})\, \zeta^*(\mathbf{K}') \end{aligned} \tag{C.13}$$

This expression can be further simplified as follows,

$$\begin{aligned} f^{(\beta,\mathbf{q})}_{\kappa\mu}(\mathbf{K},\mathbf{K}') \;=\; & i(K_\beta+\frac{q_\beta}{2})\, \zeta(\mathbf{K})\, \zeta^*(\mathbf{K}') \\ & - i(K'_\beta+\frac{q_\beta}{2})\, \zeta(\mathbf{K}+\mathbf{q})\, \zeta^*(\mathbf{K}'+\mathbf{q}) \\ & - i(K_\beta-K'_\beta+q_\beta)\, \zeta(\mathbf{K}+\mathbf{q})\, \zeta^*(\mathbf{K}'). \end{aligned} \tag{C.14}$$

The final result is precisely Eq. 4.10.

Bibliography

[1] S. V. Aert et al. “Direct Observation of Ferrielectricity at Ferroelastic Domain Boundaries in $CaTiO_3$ by Electron Microscopy”. In: *Adv. Materials* 54 (2012), p. 523.

[2] I. Balsiev. “Influence of Uniaxial Stress on the Indirect Absorption Edge in Silicon and Germanium”. In: *Phys. Rev.* 143 (1966), p. 636.

[3] P. Barone, D. D. Sante, and S. Picozzi. “Improper origin of polar displacements at $CaTiO_3$ and $CaMnO_3$ twin walls”. In: *Phys. Rev. B* 89 (2014), p. 144104.

[4] S. Baroni and R. Resta. “Ab initio calculation of the macroscopic dielectric constant in silicon”. In: *Phys. Rev. B* 33 (1986), pp. 7017–7021.

[5] S. Baroni et al. “Phonons and related crystal properties from density-functional perturbation theory”. In: *Rev. Mod. Phys.* 73 (2001), pp. 515–562.

[6] U. K. Bhaskar et al. “A flexoelectric microelectromechanical system on silicon”. In: *Nature Nanotechnology* 11 (2016), p. 263.

[7] U. K. Bhaskar et al. “Flexoelectric MEMS: towards an electromechanical strain diode”. In: *Nanoscale* 8 (3 2016), pp. 1293–1298.

[8] M. Born and K. Huang. *Dynamical Theory of Crystal Lattices*. Oxford University Press, 1954.

[9] E. V. Bursian and N. Trunov. “Nonlocal piezoelectric effect”. In: *Sov. Phys. Solid State* 16 (1974), p. 760.

[10] E. V. Bursian and O. I. Zaikovskii. In: *Sov. Phys. Solid State* 10 (1968), p. 1121.

[11] W. Cao and G. R. Barsch. “Landau-Ginzburg model of interphase boundaries in improper ferroelastic Perovskites of D184h summetry”. In: *Phys. Rev. B* 41 (1990), p. 4334.

[12] M. Cardona and F. H. Pollak. “Energy-Band Structure of Germanium and Silicon: The k.y Method”. In: *Phys. Rev.* 142 (1966), p. 530.

[13] G. Catalan et al. “Domain wall nanoelectronics”. In: *Rev. Mod. Phys.* 84 (2012), p. 119.

[14] G. Catalan et al. “Flexoelectric rotation of polarization in ferroelectric thin films”. In: *Nature Materials* 10 (2011), p. 963.

[15] K. Chu et al. “Enhancement of the anisotropic photocurrent in ferroelectric oxides by strain gradients”. In: *Nature Nanotechnology* 10 (2015), p. 972.

[16] E. Courtens. “Birefringence of $SrTiO_3$ Produced by the 105° K Structural Phase Transition”. In: *Phys. Rev. Lett.* 29 (1972), pp. 1380–1383.

[17] L. E. Cross. “Flexoelectric effects: Charge separation in insulating solids subjected to elastic strain gradients”. In: *Journal of Materials Science* (2006), pp. 53–63.

[18] M. S. Dresselhaus, G. Dresselhaus, and A. Jorio. *Group Theory: Application to the Physics of Condensed Matter*. Springer-Verlag Berlin Heidelberg, 2008.

[19] C. E. Dreyer, M. Stengel, and D. Vanderbilt. “Current-density implementation for calculating flexoelectric coefficients”. In: *Phys. Rev. B* 98 (2018), p. 075153.

[20] E. A. Eliseev et al. “Universal emergence of spatially modulated structures induced by flexoantiferrodistortive coupling in multiferroics”. In: *Phys. Rev. B* 88 (2013), p. 224105.

[21] Y. Frenkel et al. “Imaging and tuning polarity at SrTiO3 domain walls”. In: *Nature Materials* 16 (2017), p. 1203.

[22] M. Fuchs and M. Scheffler. “Ab initio pseudopotentials for electronic structure calculations of poly-atomic systems using density-functional theory”. In: *Comput. Phys. Commun.* 119 (1999), p. 67.

[23] P. Giannozzi et al. “Ab initio calculation of phonon dispersions in semiconductors”. In: *Phys. Rev. B* 43 (1991), pp. 7231–7242.

[24] L. Goncalves-Ferreira et al. “Ferrielectric twin walls in $CaTiO_3$”. In: *Phys. Rev. Lett.* 101 (2008), p. 097602.

[25] X. Gonze and J.-P. Vigneron. “Density-functional approach to nonlinear-response coefficients of solids”. In: *Phys. Rev. B* 39 (1989), pp. 13120–13128.

[26] X. Gonze et al. “ABINIT: First-principles approach to material and nanosystem properties”. In: *Computer Physics Communications* 180 (2009). 40 YEARS OF CPC: A celebratory issue focused on quality software for high performance, grid and novel computing architectures, pp. 2582 –2615.

[27] X. Gonze. “Adiabatic density-functional perturbation theory”. In: *Phys. Rev. A* 52 (1995), pp. 1096–1114.

[28] X. Gonze. "First-principles responses of solids to atomic displacements and homogeneous electric fields: Implementation of a conjugate-gradient algorithm". In: *Phys. Rev. B* 55 (1997), pp. 10337–10354.

[29] X. Gonze and C. Lee. "Dynamical matrices, Born effective charges, dielectric permittivity tensors, and interatomic force constants from density-functional perturbation theory". In: *Phys. Rev. B* 55 (1997), pp. 10355–10368.

[30] J. Greil et al. "Nanowires enabling strained photovoltaic". In: *Appl. Phys. Lett.* 104 (2014), p. 163901.

[31] C. Guo and M. A. Van Hove. "Ab Initio Atomistic Prediction of Charge Separation in Bent Silicon Nanostructures". In: *J. Phys. Chem. C* 115 (2011), p. 4516.

[32] J. H. Haeni et al. "Room-temperature ferroelectricity in strained $SrTiO_3$". In: *Nature* 430 (2004), p. 759.

[33] D. R. Hamann et al. "Metric tensor formulation of strain in density-functional perturbation theory". In: *Phys. Rev. B* 71 (2005), p. 035117.

[34] P. Hohenberg and W. Kohn. "Inhomogeneous Electron Gas". In: *Phys. Rev.* 136 (1964), B864–B871.

[35] J. Hong et al. "The flexoelectricity of barium and strontium titanates from first principles". In: *J.Phys.: Condens. Matter* 22 (2010), p. 112201.

[36] J. Hong and D. Vanderbilt. "First-principles theory and calculation of flexoelectricity". In: *Phys. Rev. B* 88 (2013), p. 174107.

[37] J. Hong and D. Vanderbilt. "First-principles theory of frozen-ion flexoelectricity". In: *Phys. Rev. B* 84 (2011), p. 180101.

[38] V. Indenbom, E. Loginov, and M. Osipov. "Elastic Constants of Crystals from Linear-Response Theory". In: *Kristallografiya* 26 (1981), p. 1157.

[39] Y. Kanai, Z. Wu, and J. C. Grossman. "Charge separation in nanoscale photovoltaic materials: Recent insights from first-principles electronic structure theory". In: *J. Mater. Chem.* 20 (2010), p. 1053.

[40] R. D. King-Smith and D. Vanderbilt. "First-principles investigation of ferroelectricity in perovskite compounds". In: *Phys. Rev. B* 49 (1994), pp. 5828–5844.

[41] A. V. Kityk et al. "Low-frequency superelasticity and nonlinear elastic behavior of $SrTiO_3$ crystals". In: *Phys. Rev. B* 61 (2000), p. 946.

[42] L. Kleinman and D. M. Bylander. "Efficacious Form for Model Pseudopotentials". In: *Phys. Rev. Lett.* 48 (1982), pp. 1425–1428.

[43] L. Kleinman and D. M. Bylander. "Efficacious Form for Model Pseudopotentials". In: *Phys. Rev. Lett.* 48 (1982), pp. 1425–1428.

[44] S. M. Kogan. In: *Sov. Phys. Solid State* 5 (1964), p. 2069.

[45] W. Kohn and L. J. Sham. "Self-Consistent Equations Including Exchange and Correlation Effects". In: *Phys. Rev.* 140 (1965), A1133–A1138.

[46] H. Lu et al. "Mechanical Writing of Ferroelectric Polarization". In: *Science* 336 (2012), pp. 59–61.

[47] W. Ma and L. E. Cross. "Flexoelectric effect in ceramic lead zirconate titanate". In: *Applied Physics Letters* 86 (2005), p. 072905.

[48] W. Ma and L. E. Cross. "Flexoelectric polarization of barium strontium titanate in the paraelectric state". In: *Applied Physics Letters* 81 (2002), pp. 3440–3442.

[49] W. Ma and L. E. Cross. "Observation of the flexoelectric effect in relaxor Pb(Mg1/3Nb2/3)O3 ceramics". In: *Applied Physics Letters* 78 (2001), pp. 2920–2921.

[50] R. Maranganti and P. Sharma. "Atomistic determination of flexoelectric properties of crystalline dielectrics". In: *Phys. Rev. B* 80 (2009), p. 054109.

[51] R. M. Martin. "Piezoelectricity". In: *Phys. Rev. B* 5 (1972), pp. 1607–1613.

[52] R. R. Martin. *Electronic Structure: Baisc Theory and Practical Methods*. Cambridge: Cambridge University Press, 2008.

[53] V. S. Mashkevich and K. B. Tolpygo. In: *Sov. Phys. JETP* 5 (1957), p. 435.

[54] H. J. Monkhorst and J. D. Pack. "Special points for Brillouin-zone integrations". In: *Phys. Rev. B* 13 (1976), pp. 5188–5192.

[55] A. N. Morozovska et al. "Roto-flexoelectric coupling impact on the phase diagrams and pyroelectricity of thin $SrTiO_3$ films". In: *J. Appl. Phys.* 112 (2012), p. 064111.

[56] M. Mostovoy. "Ferroelectricity in Spiral Magnets". In: *Phys. Rev. Lett.* 96 (2006), p. 067601.

[57] M. C. Payne et al. "Iterative minimization techniques for ab initio total-energy calculations: molecular dynamics and conjugate gradients". In: *Rev. Mod. Phys.* 64 (1992), pp. 1045–1097.

[58] J. P. Perdew and Y. Wang. "Accurate and simple analytic representation of the electron-gas correlation energy". In: *Phys. Rev. B* 45 (1992), pp. 13244–13249.

[59] R. M. Pick, M. H. Cohen, and R. M. Martin. "Microscopic Theory of Force Constants in the Adiabatic Approximation". In: *Phys. Rev. B* 1 (1970), pp. 910–920.

[60] K. M. Rabe and J. D. Joannopoulos. "Ab initio determination of a structural phase transition temperature". In: *Phys. Rev. Lett.* 59 (1987), pp. 570–573.

[61] R. Resta. "Deformation-potential theorem in metals and in dielectrics". In: *Phys. Rev. B* 44 (1991), pp. 11035–11041.

[62] R. Resta, L. Colombo, and S. Baroni. "Absolute deformation potentials in semiconductors". In: *Phys. Rev. B* 41 (1990), p. 12358.

[63] R. Resta. "The origin of antiferroelectricity in $PbZrO_3$". In: *J. Phys.: Condens. Matter* 22 (2010), p. 123201.

[64] R. Resta. "Towards a Bulk Theory of Flexoelectricity". In: *Phys. Rev. Lett.* 105 (2010), p. 127601.

[65] M. Royo and M. Stengel. "First-principles theory of spatial dispersion: Dynamicalquadrupoles andflexoelectricity". In: *arXiv:1812.05935* ().

[66] N. Sai and D. Vanderbilt. "First-principle study of ferroelectric and antiferrodistortive instabilities in tetragonal $SrTiO_3$". In: *Phys. Rev. B* 62 (2000), p. 13942.

[67] J. Sakuri and J. Napolitano. *Modern Quantum Mechanics*. Addison-Wesley, 1994.

[68] E. K. H. Salje. "Ferroelastic materials". In: *Annu. Rev. Mater. Res.* 42 (2012), p. 265.

[69] E. K. H. Salje et al. "Domains within Domains and Walls within Walls: Evidence for Polar Domains in Cryogenic $SrTiO_3$". In: *Phys. Rev. Lett.* 111 (2013), p. 247603.

[70] E. K. H. Salje et al. "Flexoelectricity and the polarity of complex ferroelastic twin patterns". In: *Phys. Rev. B* 94 (2016), p. 024114.

[71] E. K. Salje. "Ferroelastic Materials". In: *Annual Review of Materials Research* 42 (2012), pp. 265–283.

[72] W. Setyawan and S. Curtarolo. "High-throughput electronic band structure calculations: Challenges and tools". In: *Computational Materials Science* 49 (2010), pp. 299 –312.

[73] M. Stengel. "From flexoelectricity to absolute deformation potentials: The case of SrTiO3". In: *Phys. Rev. B* 92 (2015), p. 205115.

[74] M. Stengel. "Microscopic response to inhomogeneous deformations in curvili near coordinates". In: *Nat. Com.* 4 (2013), p. 2693.

[75] M. Stengel. "Unified ab initio formulation of flexoelectricity and strain-gradient elasticity". In: *Phys. Rev. B* 93 (2016), p. 245107.

[76] M. Stengel and D. Vanderbilt. "First-principles theory of flexoelectricity". In: *arXiv:1507.03440* (2015).

[77] M. Stengel. "Flexoelectricity from density-functional perturbation theory". In: *Phys. Rev. B* 88 (2013), p. 174106.

[78] M. Stengel. "Surface control of flexoelectricity". In: *Phys. Rev. B* 90 (2014), p. 201112.

[79] M. Stengel and D. Vanderbilt. "Quantum theory of mechanical deformations". In: *Phys. Rev. B* 98 (2018), p. 125133.

[80] A. K. Tagantsev. "Piezoelectricity and flexoelectricity in crystalline dielectrics". In: *Phys. Rev. B* 34 (1986), pp. 5883–5889.

[81] A. K. Tagantsev et al. "The origin of antiferroelectricity in $PbZrO_3$". In: *Nature Communications* 4 (2013), p. 2229.

[82] A. K. Tagantsev. "Landau Expansion for Ferroelectrics: WhichVariable to Use?" In: *Ferroelectrics* 375 (2008), p. 19.

[83] N. Troullier and J. L. Martins. "Efficient pseudopotentials for plane-wave calculations". In: *Phys. Rev. B* 43 (1991), pp. 1993–2006.

[84] H. Uwe and T. Sakudo. "Stress-induced ferroelectricity and soft phonon modes in $SrTiO_3$". In: *Phys. Rev. B* 13 (1976), p. 271.

[85] D Vanderbilt. "Berry-phase theory of proper piezoelectric response". In: *Journal of Physics and Chemistry of Solids* 61 (2000), pp. 147 –151.

[86] C. G. Van de Walle and R. M. Martin. ""Absolute" deformation potentials: Formulation and ab initio calculations for semiconductors". In: *Phys. Rev. Lett.* 62 (1989), pp. 2028–2031.

[87] C. G. V. de Walle and R. M. Martin. "Theoretical calculations of heterojunction discontinuities in the Si/Ge system". In: *Phys. Rev. B* 34 (1986), p. 5621.

[88] H. E. Weaver. "Dielectric properties of single crystals of $SrTiO_3$ at low temperatures". In: *J. Phys. Chem. Solids* 11 (1959), p. 274.

[89] X. Wu, D. Vanderbilt, and D. R. Hamann. "Systematic treatment of displacements, strains, and electric fields in density-functional perturbation theory". In: *Phys. Rev. B* 72 (2005), p. 035105.

[90] Z. Wu, J. Neaton, and J. Grossman. "Charge Separation via Strain in Silicon Nanowires". In: *Nano Lett.* 9 (2009), p. 2418.

[91] Z. Wu, J. B. Neaton, and J. C. Grossman. "Charge Separation via Strain in Silicon Nanowires". In: *Nano Lett.* 9 (2009), p. 2418.

[92] M.-M. Yang, D. J. Kim, and M. Alexe. "Flexo-photovoltaic effect". In: *Science* 360 (2018), pp. 904–907.

[93] W. Zhong, D. Vanderbilt, and K. M. Rabe. "First-principles theory of ferroelectric phase transitions for perovskites: The case of $BaTiO_3$". In: *Phys. Rev. B* 52 (1995), pp. 6301–6312.

[94] W. Zhu et al. "Piezoelectric composite based on the enhanced flexoelectric effects". In: *Applied Physics Letters* 89 (2006), p. 192904.

[95] P. Zubko et al. "Strain-Gradient-Induced Polarization in $SrTiO_3$ Single Crystals". In: *Phys. Rev. Lett.* 99 (2007), p. 167601.

[96] P. Zubko, G. Catalan, and A. K. Tagantsev. "Flexoelectric Effect in Solids". In: *Annual Review of Materials Research* 43 (2013), pp. 387–421.

List of Publications

The Ph.D. candidate is co-author of the following works:

- A. Schiaffino and M. Stengel, *Phys. Rev. Lett.* **119** (2017) 137601 (used for this thesis, Chapter 6)
- B. Casals, A. Schiaffino, A. Casiraghi, S. J. Hämäläinen, D. López González, S. van Dijken, M. Stengel and G. Herranz, *Phys. Rev. Lett.* **120** (2018) 217601 (not used for this thesis)
- A. Schiaffino, C. E. Dreyer, D. Vanderbilt and M. Stengel, *Phys. Rev. B* **99** (2019) 085107 (used for this thesis, Chapter 4)